NANOCRYSTALLINE MIXED METAL OXIDES IN GAS SENSORS AND PIGMENTS

Thesis submitted to
Indian Institute of Technology, Kharagpur
for the award of the degree

of

Doctor of Philosophy

by

Soumya Kanti Biswas

under the supervision of

Professor Panchanan Pramanik

and

Dr. Amita (Pathak) Mahanty

DEPARTMENT OF CHEMISTRY
INDIAN INSTITUTE OF TECHNOLOGY, KHARAGPUR
JULY 2008

Chapter 4

Synthesis of Nanocrystalline Powders of $CuGa_2O_4$ and Studies on their Gas Sensing Behavior towards Ammonia, Hydrogen and Liquefied Petroleum Gas

Dedicated to My Parents

DECLARATION

I certify that

a. *The work contained in this thesis is original and has been done by me under the guidance of my supervisors.*

b. *The work has not been submitted to any other Institute for any degree or diploma.*

c. *I have followed the guidelines provided by the Institute in preparing the thesis.*

d. *I have conformed to the norms and guidelines given in the Ethical Code of Conduct of the Institute.*

e. *Whenever I have used materials (data, theoretical analysis, figures, and text) from other sources, I have given due credit to them by citing them in the text of the thesis and giving their details in the references. Further, I have taken permission from the copyright owners of the sources, whenever necessary.*

..……..

Soumya Kanti Biswas

CERTIFICATE

This is to certify that the thesis entitled **Nanocrystalline Mixed Metal Oxides in Gas Sensors and Pigments**, submitted by **Soumya Kanti Biswas** to Indian Institute of Technology, Kharagpur, is a record of bona fide research work under our supervision and is worthy of consideration for the award of the degree of Doctor of Philosophy of the Institute.

Professor Panchanan Pramanik

Dr. Amita (Pathak) Mahanty

Date: 26.07.08

Acknowledgements

It has been a long trudge to accomplish my dissertation for doctorate degree, but the experience was pleasant one during this period. My research work will remain incomplete if I do not offer my gratitude to those people, who helped me during this venture. It is a pleasure to convey my gratitude to them all in my humble acknowledgment.

I was fortunate to have Prof. P. Pramanik and Dr. Amita (Pathak) Mahanty as supervisors in my doctoral research. It is difficult to overstate my appreciation to my supervisor, Prof. P. Pramanik, who first brought me into the world of research and introduced me to a new concept of science and technology, "Nano" which is the most promising area of modern research. His personal care and constant encouragement have helped me to grow my interest in the research. I am very much grateful to him for the confidence he placed in me and his worthwhile guidance throughout this course of research work which resulted in the present endeavor.

I would like to acknowledge my research co-supervisor, Dr. Amita (Pathak) Mahanty for her unstinted invaluable guidance and advice at the different stages of my research work. I am truly grateful to her especially for the contribution in organizing this thesis.

I would also like to thank Dr. T. Gnansekaran and his group (Liquid Metals and Structural Chemistry Division, Indira Gandhi Centre for Atomic Research, Kalpakkam, Tamil Nadu, India), for giving me an opportunity to visit Kalpakkam, for carrying out experiments on gas response measurements in their laboratory at the early stage of my research on the gas sensors. They have a significant contribution for the gas sensors portion being realized in this thesis.

I am also very much indebted to Prof. A. Basak, Department of Chemistry; Prof. S. S. Bandyapadhyaya, Cryogenic Centre; and Prof. C. K. Das, Material Science, Indian Institute of technology Kharagpur for being agreed to be members of the doctoral scrutiny committee in the midst of all their activity.

I wish to thank Prof. P. Chattaraj, present head of the Department of Chemistry.

*I am thankful to Mahan*da, *technical staff in the Cryogenic Centre who helped me lot in fabrication of the sample holder and the test chamber for the sensing measurements.*

Recognition is due to the numerous technical and non-technical staff of the Institute along with the legion of friends and colleagues, who have lent their expertise and cooperation at various stages of this endeavor.

This acknowledgment would be incomplete without mentioning the names of all my labmates. We have become close friends during this long period. I am feeling happy to acknowledge my seniors, Dr. Asit Baran Panda and Mr. Abhijit Tarafdar who made this place and my research work easier to me by their friendly behavior, valuable advices from the very beginning when I joined here as a novice. I would also like to thank all my friends, Mr. Tanmay Kumar Ghorai, Mr. Debasis Dhak, Mrs. Sasmita Mohapatra, Mrs. Sudeshna Ray, Dr. Shrabanee Sen, Mr. Susanta Biswas, and Mr. Nabakumar Pramanik who have made my stay in Kharagpur an enjoyable experience. My special thanks also go to all my juniors, Ms. Mansamita Das, Mr. Prasanta Dhak, Mr. Sumanta Kumar Sahu, Ms. Soma Das, Ms. Samarpita Senapati, and Ms. Dipshikha Bhattacharya.

I am obliged to the Department of Science and Technology, India and the Department of Atomic Energy, India for granting my fellowship and the financial support during the course of this investigation.

I would like to acknowledge the appropriate authorities for providing instrumental facilities and the support of this research work accomplishing in the premises of Indian Institute of Technology Kharagpur, India.

Lastly, and most importantly, I would like to say that I am greatly fortunate to have an extremely supportive family who has always been a source of comfort and hope when I needed it. It is impossible to convey my feeling in words to my parents Sri Subrata Kumar Biswas and Srimati Astamita Biswas, my lovable younger sister (Sayantani) and my wife, Mrs. Arpita (Sarkar) Biswas for their constant support and cooperation in all aspects. The blessing, affection and care of my parents have been the constant source of my inspiration throughout the entire period of my academic career. I am extremely grateful to Arpita for all her constant help and inspiration in my research life. Her association, constant support kept me confident, mentally fresh even in awkward situation during this research period.

Dated: 26.07.2008 Soumya Kanti Biswas

Abstract

The thesis attempts to establish a versatile and technically simple aqueous-based chemical synthesis methodology for the preparation of nanocrystalline powders of $CuNb_2O_6$, $CuGa_2O_4$, $FeNbO_4$, and Pt impregnated $FeNbO_4$ for gas sensing application and nanocrystalline powders of $Ni_{0.1}W_{0.1}Ti_{0.8}O_2$, $NiBaTi_7O_{16}$, and $Cr_{2x}W_xTi_{1-3x}O_2$ (x = 0.05, 0.1, 0.15) for pigment application. Nanocrystalline powders of the oxides are produced on calcination of carbonaceous precursors, generated through complete evaporation of the precursor solutions of triethanolamine (TEA) and water-soluble chelated complexes of the desired metal ions.

Gas sensing studies of the compressed pellets of the nanocrystalline powders of $CuNb_2O_6$, $CuGa_2O_4$, $FeNbO_4$, and Pt impregnated $FeNbO_4$ reveal their sensitivity towards 500 ppm of reducing gases such as, H_2, liquefied petroleum gas (LPG) and NH_3. $CuNb_2O_6$ system shows the maximum response of 84% towards H_2 at 300 ºC; around 80% towards LPG at 300 ºC; and 56% towards NH_3 at 400 ºC, while the $CuGa_2O_4$ system reveals the maximum response of 82%, 75% and 37% towards H_2, LPG, and NH_3 respectively at the operating temperature of 350 ºC. Similar studies of the $FeNbO_4$ system exhibit the maximum response of 93% towards H_2 at 250 ºC, and 92% and 52% towards LPG & NH_3 gases respectively at 300 ºC. Incorporation of platinum into $FeNbO_4$ (i.e., Pt- $FeNbO_4$ system) is found to improve the system's gas sensing properties through reduction in the sensor operating temperature, sensor response time and recovery time with maximum sensitivity of 94% towards H_2 at 175 ºC, 95% towards LPG at 200 ºC, and 61% towards NH_3 at 250 ºC.

Ni^{2+}or Cr^{3+} doped nanocrystalline titanate powders [such as: $Ni_{0.1}W_{0.1}Ti_{0.8}O_2$, $NiBaTi_7O_{16}$, and $Cr_{2x}W_xTi_{1-3x}O_2$ (x = 0.05, 0.1, 0.15)] give rise to interesting color shades in different color range due to *d-d* transition of the *d*-electrons of Ni^{2+}or Cr^{3+} ions, and show promising properties for pigments application. The measurement of the color parameters (*CIE L* a* b**) reflect an intense yellow color with greenish shades for the $BaNiTi_7O_{16}$ composition, while the $Ni_{0.1}W_{0.1}Ti_{0.8}O_2$ solid solution exhibit yellow coloration with reddish shades. Doping Cr^{3+} ion in the rutile lattice on

the other hand, impart buff colouration to the $Cr_{2x}W_xTi_{1-3x}O_2$ (x = 0.05, 0.1, 0.15)] solid solution.

The developed chemical method uses simple metalo-organic based complex chemistry to prepare the aqueous-based precursor solution that contained appropriate amounts of TEA and the desired metal ions in the suitably chelated form. TEA used in the process, not only helps in homogeneous dispersion of the desired metal ions in the precursor solution through formation of stable, water-soluble coordinated complexes with the metal ions but also circumvents sintering of the final powders by generating a porous carbonaceous matrix for the metal ions on dehydration of the precursor solution. Moreover, the carbonaceous precursors (generated from TEA) when calcined generate heat through combustion thereby, facilitates realization of the desired oxide phase at external temperatures much lower than those reported through other routes so far. Low processing temperatures results in nanocrystalline powders of desired oxides with average grain sizes below 60 nm and high specific surface areas up to 110-120 m^2g^{-1} in few cases.

CONTENTS

Page

Title Page …… i

Dedication ……..... ii

Declaration …….. iii

Certificate by the Supervisors …… iv

Acknowledgement ……. v

Abstract …….. vii

Chapter 1 Introduction

1.1 Nanotechnology and Nanocrystalline Materials …… 1

1.2 Nanocrystalline Metal Oxides and their Importance ……. 4

1.3 Synthesis of Metal Oxide Nanoparticles …… 6

1.3.1 Coprecipitation Method …….. 8

1.3.2 Solvothermal/Hydrothermal Method ……. 8

1.3.3 Microemulsion Process …….. 9

1.3.4 Sol-Gel Method …….. 10

1.3.5 The Pechini Method ……... 11

1.3.6 Self-Combustion Method ……... 12

1.3.7 Metal Ion-Ligand Complex Based Precursor Solution Method ……... 13

1.4 Gas Sensors …… 16

1.4.1 Different Parameters Determining the Sensor Characters. 17

1.4.2 Nanocrystalline Metal Oxide Gas Sensors ….…… 18

1.5 Pigments ……. 25

1.5.1 Inorganic Pigments ……. 26

1.5.2 Metal Oxide Based Pigments ……. 27

1.5.2.1 Mixed Metal Oxide Based Pigments ……... 28

1.5.3 Nanocrystalline Mixed Metal Oxide Pigments ... 29

1.6 Objectives and Scope of the Present Work …… 31

References …….. 33

Chapter 2 Synthesis of Nanocrystalline Powders of $CuNb_2O_6$ and Studies on their Gas Sensing Behavior towards Ammonia, Hydrogen and Liquefied Petroleum Gas.

2.1 Introduction …… 41

2.2 Reported Methods for the Preparation of $CuNb_2O_6$ ……... 42

2.2.1 Conventional Solid-State Method …….. 42

2.2.2 Chemical Method ……... 43

2.3 Scope of the Present Investigation ……. 43

2.4 Synthesis of Nanocrystalline $CuNb_2O_6$ Powders ……... 44

2.4.1 The Raw Materials Used in the Developed Synthesis Method …….. 44

2.4.1.1 Preparation of Aqueous Solution of Niobium Tartrate …….. 44

2.4.2 Synthesis Procedure of Nanocrystalline $CuNb_2O_6$ Powders ……. 46

2.5 Techniques for Characterization of the Prepared Nanocrystalline $CuNb_2O_6$ Powder ……. 47

2.6 Results and Discussion …….. 48

2.6.1 Thermal Studies of the Nanocrystalline $CuNb_2O_6$ Precursors ……. 48

2.6.2 Composition, Phase and Structural Analysis of the Nanocrystalline $CuNb_2O_6$ Powders ……... 49

2.6.3 Morphology and Microstructural Studies of the Nanocrystalline $CuNb_2O_6$ Powders …….. 51

2.6.4 Electrical Measurements and Gas Sensing Studies of the Nanocrystalline $CuNb_2O_6$ …….. 54

2.6.4.1 Electrical Measurements of the Nanocrystalline $CuNb_2O_6$ and Discussion …… 57

2.6.4.2 Gas Sensing Studies of the Nanocrystalline $CuNb_2O_6$ and Discussion …… 58

2.7 Major Findings in the present Investigation …….. 63

References …….. 65

Chapter 3 Synthesis of Nanocrystalline Powders of $FeNbO_4$ (with and without Pt Impregnation) and Studies on their Gas Sensing Behavior towards Ammonia, Hydrogen, and Liquefied Petroleum Gas.

3.1 Introduction …… 67

3.2 Reported Methods for the Preparation of $FeNbO_4$ ……..... 68

3.2.1 Conventional Solid-State Method …….. 68

3.2.2 Chemical Method ……... 69

3.3 Scope of the Present Investigation ……. 70

3.4 Synthesis of Nanocrystalline $FeNbO_4$ Powders ……..... 71

3.4.1 The Raw Materials Used in the Developed Synthesis Method …….. 71

3.4.1.1 Preparation of Aqueous Solution of Niobium Tartrate ……... 72

3.4.2 Synthesis Procedure of Nanocrystalline $FeNbO_4$ Powders 72

3.4.3 Procedure for the Synthesis of Platinum (1 wt %) Incorporated Nanocrystalline $FeNbO_4$ (Pt-$FeNbO_4$) Powders …….. 73

3.5 Techniques for Characterization of the Prepared Nanocrystalline $FeNbO_4$ Powders ……..... 73

3.6 Results and Discussion ……... 74

3.6.1 Thermal Studies of the Nanocrystalline $FeNbO_4$ Precursors ……... 74

3.6.2 Composition, Phase and Structural Analysis of the Nanocrystalline $FeNbO_4$ Powders ……. 75

3.6.3 Morphology and Microstructural Studies of the Nanocrystalline $FeNbO_4$ Powders …… 77

3.6.4 Electrical Measurements and Gas Sensing Studies of the Nanocrystalline $FeNbO_4$ ……. 80

3.6.4.1 Electrical Measurements of the Nanocrystalline $FeNbO_4$ and Discussion …….. 80

3.6.4.2 Gas Sensing Studies of the Nanocrystalline $FeNbO_4$ and Discussion ……. 81

3.7 Major Findings in the present Investigation ……... 84

References …….. 86

Chapter 4 Synthesis of Nanocrystalline Powders of $CuGa_2O_4$ and Studies on their Gas Sensing Behavior towards Ammonia, Hydrogen and Liquefied Petroleum Gas.

4.1 Introduction …… 89

4.2 Reported Methods for the Preparation of $CuGa_2O_4$ ……... 90

4.2.1 Conventional Solid-State Method …….. 91

4.2.2 Chemical Method ……... 91

4.3 Scope of the Present Investigation ……. 91

4.4 Synthesis of Nanocrystalline $CuGa_2O_4$Powders ……..... 92

4.4.1 The Raw Materials Used in the Developed Synthesis Method ……... 92

4.4.1.1 Preparation of Aqueous Solution of Gallium Nitrate ……. 92

4.4.2 Synthesis Procedure of Nanocrystalline $CuGa_2O_4$ Powders …….. 92

4.5 Techniques for Characterization of the Prepared Nanocrystalline $CuGa_2O_4$ Powder …… 93

4.6 Results and Discussion ……... 94

4.6.1 Composition, Phase and Structural Analysis of the Nanocrystalline $CuGa_2O_4$ Powders …… 94

4.6.2 Morphology and Microstructural Studies of the Nanocrystalline $CuGa_2O_4$ Powders …… 96

4.6.3 Electrical Measurements and Gas Sensing Studies of the Nanocrystalline $CuGa_2O_4$ ……... 98

4.6.3.1 Electrical Measurements of the Nanocrystalline $CuGa_2O_4$ and Discussion …… 99

4.6.3.2 Gas Sensing Studies of the Nanocrystalline $CuGa_2O_4$ and Discussion …… 100

4.7 Major Findings in the present Investigation ……... 103

References …….. 104

Chapter 5 Synthesis of Nanocrystalline Powders of $Ni_{0.1}W_{0.1}Ti_{0.8}O_2$ and $BaNiTi_7O_{16}$ for Pigment Applications

5.1 Introduction …… 107

5.2 Reported Methods for the Preparation of $Ni_{0.1}W_{0.1}Ti_{0.8}O_2$ and $BaNiTi_7O_{16}$ ……. 109

5.2.1 Conventional Solid-State Method …….. 109

5.2.2 Chemical Method ……... 110

5.3 Scope of the Present Investigation ……. 110

5.4 Synthesis of Nanocrystalline Powders of $Ni_{0.1}W_{0.1}Ti_{0.8}O_2$ and $BaNiTi_7O_{16}$ ……..... 111

5.4.1 The Raw Materials Used in the Powders of $Ni_{0.1}W_{0.1}Ti_{0.8}O_2$ and $BaNiTi_7O_{16}$……... 111

5.4.1.1 The Raw Materials Used in the Preparation of Nanocrystalline Powders of $Ni_{0.1}W_{0.1}Ti_{0.8}O_2$ 111

5.4.1.2 The Raw Materials Used in the Preparation of Nanocrystalline Powders of $BaNiTi_7O_{16}$ 111

5.4.1.3 Preparation of Aqueous Solution Dimethylammonium Tungstate ……... 111

5.4.1.4 Preparation of Aqueous Solution of Titanium oxalate ……. 112

5.4.2.1 Synthesis Procedure of Nanocrystalline $Ni_{0.1}W_{0.1}Ti_{0.8}O_2$ Powders …… 113

5.4.2.2 Synthesis Procedure of Nanocrystalline $BaNiTi_7O_{16}$ Powders …… 115

5.5 Techniques for Characterization of the Prepared Nanocrystalline $Ni_{0.1}W_{0.1}Ti_{0.8}O_2$ and $BaNiTi_7O_{16}$ Powders ……. 116

5.6 Results and Discussion ……... 117

5.6.1 Thermal Studies of the Nanocrystalline $Ni_{0.1}W_{0.1}Ti_{0.8}O_2$ and $BaNiTi_7O_{16}$ Precursors ……..... 117

5.6.2 Composition, Phase and Structural Analysis of the Nanocrystalline $Ni_{0.1}W_{0.1}Ti_{0.8}O_2$ and $BaNiTi_7O_{16}$ Powders …… 119

5.6.3 Morphology and Microstructural Studies of the Nanocrystalline $Ni_{0.1}W_{0.1}Ti_{0.8}O_2$ and $BaNiTi_7O_{16}$ Powders …… 123

5.6.4 UV-visible Spectroscopy Studies and Color Measurements of the Nanocrystalline $Ni_{0.1}W_{0.1}Ti_{0.8}O_2$ and $BaNiTi_7O_{16}$ Powders ……. 125

5.7 Major Findings in the present Investigation…… 128

Reference……. 129

Chapter 6 Synthesis of Nanocrystalline Powders of $Cr_{2x}W_xTi_{1-3x}O_2$ (x = 0.05, 0.1, 0.15) for Pigment Applications

6.1 Introduction …… 131

6.2 Reported Methods for the Preparation of $Cr_{2x}W_xTi_{1-3x}O_2$ ……. 132

6.2.1 Conventional Solid-State Method …… 132

6.2.2 Chemical Method ……..... 133

6.3 Scope of the Present Investigation ……. 133

6.4 Synthesis of Nanocrystalline Powders of $Cr_{2x}W_xTi_{1-3x}O_2$ (x = 0.05, 0.1, 0.15) …..... 135

6.4.1 The Raw Materials Used in the Developed Synthesis Method…….. 135

6.4.1.1 Preparation of Aqueous Solution Dimethylammonium Tungstate…… 135

6.4.1.2 Preparation of Aqueous Solution of Titanium oxalate ……. 135

6.4.2 Synthesis Procedure of Nanocrystalline $Cr_{2x}W_xTi_{1-3x}O_2$ (x = 0.05, 0.1, 0.15) Powders…… 135

6.5 Techniques for Characterization of the Prepared Nanocrystalline Powders of $Cr_{2x}W_xTi_{1-3x}O_2$ (x = 0.05, 0.1, 0.15)…… 137

6.6 Results and Discussion ……... 138

6.6.1 Thermal Studies of the Nanocrystalline $Cr_{2x}W_xTi_{1-3x}O_2$ (x = 0.05, 0.1, 0.15) Precursors……..... 138

6.6.2 Composition, Phase and Structural Analysis of the Nanocrystalline $Cr_{2x}W_xTi_{1-3x}O_2$ (x = 0.05, 0.1, 0.15) Powders …… 140

6.6.3 Morphology and Microstructural Studies of the Nanocrystalline $Cr_{2x}W_xTi_{1-3x}O_2$ (x = 0.05, 0.1, 0.15) Powders …… 144

6.6.4 UV-visible Spectroscopy Studies and Color Measurements of the Nanocrystalline $Cr_{2x}W_xTi_{1-3x}O_2$ (x = 0.05, 0.1, 0.15) Powders ……..... 147

6.7 Major Findings in the present Investigation…… 151

Reference……. 152

Chapter 7 Conclusions and Scope of Future Studies

Appendix A

Appendix B

Appendix C

Annexure

Curriculum Vita

List of Publications

Chapter 1

Introduction

Chapter 1

Introduction

1.1 Nanotechnology and Nanocrystalline Materials

The concept of 'nanotechnology' was envisioned by Nobel Prize-winner physicist, Richard P Feynman, way back in 1959 (Feynman, 1960) but it was only in 1974 that the terminology was actually conceived by Norio Taniguchi (Taniguchi, 1974) and defined as the processes of separation, consolidation, and deformation of materials on a molecular scale. The term was later explored and popularized by K. Eric Drexler through his journal articles (Drexler, 1981) and the book '*Engines of Creation: The Coming Era of Nanotechnology*' (Drexler, 1986). The word 'nanotechnology', derived from the Greek word '*nãnos*' meaning 'dwarf', is befittingly used to underline its fundamental theme of miniaturization. It can be broadly defined as the technology that deals with structures and processes in the spatial dimensions of less than 100 nanometers (1 nanometer = 1×10^{-9} meter). Some of these technologies despite having only limited control of structure at the nanometer scale are already in use, producing useful products. They are also being further developed to produce even more sophisticated products, in which the structure of matter is more precisely controlled.

Nanotechnology received its greatest momentum when scientists acquired new sophisticated tools such as, the scanning tunneling microscope (STM) and the atomic force microscope (AFM) to picture single atoms with unprecedented clarity. STM, invented in 1982 by Binning and Rohrer, allows imaging of solid surfaces of conducting samples with atomic scale resolution. AFM, developed in 1986 by Binning, Quate and Gerber, enables scientists to study non-conducting surfaces as it scans van der Waals forces with its 'atomic' tips.

Since the early 1990s, the term 'nanocrystalline material' and synonymous terminologies such as, nanoscaled material/nanophase material/nanosized material/ nanomaterial, have emerged to encompass the structure of matter, controlled at the nanometer scale, that can be used to produce novel materials and devices with useful

and unique properties. Nanocrystalline material may be broadly identified as those which have dimensions larger than that of a molecular cluster but smaller than that of a bulk material, more importantly they show selected properties/ phenomena that are different from either and can be uniquely assigned to them. Accordingly, it is nanotechnology through which we attempt to harness these phenomena of the nanocrystalline materials for the application at the macroscopic scale such as, for device application. 'Nanomaterial' is now a generic term used to designate materials that have structures within 100 nm (nm = nanometer) in at least one of the spatial dimensions.

Materials with particle sizes (i.e., diameters) in the nanosize regime have experienced a rapid development in last two decades due to their exciting and potential applications in a wide variety of technological areas. With particle sizes diminishing to nanometer scale, the materials exhibit unique and interesting properties compared to their conventional coarse/bulk counterparts. A list of the physical properties which undergo change with diminishing grain sizes in a material is summarized in Table 1.1.

Table 1.1: *Summary of changes observed in some of the physical properties of nanocrystalline materials*

Properties	**Change Observed in Nanocrystalline Materials**
Mechanical	• Increase in hardness and strength of metals and alloys • Enhanced ductility and toughness in metals and alloys
Electrical	• Higher electrical conductivity in ceramics and magnetic nanocomposites • Higher electrical resistivity in metals
Magnetic	• Increase in coercivity down to a critical grain size • Decrease in coercivity leading to super paramagnetic behavior in magnetic material below critical grain size
Catalytic	• Increased catalytic activity due to enhanced surface area, large interface volume and modified coordination number of the

	surface atoms in metal/alloys/ceramics
Optical	• Blue-shift of optical spectra of quantum-confined crystallites • Increase in luminescence efficiency of semiconductors
Temperatures	• Decrease of sintering and melting temperatures and increase of plasticity in pure and composite metals and ceramics

The unique properties of nanocrystalline materials can be attributed to their high surface areas and dominance of quantum effects. The nanomaterials possess high surface-to-volume ratio and are therefore characterized by (i) large fraction of surface atoms and large number of grain boundaries (ii) high surface energy, and (iii) spatial confinement, which do not exist in their corresponding coarse-grained polycrystalline counterparts (Cao, 2004). Thus, in nanomaterials a large fraction of atoms are boundary atoms and as the grain size are reduced from 10 nm, 5 nm to 1 nm the fraction of their atoms at the surfaces or, at the grain boundaries increases from 30 %, 40 % to 98 % respectively (Pathak *et al*., 2001). These surface atoms are characterized by (a) lower coordination number, (b) lower coordination symmetry, and (c) lower atomic density (Gleiter, 1989). Therefore, the interface structure plays an important role in determining the physical and mechanical properties of nanomaterials. Especially when the sizes of nanoparticles are comparable to Debye length, the entire material would be affected by the surface properties of nanosized materials (Lüth, 1995; Ogawa *et. al.*, 1982). As the size of matter is reduced to tens of nanometers or less, quantum effects begin to come into play, and these can significantly change the materials' physico-chemical properties, such as: optical, magnetic or electrical properties etc (Barker *et al.*, 2008). Therefore, high surface areas and thus, large fractions of surface atoms together with small particle sizes provides scope for distinctly new and different properties in the nanocrystalline materials.

1.2 Nanocrystalline Metal Oxides and their Importance

Metals form a large variety of oxide compounds that can exist in a number of structural geometries (Wyckoff, 1964) and depending on their electronic structure they can show insulating, semiconducting, metallic and even superconducting behavior. Metal oxides especially, of transition metals, play a significant role in many areas of chemistry, physics, and materials science (Fernández-García *et al.*, 2004, Rickerbya *et al.*, 2007) due to their wide ranging physico-chemical properties originating from the multiple valency states of the metal ions. In technological applications, metal oxides are used in the fabrication of microelectronic circuits, chemical sensors, piezoelectric devices, in coatings for corrosion protection or thermal isolation, in heterogeneous and environmental catalysis, etc (Al-Abadleh *et. al.*, 2003; Faraday Discussion, 1999; Spoto *et.al.*, 2004; Weiss *et.al.,* 2002). The major proportions of the catalysts used in industrial applications involve metal oxides either as an active phase, or/and a promoter, or/and as "support". The chemical and petrochemical industries predominantly use metal and metal oxide catalysts (Ertl, 1997). For monitoring environmental pollution, metal oxide based catalysts or sorbents are employed to remove the oxides of carbon, nitrogen, and sulfur species generated during the combustion of fossil-derived fuels. Additionally, metal oxides are vastly used in the semiconductor industry. Most of the chips used in computers today contain a metal oxide component.

In the emerging field of nanotechnology, an objective is to formulate nanocrystalline metal oxide materials with unique properties which are much improved with respect to those of bulk materials (Bäumer *et. al.,* 1999; Gleiter, 1995; Rodriguez, *et. al.,* 2002; Trudeau, *et. al.,* 1996; Valden, *et. al.,* 1998). Nanocrystalline oxides can exhibit unique chemical properties either owing to the limited size of their grains and a high density of low-coordinated surface sites or, can provide new extended systems with unprecedented structure, morphology and/or composition. Very unreactive oxides in the form of massive crystals become highly reactive when prepared in high surface area form (Kourtakis, 2002; Richards *et al.*, 2001). Similarly,

unique structures and/or, chemical compositions of nanocrystalline oxides can bring about revolutionary properties in the materials.

Nanocrystalline metal oxides have found technological applications as electronic, magnetic, optical materials, ceramics, catalytic and porous materials etc. A brief account of their varied applications is documented below.

- Nanocrystalline oxides are usually used as heterogeneous catalysts and their catalytic activity is due to their enhanced surface area, large interface volume and modified coordination number of the surface atoms. Heterogeneous catalysis plays an important role in the production of fine chemicals, petroleum refinery, environmental protection and remediation, and processing of consumer products and advanced materials.
- Nanocrystalline oxides have great technological and industrial importance for their photoactivity. There are many applications of pure, functionalized or doped oxide films or oxide nanoparticles (e.g., titania) for the photocatalytic activity in our everyday life, such as, in solar cells, as self-cleaning surface film on glass windows.
- Thin films of nanocrystalline metal oxides with high dielectric constants, also called high-K dielectrics, are important in microelectronic industry as a substitute for silicon dioxide as an insulating component in metal oxide field effect transistors.
- Recent years have witnessed a tremendous growth of research in the field of magnetoelectronics, in view of its obvious potential for novel devices with entirely new capabilities. The oxides of transition metals and their interfaces with metals and semiconductors represent one of the most exciting areas currently studied in magnetism.
- Nanocrystalline semiconducting metal oxides with controlled composition are indeed of increasing interest in gas sensing, and also constitute a new and exciting subject in fundamental research.
- Nanocrystalline metal oxides based pigments are commercially important because of their good chemical and thermal stability, high refractive indices,

insolubility (bleed resistance), high surface coverage, easy dispersibility in dispersing medium for paint formulation.

1.3 Synthesis of Metal Oxide Nanoparticles

There are two basic strategies involved in the synthesis of metal oxide nanoparticles/nanostructure; they are *the bottom-up* and *the top-down* approaches (Hu, *et al.*, 1999). Both approaches are schematically represented in Figure 1.1. All the solution-based chemical methods for syntheses of oxides belong to the bottom-up approach, and it involves building up of nanostructures through staking of the fundamental building-blocks which can be atom-by-atom, or molecule-by-molecule, or cluster-by-cluster. Top-down approach, on the other hand, leads to the formation of nanostructures by breaking down bulk materials gradually into smaller sizes until the grains are obtained in the nanometric dimension. Thermal/mechanical attrition or, milling of the bulk material is typical example of this approach (Koch, 1989). Although the top-down approach of synthesis of oxides offers reliability and is suitable for fabrication of complex device components, they are constrained by higher energy usage, and greater waste generation compared to the bottom-up approach. Moreover, the conventional top-down approach such as, lithography results in imperfection in the surface structure and introduces additional defects during the etching step. Despite these disadvantages, the top-down strategy remains as a significant approach for the synthesis of oxide nanoparticles.

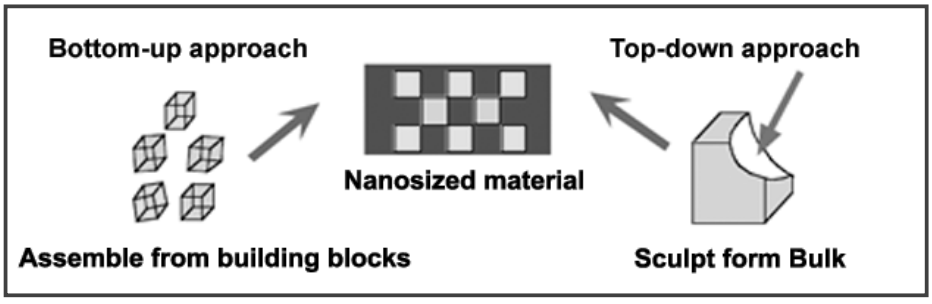

Figure 1.1: *Schematic illustration for Bottom-up and Top-down approach* (*reproduced after* Hu, E. L. *et al.*, 1999).

Bottom-up approach, which is the common strategy involved in the synthesis of nanomaterials, can be classified under three major heads depending on their processing techniques; they are - chemical synthesis, self assembly, and positional assembly.

- Chemical synthesis is a method of producing raw materials such as, molecules or particles, which can then be used either directly in products in their bulk disordered form, or as the building blocks of more advanced ordered materials, produced using the self assembly, and positional assembly techniques.
- Self assembly is a bottom-up synthesis technique in which atoms or molecules arrange themselves spontaneously under equilibrium conditions into ordered and stable nanoscaled structures by physical or chemical interactions between the units.
- The final bottom-up technique is positional assembly, whereby atoms, molecules or clusters are deliberately manipulated and positioned one-by-one.

Bottom-up approach promises a better chance to obtain nanostructures with less defects, high chemical homogeneity and better short and long range ordering. Bottom-up approach is driven mainly by the reduction of Gibbs free energy, so that the nanoparticles produced are in a form closer to a thermodynamic equilibrium state.

Solution-based chemical synthesis techniques are among the most common and crucial bottom-up synthesis strategies available for the synthesis of nanocrystalline powders, especially for the multi-component oxide systems. Few of the most popularly known chemical synthesis routes (Cushing *et al.*, 2004) available for the preparation of nanocrystalline mixed oxides include: coprecipitation, solvothermal/hydrothermal, sol–gel, microemulsion and solvent evaporation methods. A concise review of the common chemical synthesis techniques available for the preparation of nanocrystalline mixed metal oxide powders is summarized below.

1.3.1 Coprecipitation Method

Probably the most widely used method for the preparations of nanocrystalline oxides is the *coprecipitation method*. Since, in this method, two or more species are precipitated simultaneously, the method is termed coprecipitation. This method involves the precipitation of sparingly soluble products from aqueous/nonaqueous solutions. The coprecipitation of metal ions as hydroxides, carbamates, carbonates, bicarbonates, or oxalates, (called precipitates) followed by the separation of the precipitates with a filtration step and subsequent calcination and decomposition, is a common way of producing crystalline nanoparticles of oxides. The coprecipitation reaction involves nucleation, crystal growth, coarsening, and/or agglomeration in the precipitates simultaneously (Cushing *et al.*, 2004). Besides simple addition/exchange reactions, precipitation can be performed by some other methods, such as, chemical reduction, photoreduction, oxidation, and hydrolysis. A chemical precipitation is generally not a controlled process in terms of reaction kinetics and the solid phase nucleation and growth process (Feng *et al.*, 2004). The precipitation reactions for the synthesis of complex oxides containing multiple constituent ions (more than two) gets complicated, as multiple species, having variable reaction kinetics, need to get precipitated simultaneously for obtaining homogeneous precursors.

1.3.2 Solvothermal/Hydrothermal Method

In *solvothermal method*, the solvent is brought to a temperature well above its boiling point by increase in the autogenous pressure through heating in a sealed reaction-vessel (reactor/ autoclave). When water is used as solvent in the reaction, the method is called as *hydrothermal method.* The solvothermal or hydrothermal method is based upon the solubility of almost all inorganic substances in a solvent at elevated temperatures and pressures and subsequent crystallization of the dissolved material from the fluid (Burda *et al.*, 2005). Although synthesis reaction can be carried out at a temperature ranging from 100 ºC to 1000 ºC and under pressure ranging from one atmosphere to several thousand atmosphere, most of the hydrothermal experiments are conducted below the supercritical temperature of water, i.e. 374 ºC (Cushing *et*

al., 2004; Roy, 1987). The solvothermal synthesis yields crystalline metal oxides at temperatures substantially below those required by traditional solid-state reactions. Unlike the cases of coprecipitation and sol-gel methods, the products of solvothermal reactions are usually crystalline and do not require post annealing treatments. As a result, this method can avoid the formation of hard agglomerates unlike in sol-gel or coprecipitation method. Therefore, this is the major advantage in the hydrothermal process in preparation of nanophase oxides. Among the low temperature methods, the hydrothermal method is versatile (Komarneni, 2003). There are few more advantages associated with this method (Stambaugh, 1982), namely, easy to control particle size and morphology by varying synthesis conditions (Feng *et al.*, 2004), significant increase of kinetics of the reaction by a small increase of the reaction temperature, formation of new metastable products, obtaining high purity products from impure feedstocks. Successful synthesis of materials by the hydrothermal synthesis depends on the selection of its precursors. A precursor, which should be both reactive as well as cost effective, should additionally posses appropriate process conditions and variables such as, temperature, pH, ionic strength and cationic and anionic concentrations.

1.3.3 Microemulsion Process

Microemulsion synthesis is very popular reported method, in recent literature for the synthesis of nanocrystalline inorganic oxides, mixed oxides, semiconductors etc (Feng *et al.*, 2004). Microemulsions are thermodynamically stable, fluid, and optically clear dispersions (10-100 nm subphases) of two immiscible liquids such as water and oil. Microemulsions form when a surfactant, or more commonly a mixture of surfactants and cosurfactants, lowers the oil/water interfacial tension to ultralow values, allowing thermal motions to spontaneously disperse the two immiscible phases. In a typical process for nanoparticle synthesis by microemulsion technique, the organo metallic and/or metal salt precursors are dissolved inside the water pools of the reverse spherical micelles, and are allowed to react via droplet collision and rapid intermicellar exchange of their water content (Bourgeat-Lami, 2002). As each

droplet acts as an independent reactor, the morphology of the powder product can be easily controlled by manipulating the droplet size. The main advantage associated with microemulsion synthesis is the synthesis of the metal oxides with the narrow particle size distribution. The process is however disadvantaged by low product yield.

1.3.4 Sol-Gel Method

The sol-gel method is based on inorganic polymerization reactions (Cushing *et al.*, 2004). The name *sol-gel* is given to the process because of the distinctive viscosity increase that occurs at a particular point in the sequence of steps. A sudden increase in viscosity in sol-gel process leads to the gelation (Rao, 1994). The sol-gel process includes four steps: hydrolysis, poly-condensation, drying, and thermal decomposition. Precursors of the metal or nonmetal alkoxides hydrolyze with water or alcohols according to the hydrolysis process (Roy, 1987). The whole process has following steps:

Step I involves the mixing of components together to make a solution. This solution is a true ionic or molecular mixture of a multicomponent composition and ensures the atomic scale mixing of the components, which is the basis for the ultra homogenization in sol-gel technique. The liquid phase in the vast majority of the oxide gel is water or short-chain alcohol, and the solutes may be inorganic nitrates, inorganic chlorides, or a wide variety of metal organic molecules.

Step II is the key step of the sol-gel process. It involves the formation of a sol and conversion of it to a gel so that it retains a chemical homogeneity of the sample during the desiccation. Conversion to a sol is accompanied by adjusting the activity of some species, H^+ and OH^- and other ions, which result in the formation of a dispersed solid phase.

Step III involves the gelation of the sol which is in principle controlled by the pH, ionic strength and temperature of the precursor mixture. A manipulation of these parameters is an empirical procedure and it must be worked out independently for

each composition although the general condition of pH and temperature are known for simple oxides. The fine-tuning of this step for different starting materials, especially new organic precursors and multi component systems has become a major area of current research.

Step IV is drying of gel; in this step water and alcohol are removed at moderate temperatures (below 200 ºC), leaving a hydroxylated metal oxide with residual organic remnant. To prepare a high surface area *aerogel*, the solvent is removed supercrtically.

Step V is the last step of the process involving the desiccation and heat treatment of the gels to obtain nanocrystalline oxide powders.

The versatility and general usefulness of modern sol-gel processing in the synthesis of nanoparticles are associated with the better homogeneity, high purity, lower processing temperature, more uniform phase distribution in multicomponent systems, better size and morphological control compared to the traditional ceramic method.

1.3.5 The Pechini Method

In 1967, Pechini (1967) developed a modified sol-gel process which has become one of the popular chemical synthesis routes for the preparation of a variety of mixed oxide powders at relatively low temperatures. The Pechini method, as it is now referred to, relies on the formation of complexes of metal ions with organic chelating agents such as α-carboxylic acids (e.g. citric acid). A polyalcohol such as, ethylene glycol is added to establish linkages between the chelates by a polyesterification reaction, resulting in gelation of the reaction mixture. The technique contains a step where the gel is rapidly dehydrated at low temperatures and subsequently pyrolysed to result in the of fine oxide powders. The advantage of the Pechini method is the ability to synthesize considerably complex oxides with good chemical homogeneity through an easy approach.

1.3.6 Self-Combustion Method

The self-combustion method has been widely used in the synthesis of a variety of oxides/ceramic particles. This method is also known as the 'self-sustaining propagating high-temperature synthesis' (SHS), the combustion method, and autoignition process, or is sometimes more specifically the organometallic polymer precursor method. Unlike the Pechini or the amorphous citrate-gel processes, these processes are rapid and may approach direct conversion from the molecular mixture of the precursor solution to the final oxide product, avoiding formation of intermediate crystalline phases that require inter diffusion for complete reaction. The process makes use of highly exothermic redox chemical reactions between the reactants to produce a flame due to spontaneous combustion, which then yields the desired product or its precursor in finely divided form. The method involves a molecular mixture of oxidizers (e.g., metal nitrates, ammonium nitrates etc.) and reducers (e.g., carbon containing materials such as urea, carbohydrazide, glycine, polyvinyl alcohol, sucrose, ethylenediamine tetraacetic acid), which can be ignited at relatively low temperatures. This method involves complete evaporation of aqueous precursor solutions that are composed of stoichiometric amounts of the desired metal ions, mixed with polymers or complexing agent resulting fluffy voluminous carbonaceous mass that constitutes the precursor materials.

In the present thesis, the author reports the preparation of various nanocrystalline mixed metal oxide compositions through pyrolysis of *metal ion-ligand complex based precursor solution*. Thermal decomposition of aqueous precursor solution of metal ion-ligand complex is a bottom-up synthesis strategy, which stands out as an alternative and promising approach for the preparation of chemically homogeneous nanocrystalline oxide for a variety of compositions. The approach is technically simple and versatile and hence has been adopted in the present investigation for the preparation of mixed metal oxide gas sensor materials and oxide pigments compositions.

1.3.7 Metal Ion-Ligand Complex Based Precursor Solution Method

The synthesis method involves pyrolysis of aqueous based precursor solution that comprises of water-soluble, metal ion-ligand complexes of the desired metal ions in the requisite molar ratios. The complexing/chelating agents generally used for obtaining the water-soluble, metal ion-ligand complexes are triethanolamine (TEA), oxalic acid, ethylenediaminetetraacetic acid (EDTA) and tartaric acid. The complexing/chelating agents are used to keep the metal ions in homogeneous solution throughout the reaction without undergoing precipitation. To ensure this, the moles of the complexing/chelating agent per unit mole of the metal ion in the starting solution are always kept in excess. The choice of the appropriate organic acid as the complexing agent is based on the solubility of the resulting complex in water. The synthesis method involves the complete dehydration of the metal ion-ligand complex precursor solution followed by decomposition of the metal complexes. The decomposition results in a voluminous, organic based, black, fluffy mass. This organic mass is easily crushed to fine powders to compose the *precursor powders*. The as-prepared precursor powders are calcined at respective crystallization temperatures of the desired oxide compositions. The complexing/chelating agents apart from serving as solubilizer for the uniform distribution of the cations in the solution also act as fuels during calcinations of the precursor powders. A generalized process for the preparation of nanocrystalline mixed metal oxides through the metal ion-ligand complex based precursor solution method is shown in Figure 1.2. A photograph of a voluminous, organic based, black, fluffy mass, generally obtained through the process is depicted in Figure 1.3.

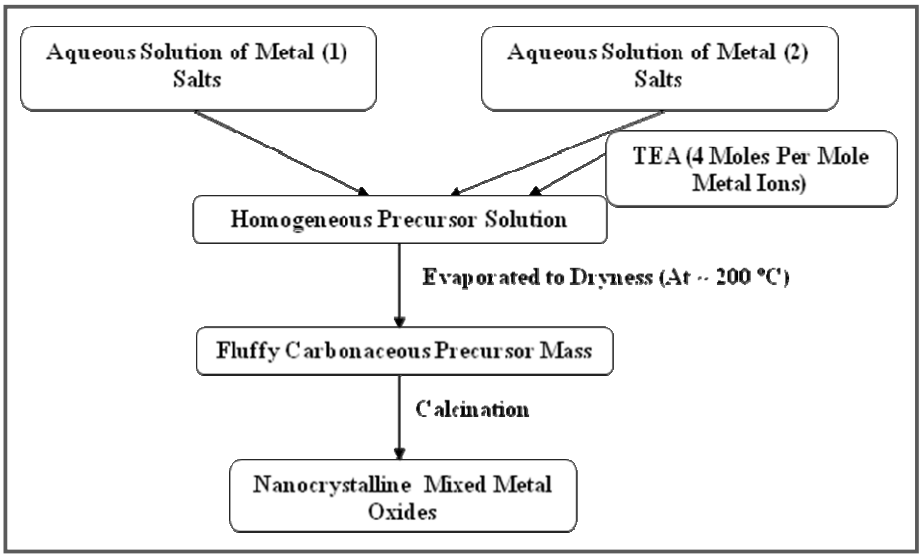

Figure 1.2: *Schematic representation of metal ion-ligand complex based precursor solution method.*

Figure 1.3: *A photograph of black carbonaceous fluffy mass.*

In the metal ion-ligand complex based precursor solution TEA is used as a competent complexing agent for the generation of nanosized particles at reduced external heat treatment temperatures. TEA is a tetradentate chelating ligand that readily complexes with a number of metal ions in the aqueous medium and thereby ensures their homogeneous dispersion in the precursor solution (Figure 1.4). The

chelation of metal ions with TEA in the precursor solution is dependent on the pH of the reaction medium, concentrations of TEA to the metal ions, and temperature. In the precursor solution, the amount of TEA is always maintained in excess to the required stoichiometry and the unchelated, free TEA in the precursor solution probably undergoes polymerization during evaporation process and generates a highly branched polymeric framework for anchoring the metal ions/metal coordinated complexes (Biswas *et al.*, 2008; Pathak *et al.*, 2004). This not only prevents segregation/precipitation of the metal ion from the homogeneous precursor solution during evaporation but also provides a voluminous, fluffy carbonaceous matrix in which metal ions embed on complete evaporation of the precursor solution. Slow heat-treatment of the carbonaceous residue through calcination in dynamic air, results in the nanosize particles of the respective mixed oxide and the heat generated through combustion of the carbonaceous mass facilitates the reduction in the external temperatures required for the formation of desired oxide phase. The entire oxidative decomposition process develops a large amount of gases (such as: water vapor, oxides of carbon and nitrogen), which helps the precursor material to dissipate the heat of combustion and thus inhibits sintering of the fine particles during the process.

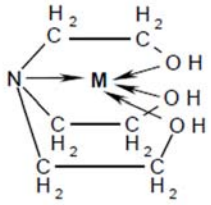

Figure 1.4: *Probable metal-TEA complex.*

The present investigation would be an attempt to establish the suitability and reliability of the proposed chemical synthetic technique through preparation of various metal oxide compositions that find application either in gas sensors or in pigments.

1.4 Gas Sensors

In our everyday life, the frequently used term "sensor" defines a technological device, which responds to an external stimulus and subsequently turns it into a suitable output signal, which can be measured or recorded and interpreted. The output signal from a sensor is typically electronic in nature, being a current, voltage, or impedance/conductance change caused by change in external analyte composition or quality. The external stimulus can be a change of physical condition such as, temperature, pressure, etc. or a chemical substance such as gas etc. Thus, based on the kind of external analytes and the nature of interactions with them, the sensors are categorized into two classes: Physical sensors and Chemical sensors. A physical sensor measures the physical conditions of a system whereas a chemical sensor provides the information of a chemical, ranging from the concentration of a specific sample component to total composition analysis.

Increasing awareness for protecting the environment, public health and the private properties from hazardous and poisonous gases, released mostly by motor vehicles, industries and power plants in the atmosphere has promoted the need for gas sensors. Therefore, in the past decade, research efforts in gas sensors have grown extensively worldwide. The prime interest concerning gas sensors is the capable of detecting major pollutants such as hydrocarbons, oxides of nitrogen, and oxides of carbon in atmosphere. The basic objectives of all such researches and developments are to design cheap, small, robust and user-friendly gas sensor materials which possess high response, selectivity and stability in harsh environments. Based on different sensing principles a variety of gas sensors such as, metal oxide semiconductor gas sensors, optical sensors, thermal conductivity sensors, mass sensitive devices like quartz microbalance sensors, catalytic sensors, dielectric sensors, electrochemical sensors and electrolyte sensors have been developed.

1.4.1 Different Parameters Determining the Sensor Characters

Response

Response, generally, means a qualification of a sensor for measuring a given concentration of an analyte. For a gas sensor, the response is defined as the measure of the variation of output signals (current, resistance or voltage) of it under exposure of test gas. The test gas interacts or adsorbs onto the surface of the gas sensitive materials, thereby bringing about the change of the electrical properties (like conductivity) of the sensor material, which represents a measure of the gas concentration. The response (S) of a sensor material to a given concentration of a gas is generally expressed as:

$$S = \frac{R_g - R_a}{R_a} \times 100\,\%$$

In which, R_a and R_g denote the resistances of the material in air and in gas, respectively. Response depends on the sensor operational temperatures; careful temperature modulation has been noticed to improve discrimination and quantification of sensitivity. Doping of noble metals ions in some cases and use of nanoparticles of the sensor materials also play significant role in improving the response of the sensor materials.

Selectivity

Sensor material may have different responses towards different gases at any operating temperature. Selectivity can be defined as the ratio of response (S_1) of one gas to that (S_2) of another gas at a temperature or over a temperature range for equivalent concentrations of both gases.

$$Selectivity = \frac{S_1}{S_2}$$

Thus from a study of responses, the best operating temperature for the selectivity of a sensor can be determined.

Response Time and Recovery Time

Response time is considered as the time required for the sensor output to reach 90% of its saturation (final change in resistance) after applying or switching off the respective gas in a step function and recovery time is taken as the time needed for the sensor to attain 10% above the original output value (resistance) in air.

1.4.2 Nanocrystalline Metal Oxide Gas Sensors

The idea of using metal oxide semiconductors as gas responsive devices was instigated in 1952, when Brattain *et al.,* (1952) first reported the gas sensitivity of Germanium. Seiyama *et al.* (1962) were the first to observe that metal oxides were gas sensitive and they went ahead to demonstrate that ZnO could be used for the detection of inflammable and toxic gases. Unrelated but concurrent work carried out by Taguchi introduced SnO_2 as the first commercially available metal oxide gas sensor in 1968 (Taguchi, 1970a, 1970b, 1970c, 1972). Since then, gas sensors using simple binary metal oxides, such as SnO_2, TiO_2, WO_3, ZnO, Fe_2O_3, and In_2O_3 have been extensively investigated (Simon *et al.*, 2001). Amongst them, SnO_2 is by far the most popular gas sensitive oxide. These metal oxides are *n*-type semiconductors; they possess an electron depleted surface under normal atmospheric conditions and in the typical operational temperatures range of 200-400 ºC. The electron depleted surface forms due to adsorption of atmospheric oxygen, which gets dissociated into O_2^- or O^- species (Morrison, 1978) by accepting electronic carriers from the semiconductor oxides. This chemisorbed oxide ion (O_2^- or O^-) participates in the reaction with the reducing gases (test gases) such as H_2 etc and releases electrons in the process. The electron produced in the reaction process, goes into the conduction band of the sensor material and thus the *n*-type semiconductor gas sensors exhibit a decrease in the

resistance in presence of a reducing gas. A simplified outline of the reactions involved in the sensors mechanism is given below.

$$O_2(g) + e^- \rightarrow O^-_{2\,(ads)}$$

$$O^-_{2\,(ads)} + e^- \rightarrow 2O^-_{(ads)}$$

$$R + O^-_{ads} \rightarrow RO + e^-$$

In this reaction, R denotes the reducing gas.

Recent researches have however, shown that simple binary metal oxides cannot always fulfill the demands of a perfect gas sensing matrix. As an alternative, complex, multi-component metal oxides based materials are gaining attention as potential contenders for gas sensor applications (Golovanov *et al.* 2001; Meixner *et al.*, 1996; Yamazoe *et al.*, 1992; Zakrzewska, 2001) since in many cases, they have been realized to circumvent the limitations like low sensitivity, slow response and recovery time etc. posed by the simple metal oxides. The properties of the system undergo change when pure components combine to form solid-solutions/mixed oxide compositions. For instance, compared to the respective pure oxide systems their solid-solutions or mixed oxide compositions would undergo modifications in both, the bulk electronic structure (Zakrzewska, 2001) as well as in the surface properties. In the case of mixed metal oxide systems, concentration of charge carriers, chemical and physical properties of the oxide matrix, bulk electronic structure, the band gap, Fermi level position, etc., experience important changes. Electronic and physicochemical properties of the surface such as, the energy of adsorption and desorption, sticking coefficients, surface potential and inter-crystallite barriers, are expected to be significantly influenced by new boundaries between grains having different chemical compositions. It is thus anticipated that all these phenomenological changes, brought about by mixing pure components, would contribute advantageously towards the gas sensing mechanism in the system and hence would be favored for technological applications.

In the last decade, simple binary metal oxides along with a number of ternary, quaternary and complex metal oxides, mostly belonging to the titanate, stannate, niobate, tantalate, gallate, and ferrite families have been synthesized and they have been reported to show good gas sensing behavior.

A very popular dielectric ceramic oxide, $BaTiO_3$ has also been well known as good gas sensor material. Haeusler *et al.* (1996) have developed $BaTiO_3$ for application as an effective carbon dioxide sensor. They have synthesized $BaTiO_3$ using solid-state reaction. Zhou *et al.* (2003) have investigated the role of defects in La doped $BaTiO_3$ towards sensing an atmosphere of carbon monoxide gas.

The gas sensitivity of $BaSnO_3$ has been extensively investigated. The responses of $BaSnO_3$ with and without modification by doping with different additives have been investigated towards carbon monoxide (Lampe *et al.*, 1995), hydrogen sulfide (Jayaraman *et al.*, 1996), liquefied petroleum gas (Reddy *et al.*, 1999). Other stannate systems such as, $Bi_2Sn_2O_7$ with pyrochlore structure have been reported to exhibit the sensitivity towards carbon monoxide (Adamian *et al.*, 1996).

Among different transition metal niobate compositions, $FeNbO_4$ has been investigated for its gas sensing behavior towards chlorine (Dawson *et al.*, 1996), carbon monoxide (Henshaw *et al.*, 1996), hydrogen sulfide, liquefied petroleum gas, and hydrogen (Gnanasekar *et al.*, 1999). In these studies, $FeNbO_4$ has been prepared through conventional solid-state reactions. Gnanasekar *et al.* (1999) have prepared $FeNbO_4$ through mixing the stochiometric amounts of α-Fe_2O_3 and Nb_2O_5 followed by heat treatment at 1000 ºC in air for about 24 h by repetitions two times. $FeNbO_4$ comprising of two transition metal ions, having similar ionic radii but different valence states, exhibit semiconducting behavior.

Moseley *et al.* (1988) have prepared different transition metal tantalate compositions such as, $FeTaO_4$ with rutile structure, $CoTa_2O_6$ and $NiTa_2O_6$ with trirutile structures, and $CuTa_2O_6$ with perovskite structure by solid-state method and studied their gas sensing behaviors towards different gases such as chlorine, nitrogen dioxide, sulfur dioxide, hydrogen sulfide, carbon monoxide, methane. The gas sensing

characteristics of transition metal tantalates have shown a variety of behavior, which may be useful in the preparation of semiconductor gas detectors with improved characteristics over tin dioxide devices.

It has been seen that the reduction of the crystallite size in a sensor material brings about substantial improvement in the sensor properties. In the early 1990s Yamazoe and coworkers (Tamaki *et al.*, 1994; Xu *et al.*, 1991a; Xu *et al.*, 1991b) have presented systematic investigations to realize whether nanocrystalline metal oxides increase the sensitivity. They have found a strong correlation between grain diameter and sensitivity (Xu *et al.*, 1991b). In case of SnO_2, for particle sizes below 10 nm, the sensitivity has been reported to have increased drastically. Liu and coworkers (1997) have observed that nanocrystalline α-Fe_2O_3 exhibits reasonable sensitivity to ethanol whereas large particles of α-Fe_2O_3 exhibit almost no sensitivity to ethanol. Chu *et al.* (1999a) have reported similar phenomenon using a complex oxide, nanocrystalline $CdIn_2O_4$, which exhibits good sensitivity towards ethanol, while the coarse particles of $CdIn_2O_4$, prepared by a solid-state method at high temperature, have been found to be insensitive towards ethanol.

Nanotechnology presents provisions for enhancing the properties and performance (such as: high sensitivity, low operating temperature) of gas sensors. The sensitivity of metal oxide sensors to the test gases is intimately related to the grain size, surface morphology, surface area, and internal porosity of the sensor materials. Nanocrystalline mixed oxide based gas sensor materials exhibit improved sensitivity owing to their small particle size, high surface to volume ratio, and a high density of low-coordinated surface sites compared to their corresponding bulk counterparts. Morrison (1987) has pointed out that the gas-sensing phenomenon is a sort of the surface catalyzed combustion. Nanocrystalline mixed oxide particles give rise to high surface area and thus a large fraction of atoms get accommodated at the surface or the interface region compared to the bulk and large volume of analytes or gas molecules can come in contact with surface sites/atoms for surface chemical reaction in greater extent. Hence, nanocrystalline gas sensor materials show improved sensitivity compared to their bulk counterparts.

However, the main effect is associated with the width of the surface charge depletion region produced around surface of the particles due to gas adsorption, in relation to the particle size. Chemisorbed of O_2 gas molecules on the oxide surface get dissociate to O_2^- or O^- species, taking electrons from the oxide lattice resulting in a surface depleted layer, which leads to a decrease in near-surface conductivity.

The surface depletion layer for an *n*-type semiconductor gas sensor can be expressed in terms of the Debye length (L_D), which is defined as (Xu *et al.*, 1991c):

$$L_D = \left(\frac{\varepsilon_o KT}{n_o e^2}\right)^{\frac{1}{2}}$$

Where, ε_o is the static dielectric constant, n_o is the total carrier concentration, e is the carrier charge, K is the Boltzmann constant, T is the absolute temperature.

Xu *et al.* (1991b) have proposed a semiquantitative model to explain the effect of grain/particle size on the sensitivity of metal oxide gas sensors. They have shown with their model that the maximum sensitivity is achieved whenever the Debye length is about half the grain size. Under this condition (when grain size $D \leq 2L_D$), the depletion region extends throughout the whole grain and the crystallites are almost fully depleted of mobile charge carriers and as a result the conductivity decreases steeply. It is often asserted that gas sensitivity should increase with increasing electric resistance in the sensor elements. This is based on the grounds that a change in concentration of conduction electrons due to the reaction of the chemisorbed O_2^- or O^- species with the analyte gas on the sensor surface would bring about a larger resistance change in the sensor material, which has higher resistance compared to the sensor material having low resistance (Xu *et al.*, 1991c). In this conduction regime, the sensitivity (S) is related to the change in the carrier concentration (Δn) and is given by

$$S = \frac{\Delta n}{n_o} L_D$$

The optimum sensitivity is obtained in a material with small grain sizes, large Debye lengths, and relatively low carrier concentration (Cosandey *et al.*, 2000).

In recent years, a variety of nanocrystalline mixed oxides are being synthesized through wet chemical methods for successful application in gas detections. Chu *et al.* (1999b) have developed nanocrystalline powders of $CoTiO_3$ powders for detecting ethanol gas. The oxide composition, prepared through coprecipitation method, exhibited high sensitivity, good selectivity and fast response time towards ethanol gas. Siemons *et al.* (2006) have reported the doping effect of various metals (Au, Ce, Ir, Pd, Pt, Rh, Ru) onto the nanocrystalline La containing $CoTiO_3$ matrix for fast detection of ethanol, propylene and NO_2 gas. The same group (Siemons *et al.*, 2007) has also shown that the *p*-type mixed oxide composition, $CoTiO_3$ doped with Gd, Ho, K, La, Li, Na, Pb, Sb, and Sm, synthesized by polyol assisted synthesis method are good sensor materials for fast detection of ethanol and propylene gases.

Tao *et al.* (2000) have prepared the $BaSnO_3$ powder with perovskite structure by the coprecipitation technique. The fine powders of $BaSnO_3$ have been found to be a promising ethanol-sensing material. The gas sensing mechanism of $BaSnO_3$ has been demonstrated as a surface controlled process. Other stannate systems such as $ZnSnO_3$ and $Bi_2Sn_2O_7$ have been prepared and investigated for their sensitivity towards different test gases. Nanoparticles of $ZnSnO_3$ synthesized through hydrothermal method have shown high sensitivity towards hydrogen sulfide (Xu *et al.*, 2006). Yu-Sheng, *et al.* (1993) have prepared ultramicro-size particles of $ZnSnO_3$ by the coprecipitation method and shown that the oxide composition is a good ethanol sensor.

A number of ferrite systems such as $NiFe_2O_4$, $MgFe_2O_4$, $ZnFe_2O_4$, $CuFe_2O_4$ and $CdFe_2O_4$ have been developed for gas sensor applications. Baruwati *et al.* (2007) have prepared $NiFe_2O_4$ composition with particle size in the range of 10-12 nm through the hydrothermal route. They have demonstrated that $NiFe_2O_4$ exhibits both *n*-type and *p*-type conductivity depending on the pH conditions of the reaction medium maintained during synthesis. When pH of the reaction medium is maintained

between 7 and 8 the material is found to exhibit *n*-type conductivity while pH of the reaction medium is kept between 9 and 11, the materials show *p*-type conductivity. The behavior of the synthesized $NiFe_2O_4$ composition has been studied in presence of liquefied petroleum gas. Liu *et al.* (2004) have reported that Au, Pt or Pd, impregnated $NiFe_2O_4$ with different concentrations show excellent sensor response and selectivity to H_2S gas. The sensors based on nanocrystalline $MgFe_2O_4$ are reported to have good sensitivity towards ethanol gas (at operational temperature 335 ºC) and towards H_2S (at operational temperature 160 ºC) at different operational temperatures (Liu *et al.*, 2005). The sensors based on nanocrystalline $CuFe_2O_4$ are reported to show the optimum response towards C_2H_5OH at 332 ºC with good reproducibility and with response time in seconds (Sun *et al.*, 2007).

For gas sensing studies, nanocrystalline $LaFeO_3$ powders as well as various bivalent metal ions (such as: Sr, Pb, Ni, Mg etc) doped nanocrystalline $LaFeO_3$ powders have been prepared through citrate gel method (Jagtap *et al.*, 2008; Liu *et al.*, 2007; Suo *et al.*, 1997; Zhang *et al.*, 2005). Wang *et. al.* (2006) have prepared single crystalline $LaFeO_3$ nanotubes through two-step method: co-precipitation followed by molten-salt synthesis. The synthesized $LaFeO_3$ nanotubes show good sensing properties towards Cl_2 gas at room temperature. The substitution of some fraction of La in $LaFeO_3$ by different bivalent metal ions (such as: Sr, Pb, Ni, Mg etc.) helps to reduce the resistance of the material and improve the response towards ethanol vapor. Jagtap *et al.*, (2008) have reported that lanthanum ferrites with the composition, $La_{0.7}Pb_{0.3}Fe_{0.4}Ni_{0.6}O_3$ have good response towards hydrogen sulfide.

Zhang *et al.* (2006) have carried out the experiments to study the gas sensing behavior of MCo_2O_4 (M = Ni, Cu, Zn) nanotubes. They have observed high sensitivity of these materials towards ethanol and sulfur dioxide gases. The mixed valences of the cations in these composite oxides assist in reversible adsorption of gases by providing donor-acceptor sites for chemisorptions.

From the up-to-date literature review, it is observed that transition metal niobate and gallate systems have not been extensively investigated for their gas sensing properties. Although among the transition metal niobate, the bulk $FeNbO_4$

system has been investigated for its gas sensing properties but similar studies using nanocrystalline $FeNbO_4$ does not feature in recent literature. Of the transition metal gallates, only bulk $ZnGa_2O_4$ and Mg doped $CdGa_2O_4$ systems have been reported for their gas sensing applications. No literature report exist involving gas sensing behavior of nanocrystalline transition metal gallates. Scarcity of information on the nanocrystalline transition metal niobates and gallates systems has prompted our research in the synthesis of these oxides and studies their gas sensing behaviors towards different toxic and inflammable gases.

1.5 Pigments

The word "pigment" originates from the Latin word "pigmentum" and originally denoted a color in the sense of a coloring matter, but was later extended to indicate colored decoration. The word pigment is also used in biological terminology to mean dyestuffs of plant or animal organisms that occur as very small grains inside the cells or cell membranes, as deposits in tissues, or suspended in body fluids.

Today, the word pigment, which originated in the 20th century, means a substance consisting of small particles that is practically insoluble in the applied medium and is used because of its coloring and protective properties. Pigments are characterized by their chemical compositions, and by their optical or technical properties.

Pigments are of two kinds: inorganic and organic. Organic color pigments are generally brighter, purer, and richer in color than their corresponding colored inorganic counterparts. However, they are also generally more susceptible to degrading under the influence of sunlight, weather, chemical attack and heat. Furthermore, organic color pigments are usually more expensive. Following table (Table 1.2) provides the difference in properties associated with organic and inorganic pigments.

Table 1.2: *Traditional properties associated with inorganic and organic properties*

Properties/Origin	**Inorganic**	**Organic**
Derivation	Minerals	Organic materials
Color	Often dull	Bright
Light fastness	Very good	Poor to very good
Solubility	Insoluble in solvent	May have solubility
Chemical, thermal and photochemical stability	Good	Moderate
Cost	Moderate	Can be very expensive

Pigments are mostly used in paints, varnishes, plastics, artists' colors, printing inks for paper and textiles, leather decoration, building materials (such as: cement, renderings, concrete bricks and tiles), imitation leather, rubber, paper, cosmetics, ceramic glazes, and enamels. Iron oxide and chromium oxide pigments have been in use for thousands of years. Pigments express color, emotions, thoughts and distinctiveness. The paint industry almost exclusively uses high-quality pigments every day. Effectiveness, economy and ecology determine the quality of pigments. Better effectiveness, which indicates the technical performance of pigments, includes improved fineness on grind, easy dispersibility in medium, better tinting strength etc. Better economy gives the consumers enhanced value-in-use and better ecology involve environmental and toxicological safety.

1.5.1 Inorganic Pigments

Natural inorganic pigments, derived mainly from mineral sources, have been used as colorants since antiquity. In the 20th century, pigments increasingly became the subject of scientific investigation. In the past few decades, the colored pigments such as cadmium red, manganese blue, molybdenum red and mixed oxides with bismuth were synthesized and came onto the market. Titanium dioxide with anatase or rutile structures, and acicular zinc oxide were introduced as new synthetic white pigments and extenders respectively.

With few exceptions, inorganic pigments usually include the oxides, sulfides, hydroxides, silicates, sulfates and carbonates of metals and normally consist of single component particles (e.g., red iron oxide, Fe_2O_3) with well-defined crystal structures. Notwithstanding that most inorganic pigments are familiar for a very long time, new developments appear for the improvement of colors. The so-called "high performance pigments" (Smith, 2002) show a lot of modern developments, although a small number of really new compounds have been developed in recent decades. This is because of inadequacy in available chemistry for the development of high performance inorganic pigments. It is possible the development of new manufacturing processes for 'old' pigments and enhancement of their properties might well renovate these products to join the positions of truly high performance pigments.

Color in inorganic oxide pigments is somewhat difficult to explain, partly because no single theory fully accounts for the color that is observed. The main cause of color of such metal oxide pigments is due to charge transfer spectra and/or *d-d* transition spectra, especially of the pigments comprising 3*d* transition metals. However, this is not the explanation for all colored inorganic oxide pigments. The crystal structure coupled with particle size is also responsible for the color of such pigments.

1.5.2 Metal Oxide Based Pigments

There is a steadily increasing requirement for more durable pigments to color products such as paints, plastics, building materials and ceramics. As a consequence, the inorganic pigments are of increasing importance to the paint formulators. Metal oxides are the most important members of the inorganic family.

Metal oxide pigments are those pigments which crystallize in stable oxide lattice and the color is imparted by the cations within the lattice. Pigments with rutile, spinel and hematite structures represent the most important category of metal oxide based inorganic pigments. They all have very good chemical and thermal stability,

high refractive indices, insolubility (bleed resistance), easy dispersibility, and compatibility with most resins and aqueous systems to give unsurpassed performance.

1.5.2.1 Mixed Metal Oxide Based Pigments

A variety of mixed metal oxide compositions (especially, those containing the transition metals ions) are also being pursued for their applications as high performance pigments. These mixed metal oxides, composed of two or more different metal ions, belong to an important family of pigments, known as the 'complex inorganic color pigments' (CICPs). Chemically, these pigments are synthetic crystalline metal oxides that have structures identical to those of naturally occurring minerals such as, rutile, hematite or corundum and spinel. The pigments of this CICPs family are called complex because they are mixed oxides composed of two or more different metal oxides. These pigments were formerly referred to as mixed metal oxide (MMO) pigments, a term that is still widely used even today. The mixed metal oxides are calcined pigments (final step of synthesis process involves slow heat treatment of the compositions at about 1000 ºC) developed originally for ceramics. These pigments have excellent weatherability and heat stability. Among such multi-component mixed crystal systems, transition metal ions doped titanium dioxide compositions with rutile structure have been recognized as promising candidates for pigment applications featuring interesting color shades in different color range.

Colored mixed metal oxide pigments with rutile structure, which are typically referred as "rutile mixed oxide" pigments or simply as "Titanate" pigments, are characterized by the rutile crystal structure and include at least two different metal oxides in their compositions. Typically, titanium dioxide is the major constituent of such mixed oxide pigments. The colors of rutile mixed oxide pigments are obtained by incorporating a color-producing transition metal ion such as nickel or chromium with low oxidation state into the rutile crystal structure of host titanium dioxide. The rutile mixed oxide pigments additionally include metal ions (such as niobium or

tungsten) that exhibit high oxidation states to achieve electroneutrality in the composition.

1.5.3 Nanocrystalline Mixed Metal Oxide Pigments

The important physical data for inorganic oxide pigments comprise particle size and particle size distribution. The *specific surface area* also represents a mean of the pigment particle size distribution. It can be used to calculate the mean diameter of the surface distribution. It is a well known fact that the color strength of the product increases as it gets subjected to further grinding. From this practical evidence it is believed that the color strength of a pigment increases as its particle size is reduced (Carr, 1973).

Because of high surface area, nanocrystalline mixed oxide based pigment materials are also commercially potent in the pigment industries (Biswas *et al.* 2008). High surface area of the pigment ensures higher surface coverage, higher number reflectance points and hence maximum scattering. Moreover, small sizes of the pigment particles facilitate their uniform dispersion and homogenous mixing with the binders in paint formulations, which in turn enhance the mechanical strength of the coating after drying of the paint.

Considerable effort in research is being devoted for finding the best way to make pigments with optimum physical properties. The invention of new pigments and the improvement of the already existing pigments in this class in the last decade have made new color effects available on an industrial scale. Unfortunately, very little information is available in this field in the open literature since most of the available methodologies are furiously protected by patents laws. The preparation of these inorganic oxide pigments have mainly been reported through the conventional solid-state method (Dondi *et al.*, 2006; Huguenin *et al.*, 1998; Ramos *et al.*, 1991; Sorlí *et al.*, 2004; Tavala *et al.*, 1977), which require several processing steps such as, initial ball milling of the raw materials (usually metal oxides and/or salts) for homogenization; repeated heat treatment of the raw materials at high temperature

(1100–1200 ºC) to obtain the desired crystalline phases and colors; and finally, wet milling to the reduce particle size. The solid-state method usually results in coarse-grained and agglomerated particles.

Solution-based chemical methods of preparation of the oxide solid solutions in contrast are attractive alternative to the conventional solid-state synthesis technique. They not only have the advantage of reduced processing steps but also ensure a precise control of composition and stoichiometry in multicomponent formulations, phase purity in the final product, and better control of particle size in the final powders through molecular level mixing of the starting compounds in solution. They also provide uniformly distributed particles (Alfred *et al.*, 2003) with average grain sizes in nanometer regime, which are difficult to achieve through the convetional solid-state method. In recent years, there have been few publications on the synthesis of fine particles of various mixed metal oxide pigment compositions through the polymeric precursor routes.

Oliveira *et al.* (2008) have prepared wolframite structured $Zn_xNi_{1-x}WO_4$ pigments through the Pechini process, which involved chelation of the cations by a hydrocarboxylic acid (normally citric acid) followed by polyesterification using a glycol (normally ethylene glycol), which appeared as gel. Calcination of the gel resulted in nanocrystalline powders of $Zn_xNi_{1-x}WO_4$ with wolframite structure and a yellow color.

A number of different mixed oxide pigments have been prepared by this polymeric precursor method developed by Pechini. As for example, very recent literature reviews show that nanocrystals of $CoAl_2O_4$ (Chao *et al.*, 1999), Zirconium Titanate (Bianco *et al.*, 1998), the praseodymia-doped ceria (Santos *et al.,* 2007), $MgFe_2O_4$ (Candeia *et al.*, 2006), $CaFe_2O_4$ (Candeia *et al.*, 2004), nanosized TiO_2 and Al_2O_3 powders (Bernardi *et al.*, 2007), $LaFeO_3$ (Cunha *et al.*, 2005) have also been synthesized by the Pechini method or citrate-gel method for pigment applications.

Aruna *et al.* (2001) have reported the synthesis of $Ce_{1-x}Pr_xO_{2-\delta}$ (x=0.01–0.5) red pigments, with crystallite size in the range of 30-40 nm through thermal

decomposition of $Ce_{1-x}Pr_x(N_2H_3COO)_3.3H_2O$ precursor and combustion of aqueous solutions containing cerous nitrate and oxalyl dihydrazide/ammonium acetate mixture. The preparative method is advantageous for the synthesis of inorganic pigment since the process maintains homogeneity, good stoichiometry control, and purity in the final products.

1.6 Objectives and Scope of the Present Work

Since nanocrystalline powders enhance both, the gas sensing as well as the pigmentary properties in different metal oxide compositions hence the aim of this research is to develop and establish a versatile synthetic methodology that can be used for the preparation of nanocrystalline powders of a variety of metal oxide systems. In the present research work, a versatile chemical synthesis technique has been proposed for the preparation of nanocrystalline powders of a variety of different mixed metal oxide compositions (that can be either used as gas sensors or, as pigments) that involves thermal decomposition of aqueous precursor solutions of the desired metal ion-ligand complexes in appropriate mole ratios. The complexing agents used for obtaining the water-soluble, metal ion-ligand complexes are TEA, oxalic acid, EDTA and tartaric acid. The as-prepared powders have been calcined at their respective crystallization temperatures and studied for their gas sensing or, their pigment properties.

The objective of the present investigation is to establish the proposed chemical synthetic technique through preparation of various metal oxide compositions that are listed below, followed by characterization of the powders and study of their respective properties. The objective may be summarized as follows:

Sl.No.	Prepared metal oxide compositions	Property studied
1.	Nanocrystalline powders of: $CuNb_2O_6$; $CuGa_2O_4$; $FeNbO_4$ and Pt impregnated nanocrystalline powders of $FeNbO_4$	• Gas sensing property through Electrical conductivity measurements in dry air. • Gas sensing property towards reducing gases like hydrogen, liquefied petroleum gas (LPG), and ammonia.
2.	Nanocrystalline powders of $Ni_{0.1}W_{0.1}Ti_{0.8}O_2$; $NiBaTi_7O_{16}$; and $Cr_{2x}W_xTi_{1-3x}O_2$ (x = 0.05, 0.1, 0.15)	• UV-visible Absorption Spectroscopy • Color measurement

- Thermal decomposition behavior of the as-prepared, virgin precursor (i.e., pre-calcined) powders for all the prepared mixed oxide compositions have been carried out through simultaneously recorded thermogravimetric and differential thermal analysis (TG/DTA).
- Structure and morphology of the synthesized mixed oxide compositions of the calcined powders have been investigated through X-ray powder diffraction (XRD) studies, transmission electron microscopy (high resolution/low resolution) (HRTEM/TEM), and scanning electron microscopy (SEM).
- Chemical compositions of the synthesized mixed oxides have been substantiated through energy dispersive X-ray analysis (EDAX).

References

Adamian, Z. N., Abovian, H. V. and Aroutiounian, V. M. (1996), Smoke Sensor on the Base of Bi_2O_3 Sesquioxide, Sensors and Actuators B: Chemical, Vol. 35-36, pp. 241–243.

Al-Abadleh, H. A. and Grassian, V. H. (2003), Oxide Surfaces as Environmental Interfaces, Surface Science Reports, Vol. 52, No. 3-4, pp. 63-161.

Alfred, S. and Adriana, U. (2003), Electronic Study of Doping TiO_2 Catalysts Doping with Higher Valence Ions (WO_3) and Variable Valence Ions (Cr_2O_3). Prog. Catal. 12 (1) 51–69.

Aruna, S.T., Ghosh, S. and Patil K.C. (2001), Combustion Synthesis and Properties of $Ce_{1-X}Pr_xO_{2-\Delta}$ Red Ceramic Pigment,. International Journal of Inorganic Materials, Vol. 3, pp. 387–392.

Barker, T. F., Fatehi, L., Lesnick, M. T., Mealey, T. J. and Raimond, R. R. (2008), Nanotechnology and the Poor: Opportunities and Risks for Developing Countries, Nanotechnology and Society, Netherlands, Springer, pp. 243-263.

Baruwati, B., Rana, R. K. and Manorama, S. V. (2007), Further Insights in the Conductivity Behavior of Nanocrystalline $NiFe_2O_4$ in Presence of Liquefied Petroleum Gas, Journal of applied physics, Vol. 101, pp. 0143021-01430217.

Bäumer, M. and Freund, H.-J. (1999), Metal Deposits on Well-Ordered Oxide Films. Progress in Surface Science, Vol. 61, No. 7-8, pp.127-198.

Bernardi, M. I. B., Vicente, F. S. D, Li, M. S and Hernandes, A. C. (2007), Colored Films Produced By Electron Beam Deposition From Nanometric TiO_2 and Al_2O_3 Pigment Powders Obtained By Modified Polymeric Precursor Method, Dyes and Pigments, Vol. 75, pp. 693-700.

Bianco, A., Paci, M. and Free, R. (1998), Zirconium Titanate: from Polymeric Precursors to Bulk Ceramics, Journal of the European Ceramic Society, Vol. 18, pp. 1235-1243.

Bourgeat-Lami, E. (2002), Organic-Inorganic Nanostructured Colloids, Journal of Nanoscience and Nanotechnology Vol. 2, No. 1, pp.1-24.

Biswas, S. K., Dhak, D., Pathak, A. and Pramanik, P. (2008), Chemical Synthesis of Environment-Friendly Nanosized Yellow Titanate Pigments, Materials Research Bulletin, Vol. 43, No. 3, pp. 665-675.

Brattain, W.H. and Bardeen, J. (1952), Surface Properties of Germanium, Bell System Technical Journal, Vol. 32, pp. 1-5.

Burda, C., Chen, X., Narayanan, R. and El-Sayed, M. A. (2005), Chemistry and Properties of Nanocrystals of Different Shapes, Chemical Review, Vol. 105, pp. 1025-1102.

Candeia, R. A., Bernardi, M. I. B., Longo, E., Santos, I.M.G., Souza A.G., (2004), Synthesis and Characterization of Spinel Pigment $CaFe_2O4$ Obtained by The Polymeric Precursor Method, Materials Letters, Vol. 58, pp. 569– 572.

Candeia, R. A., Souza, M. A. F., Bernardi, M. I. B., Maestrelli, S.C., Santos, I. M. G., Souza, A. G. and Longo, E. (2006), $MgFe_2O_4$ Pigment Obtained at Low Temperature, Materials Research Bulletin, Vol. 41, pp. 183–190.

Cao, G. (2004), Nanostructures & Nanomaterials: Synthesis, Properties & Applications, Lodon, UK, Imperial College Press.

Carr, W. (1973), Pigments Powders and Dispersions: Measurements And Interpretation of Their Physical Properties. Patton, T. C. (Editor), Pigment Handbook, Vol. 3, pp. 11-27.

Choa, W.-S. and Kakihana, M. (1999), Crystallization of Ceramic Pigment $CoAl_2O_4$ Nanocrystals from Co-Al Metal Organic Precursor, Journal of Alloys and Compounds Vol. 287, pp. 87–90.

Chu, X., Liu, X. and Meng, G. (1999a), Preparation and Gas-Sensing Properties of nano-$CdIn_2O_4$ material, Materials Research Bulletin, Vol. 34, No. 5, pp. 693-700.

Chu, X., Liu, X., Wang, G. and Meng, G. (1999b), Preparation and Gas-Sensing Properties of Nano-$CoTiO_3$, Materials Research Bulletin, Vol. 34, No. 10-11, pp. 1789-1795.

Cosandey, F., Skandam,G. and Singhal, A. (2000), Materials and Processing Issues in Nanostructured Semiconductor Gas Sensors, JOM-e, Vol. 52, No. 10. [http://www.tms.org/pubs/journals/JOM/0010/Cosandey/Cosandey-0010.html]

Cunha, J. D., Melo, D. M. A., Martinelli, A. E., Melo, M. A. F., Maia, I. and Cunha S. D. (2005), Ceramic Pigment Obtained By Polymeric Precursors. Dyes and Pigments, Vol. 65, pp. 11-14.

Cushing, B. L., Kolesnichenko, V. L., and O'Connor, C. J. (2004), Recent Advances in the Liquid-Phase Syntheses of Inorganic Nanoparticles, Chemical Review, Vol. 104, No. 9, pp. 3893-3946.

Dawson, D. H. and Williams, D. E. (1996), Gas-Sensitive Resistors: Surface Interaction of Chlorine with Semiconducting Oxides, Journal of Materials Chemistry, Vol. 6, No. 3, pp. 409-414.

Dondi, M., Cruciani, G., Guarini, G., Matteucci, F. and Raimondo, M. (2006), The Role of Counterions (Mo, Nb, Sb, W) in Cr-, Mn-, Ni- and V-Doped Rutile Ceramic

Pigments: Part 2. Colour and Technological Properties. Ceramics International, Vol. 32, No. 4, pp. 393-405.

Drexler, K. E. (1981), Molecular engineering: An Approach to The Development of General Capabilities for Molecular Manipulation, Proceedings of the National Academy of Sciences, Vol. 78, No. 9, pp. 5275-5278. http://www.imm.org/PNAS.html.

Drexler, K. E. (1986), 'Engines of Creation: The Coming Era of Nanotechnology, New York: Anchor Press/Doubleday 4.

Ertl, G., Knözinger, H. and Weitkamp, J. (1997), Hand book of Heterogeneous Catalysis, Vol. 5, Weinheim, Wiley-VHC.

Faraday Discussion (1999), The Surface Science of Metal Oxides, Vol. 114, pp. 1-465.

Feng, X. and Hu, M. Z. (2004), Ceramic Nanoparticle Synthesis, Encyclopedia of Nanoscience and Nanotechnology, Edited by H. S. Nalwa, Vol. 1, pp. 687-726.

Fernández-García, M., Martínez-Arias, A., Hanson, J. C. and Rodriguez, J. A. (2004), Nanostructured Oxides in Chemistry: Characterization and Properties, Chemical Review, Vol. 104, pp. 4063-4104 (References therein).

Feynman, R.P. (1960), There's Plenty of Room at the Bottom, Engineering and Science, Vol. 23, pp. 22–26, 30, 34, and 36. Feynman R. P. (1961), There's Plenty of Room at the Bottom, Miniaturization, (Gilbert H D. Ed.), Reinhold, New York, pp. 282-296.

Gnanasekar, K.I., Jayaraman, V., Prabhu, E., Gnanasekaran, T. and Periaswami, G. (1999), Electrical and Sensor Properties of $FeNbO_4$: A New Sensor Material, Sensors and Actuators B, Vol. 55, 170-174.

Gleiter, H. (1989), Nanocrystalline Materials. Progress in Materials Science, Vol. 33, pp. 223-315.

Gleiter, H. (1995), Nanostructured Materials: State of The Art and Perspectives, Nanostructured Materials, Vol. 6, NO. 1-4, pp. 3-14.

Golovanov, V., Smyntyna, V., Korotcenkov, G. and V. Brinzari, (2001) Cd_xS and Sn_xWO_3 Based Gas Sensors: The Role of Chemical Composition in CO Sensing, Journal of Potoelectronics (Ukraine), Vol. 10, pp. 6–11.

Haeusler, A. and Meyer, J.-U. (1996), A Novel Thick Film Conductive Type CO_2 Sensor, Sensors and Actuators B: Chemical, Vol. 34, No. 1-3, pp. 388-395.

Henshaw, G. S., Morris, L., Gellman L. J. and Williams, D. E. (1996), Selectivity and Compositional Dependence of Response of Gas-Sensitive Resistors Part 4.-Properties

of Some Rutile Solid Solution Compounds, Journal of Materials Chemistry, Vol. 6, No. 12, pp. 1883-1887.

Hu, E. L. and Shaw, D. T. (1999), Synthesis and Assembly in "Nanostructure Science and Technology, R&D Status and Trends in Nanoparticles, Nanostructured Materials, and Nanodevices, Editors: Siegel, R. W., Hu, E. and Roco, M. C., Chapter 2, pp. 15-33.

Huguenin, D. and Chopin, T. (1998), New Titanium Precursors For Manufacture of Colored Pigments, Dyes and Pigments, Vol. 37, No. 2, pp. 129–134.

Jagtap, S.V., Kadu, A.V., Sangawar, V.S., Manorama, S.V., Chaudhari, G. N. (2008), H_2S Sensing Characteristics of $La_{0.7}Pb_{0.3}Fe_{0.4}Ni_{0.6}O_3$ Based Nanocrystalline Thick Film Gas Sensor, Sensors and Actuators B: Chemical, Vol. 131, pp. 290–294.

Jayaraman, V., Mangamma, G., Gnanasekaran, T. and Periaswami, G. (1996), Evaluation of $BaSnO_3$ and $Ba(Zr,Sn)O_3$ Solid Solutions as Semiconductor Sensor Materials, Solid State Ionics, Vol. 86-88, No. 2, pp. 1111-1114.

Koch, C.C. (1989). Materials Synthesis by Mechanical Alloying, Annual Review of Materials Science, Vol. 19, pp. 121-143.

Komarneni, S. (2003), Nanophase Materials by Hydrothermal, Microwave-Hydrothermal and Microwave-Solvothermal Methods, Current Science, Vo. 85, No. 12, pp. 1730-1734.

Kourtakis, K. (2002), High Surface Area Sol-Gel Route Prepared Oxidation Catalysts, United States Patent 6413903.

Lampe, U., Gerblinger, J., Meixner, H. and Siemens, A. G, (1995), Carbon Monoxide Sensors Based on Thin Films of $BaSnO_3$, Sensors and Actuators, B: Chemical, Vol. 25, No. 1-3, pp. 657-660.

Liu, X., Cheng, B., Qin, H., Song, P., Huang, S., Zhang, R., Hu, J. and Jiang, M. (2007), Preparation, Electrical and Gas-Sensing Properties of Perovskite-Type $La_{1-x}Mg_xFeO_3$ Semiconductor Materials, Journal of Physics and Chemistry of Solids, Vol. 68, pp. 511–515.

Liu, X. Q., Tao, S.W. and Shen, Y.S. (1997), Preparation and Characterization of Nanocrystalline α-Fe_2O_3 by a Sol-Gel Process, Sensors and Actuators B: Chemical, Vol. 40, No. 2-3, pp. 161-165.

Liu, Y.-Li., Wang, H., Yang, Y., Liu, Z.-M., Yang, H.-F., Shen, G.-L. and Yu, R.-Q. (2004), Hydrogen Sulfide Sensing Properties of $NiFe_2O_4$ Nanopowder Doped with Noble Metals, Sensors and Actuators B: Chemical, Vol. 102, pp. 148–154.

Liu, Y.-Li., Liu, Z.-M., Yang, Y., Yang, H.-F., Shen, G.-L. and Yu, R.-Q. (2005) Simple Synthesis of $MgFe_2O_4$ Nanoparticles as Gas Sensing Materials, Sensors and Actuators B: Chemical, Vol. 107, pp. 600-604.

Lüth, H. (1995), Surfaces and Interfaces of Solid Materials, Berlin, Heidelberg, Springer, Third Edition.

Meixner, H. and Lampe, U. (1996), Metal Oxide Sensors, Sensors and Actuators B: Chemical, Vol. 33, No. 1-3, pp. 198-202.

Morrison, S. R. (1978), The Chemical Physics of Surfaces, Plenum, New York, 2nd edn., pp. 242 - 246.

Morrison, S. R. (1987), Selectivity in Semiconductor Gas Sensors, Sensors and Actuators, Vol. 12, pp. 425–440.

Moseley, P. T., Williams, D. E., Norris, J. O. W. and Tofield, B. C. (1988), Electrical Conductivity and Gas Sensitivity of Some Transition Metal Tantalates, Sensors and Actuators, Vol. 14, No. 1, pp. 79-91.

Ogawa, H., Nishikawa, M. and Abe, A. (1982), Hall Measurement Studies and An Electrical Conduction Model of Tin Oxide Ultrafine Particle Films, Journal of Applied Physics, Vol. 53, pp. 4448-4455.

Oliveira, A. L. M. d., Ferreira, J. M., Silva, M. R. S., Braga, G. S., Soledade, L. E. B., Aldeiza, M.A. M. M., Paskocimas, C. A., Lima, S. J. G., Longo, E., Souz, A. G. d. and Santos, I. M. G. d. (2008), Yellow $Zn_xNi_{1-x}WO_4$ Pigments Obtained Using a Polymeric Precursor Method, Dyes and Pigments, Vol. 77, pp. 210-216.

Pathak, A., Mohapatra, S., Mohapatra S., Biswas, S. K., Dhak, D., Pramanik, N.K., Tarafdar, A. and Pramanik. P. (2004), Preparation of Nanosized Mixed-Oxide Powders, American Ceramic Society Bulletin, Vol. 83, No. 8, pp. 9301-9306.

Pathak, A. and Pramanik, P. (2001), Nano-Particles of Oxides through Chemical Methods, PINSA, Vol. 67, No. 1, pp. 47-70.

Pechni, M. P. (1967), Method of Preparing Lead and Alkaline Earth Titanates and Niobates and Coating Method using the Same to Form A capacitor, United States Patent 3330697.

Ramos, E., Veiga, M. L., Fernández, R., Sáez-Puche, R. and Pico, C. (1991), Synthesis, Structural Characterization, and Two-Dimensional Antiferromagnetic Ordering for the Oxides $Ti_{3(1-x)}Ni_xSb_{2x}O_6$ ($1.0>x>0.6$), Journal of Solid State Chemistry, Vol. 91, pp. 113–120.

Rao, C.N.R. (1994), Sol-Gel Synthesis, in Chemical Approaches to The Synthesis Of Inorganic Materials, Delhi, Wiley Eastern Limited, New Age International Limited, pp. 45-47.

Reddy, C. V. G., Manorama, S. V., Rao, V. J., Lobo, A. and Kulkarni, S. K. (1999), Noble Metal Additive Modulation of Gas Sensitivity of $BaSnO_3$, Explained by A Work Function Based Model, Thin Solid Films, Vol. 348, No. 1, 2, pp. 261-265.

Richards, R., Mulukutla, R. S., Mishakov, I., Chesnokov, V., Volodin, A., Zaikovski, V., Sun, N. and Klabunde, K. J. (2001), Nanocrystalline Ultra High Surface Area Magnesium Oxide as A Selective Base Catalyst. Scripta Materialia, Vol. 44, No. 8-9, pp. 1663-1666.

Rickerbya, D. G. and Morrison, M. (2007), Nanotechnology and the Environment: A European Perspective, Science and Technology of Advanced Materials, Vol. 8, pp. 19-24.

Rodriguez, J. A., Liu, G., Jirsak, T., Hrbek, Chang, Z., Dvorak, J., Maiti, A. (2002) Activation of Gold on Titania: Adsorption and Reaction of SO_2 on Au/TiO_2 (110), Journal of American Chemical Society, Vol. 124, pp. 5242-5250.

Roy, R. (1987), Ceramics by the Solution-Sol-Gel Route, Science, Vol. 238, pp. 1664-1669.

Santos, S.F., Andrade, M.C. d, Sampaio, J.A., Luz, A. B. d and Ogasawara, T. (2007),

Synthesis of Ceria-Praseodymia Pigments by Citrate-Gel Method for Dental Restorations, Dyes and Pigments, Vol. 75, pp. 574-579.

Seiyama, T., Kato, A., Fujiishi, K. and Nagatani, M. (1962), A New Detector for Gaseous Components Using Semiconductive Thin Films, Analytical Chemistry, Vol. 34, No. 11, pp. 1502-1503.

Siemons, M. and Simon, U. (2006), Preparation and Gas Sensing Properties of Nanocrystalline La-doped $CoTiO_3$, Sensors and Actuators B: Chemical, Vol. 120, pp. 110–118.

Siemons, M. and Simon, U. (2007), Gas Sensing Properties of Volume-Doped $CoTiO_3$ Synthesized Via Polyol Method, Sensors and Actuators B: Chemical, Vol. 126, pp. 595–603.

Smith, H. M. (Ed.), High Performance Pigments, Wiley-VCH, Weinheim, 2002.

Sorlí, S., Tena, M.A., Badenes, J.A., Calbo, J., Llusar, M. and Monrós, G. (2004), Structure and Color of $Ni_xA_{1-3x}B_{2x}O_2$ (A = Ti, Sn; B = Sb, Nb) Solid Solutions, Journal of the European Ceramic Society, Vol. 24, pp. 2425–2432.

Spoto, G., Gribov, E. N., Ricchiardi, G., Damin, A., Scarano, D., Bordiga, S., Lamberti, C. and Zecchina, A. (2004), Carbon monoxide MgO from Dispersed Solids to Single Crystals: A Review and New Advances, Progress in Surface Science, Vol.76, No. 3-5, pp. 71-146.

Stambaugh, E. P. and Miller, J. P. (1982), In The Proceeding of the First International Symposium on Hydrothermal Reactions, Gakujutsu Bunken Fukyu-Kai, Tokyo, pp. 859-872.

Sun, Z., Liu, L., Jia, D. z. and Pan, W. (2007), Simple Synthesis of $CuFe_2O_4$ Nanoparticles as Gas-Sensing Materials, Sensors and Actuators B: Chemical, Vol. 125 pp. 144–148.

Suo, H., Wang, J., Wu, F., Liu, G., Xu, B. and Zhao, M. (1997), Influence of Sr Content on the Ethanol Sensitivity of Nanocrystalline $La_{1-x}Sr_xFeO_3$, Journal of Solid State Chemistry, Vol. 130, pp. 152-153.

Taguchi, N. (1970), Japanese Patent 45-38200.

Taguchi, N. (1970), United States Patent 3644795.

Taguchi, N. (1970), United Kingdom Patent 1280 809.

Taguchi, N. (1972), Japanese Patent 47-38840.

Tamaki, J., Zhang, Z., Fujimori, K., Akiyama, M., Harada, T., Miura, N. and Yamazoe, N. (1994), Grain-Size Effects in Tungsten Oxide-Based Sensor for Nitrogen Oxides, Journal of The Electrochemical Society, Vol. 141, pp. 2207-2210.

Taniguchi, N. (1974), On the Basic Concept of 'Nano-Technology', Proc. Intl. Conf. Prod. London, Part II, British Society of Precision Engineering.

Tao, S., Gao, F., Liu, X. and Sørensen O. T. (2000), Ethanol-Sensing Characteristics of Barium Stannate Prepared by Chemical Precipitation, Sensors and Actuators B: Chemical, Vol. 71, No. 3, pp. 223-227.

Tavala, T.P., Brinzan, N.G. and Florea, V. (1977), Red-Brown Pigments in the Cr_2O_3–TiO_2–WO_3 System, Revue Roumaine de Chimie, Vol. 22, No. 5. Pp. 787–792.

Trudeau, M. L. and Ying, J. Y. (1996), Nanocrystalline Materials in Catalysis and Electrocatalysis: Structure Tailoring and Surface, Nanostructured Materials, Vol. 7, No. 1-2, pp. 245-258.

Valden, M., Lai, X. and Goodman, D. W. (1998), Onset of Catalytic Activity of Gold Clusters on Titania with the Appearance of Nonmetallic Properties, Science, Vol. 281, pp. 1647-1650.

Wang, D., Chu, X. and Gong, M. (2006), Single-Crystalline $LaFeO_3$ Nanotubes With Rough Tube Walls: Synthesis and Gas-Sensing Properties, Nanotechnology, Vol. 17, pp. 5501–5505.

Weiss, W. and Ranke, W. (2002), Surface Chemistry and Catalysis on Well-Defined Epitaxial Iron Oxide Layers. Progress in Surface Science, Vol.70, No.1-3, pp. 1-151.

Wyckoff, R. W. G. (1964), Crystal Structures, New York, Wiley, Second Edition.

Xu, C., Tamaki, J., Miura, N. and Yamazoe, N. (1991a), Correlation between Gas Sensitivity and Crystallite Size in Porous SnO_2-Based Sensors, Chemistry Letters, Vol. 19, No. 3, pp. 441-444.

Xu, C., Tamaki, J., Miura, N. and Yamazoe, N. (1991b), Grain Size Effects on Gas Sensitivity of Porous SnO_2-Based Elements, Sensors and Actuators B: Chemical, Vol. 3, No. 2, pp. 147-155.

Xu, C., Tamaki, J., Miura, N. and Yamazoe, N. (1991c), Promotion of Tin Oxide Gas Sensor by Aluminum Doping, Talanta, Vol. 38, No. 10, pp. 1169-1175.

Xu, J., Jia, X., Lou, X. and Shen, J. (2006), One-Step Hydrothermal Synthesis and Gas Sensing Property of $ZnSnO_3$ Microparticles, Solid-State Electronics, Vol. 50, pp. 504–507.

Yamazoe, N. and Miura, N. (1992) New Approaches in the Design of Gas Sensors, in: Gas Sensors, G. Sberveglieri (Editor), Chapter 1, Netherlands, Kluwer Academic Publishers.

Yu-Sheng, S. and Tian-Shu, Z. (1993), Preparation, Structure and Gas-Sensing Properties of Ultramicro $ZnSnO_3$ Powder, Sensors and Actuators B: Chemical, Vol. 12, No. 1, pp. 5-9.

Zakrzewska, K. (2001), Mixed Oxides as Gas Sensors, Thin Solid Films, Vol. 392. Pp. 229-238.

Zhang, L., Hu, J., Song, P., Qin, H., Liu, X. and Jiang, M. (2005), Formaldehyde-Sensing Characteristics of Perovskite $La_{0.68}Pb_{0.32}FeO_3$ Nano-Materials, Physica B, Vol. 370, pp. 259–263.

Zhang, G.-Y., Guo, B. and Chen, J. (2006), MCo_2O_4 (M = Ni, Cu, Zn) Nanotubes: Template Synthesis and Application in Gas Sensors. Sensors and Actuators B: Chemical, Vol. 114, pp. 402–409.

Zhou, Z.-G., Tang, Z.-L. and Zhang, Z.-T. (2003), Studies on Grain-Boundary Chemistry of Perovskite Ceramics as CO Gas Sensors, Sensors and Actuators B: Chemical, Vol. 93, No. 1-3, pp. 356-361.

Chapter 2

Synthesis of Nanocrystalline Powders of $CuNb_2O_6$ and Studies on their Gas Sensing Behavior towards Ammonia, Hydrogen and Liquefied Petroleum Gas

Chapter 2

Synthesis of Nanocrystalline Powders of $CuNb_2O_6$ and Studies on their Gas Sensing Behavior towards Ammonia, Hydrogen and Liquefied Petroleum Gas

2.1 Introduction

There are a number of reports in literature on the synthesis, crystal structure, magnetic and microwave dielectric properties of $CuNb_2O_6$. The structure of $CuNb_2O_6$ comprises of zig-zag chains of edge-sharing CuO_6 octahedra running along the *c*-axis (Kodama *et al.*, 1999). $CuNb_2O_6$ exists in two polymorphs- monoclinic phase and orthorhombic phase. The monoclinic phase is normally present between 700 ºC and 900 ºC (Drew *et al.*, 1995; Wahlström, *et al.*, 1977) while the orthorhombic phase normally exists as a single phase above 900 ºC. Drew *et al.* (1993; 1995) and Koo *et al.* (2001) have studied extensively the magnetic properties of $CuNb_2O_6$. The magnetic properties of $CuNb_2O_6$ originate from the Cu^{2+} (d^9) ions since the other two ions, Nb^{5+} and O^{2-} (ionic electronic counting) are diamagnetic (Koo *et al.*, 2001). Comprehensive studies on the microwave dielectric properties of $CuNb_2O_6$ have been carried out by Pullar *et al.* (2005), which reveal that $CuNb_2O_6$ has a relative permittivity (ε_r) and a temperature coefficient of resonant frequency (τ_f) values of 17.1 and -45.1 ppm respectively. $CuNb_2O_6$ has also been investigated for lithium intercalation reaction by chemical and electrochemical methods (Cruz *et al,* 1999; Sato *et al,* 1995). The lithium intercalation reactions are important for cathode materials for application in secondary lithium batteries.

However, an extensive literature survey shows that the gas sensing behavior of nanocrystalline $CuNb_2O_6$ has not yet been documented in literature. $CuNb_2O_6$ comprises of two transition metal ions having similar ionic radii ($r_{Cu^{2+}}$ = 0.72 Å and $r_{Nb^{5+}}$ = 0.69 Å) but different valence states and exhibits semiconducting behavior similar to other transition metal oxides.

2.2 Reported Methods for the Preparation of $CuNb_2O_6$

$CuNb_2O_6$ has been prepared and investigated by a number of groups where the reported phase for the system predominantly is orthorhombic. Preparations of $CuNb_2O_6$ composition have most commonly been reported through the conventional solid-state method, the use of chemical methods are rare and few. Some of the reported methods of the preparation of $CuNb_2O_6$ are summarized below.

2.2.1 Conventional Solid-State Method

A common technique for the preparation of $CuNb_2O_6$ powders is through the conventional solid-state method, which involves mechanical mixing of stoichiometric amounts of the raw materials (such as, CuO and Nb_2O_5) by repeated milling followed by heat-treatment in air. Most of the reports describe the formation of orthorhombic phase of $CuNb_2O_6$, which requires heat-treatment at high temperature (Cruz *et al,* 1999; Drew *et al.* 1993; Felten, 1966).

Drew *et al.* (1995) have reported the preparation of monoclinic $CuNb_2O_6$ through the conventional solid-state method which involves heating of an intimate mixture of monoclinic *H*-Nb_2O_5 and CuO (1: 1.08) at 700 ºC for 48 h followed by cooling, and grounding and reheating for 24 h under a flow of oxygen. In prior to the synthesis, Nb_2O_5 is first converted to its high temperature stable monoclinic form by heating at 1100 ºC for 4 days. It is then reacted with CuO at 700 ºC for 48 h. Excess CuO is removed by washing with HCl and water and the product is then finally heated at 500 ºC for 24 h under oxygen atmosphere. Pullar *et al.* (2005) have described a procedure for the synthesis of $CuNb_2O_6$ in which CuO and Nb_2O_5 are mixed through ball milling in presence of deionized water for 2 days. Then the mixture is dried on a rotary evaporator and heated at 900 ºC. The final product is reported to be a mixture of mostly monoclinic with a small amount of orthorhombic phase.

This conventional solid-state synthesis method often results in chemically inhomogeneous product with coarse particle size.

2.2.2 Chemical Method

Chemical methods are known to be convenient for the synthesis of chemically homogeneous, nanocrystalline powders; however, only few literature reports are available for the preparation of $CuNb_2O_6$ powders through the chemical method. The wet chemical methods which are available for the synthesis of $CuNb_2O_6$ are as follows:

Langbein *et al.* (1995) have reported the preparation of $CuNb_2O_6$ powders using freeze-dried complex oxalate precursors of copper and niobium, mixed together with Cu: Nb mole ratio of 1:2. The thermal decomposition of the amorphous oxalate precursor at 600 °C for 3 h leads to the formation of $CuNb_2O_6$.

From literature survey, it is clear that reports on the chemical methods for the preparation of $CuNb_2O_6$ powders are limited. The major hindrance in the use of chemical methods for their preparation is the scarcity of appropriate niobium source. The use of commonly available niobium sources such as, niobium alkoxides and $NbCl_5$ gets complicated by their moisture sensitivity and easy hydrolysis during the reaction process. Therefore, the preparation of $CuNb_2O_6$ through chemical method necessitates development of a suitable niobium source that would be stable in aqueous medium in course of the reaction process. In the present investigation, an aqueous based chemical synthesis process has been developed for the preparation of nanocrystalline $CuNb_2O_6$ powders based on simple metalo-organic complex chemistry where niobium tartrate has been used as the niobium source. The use of niobium tartrate circumvents the problems of moisture sensitivity since the coordinate complex is soluble in water and does not undergo hydrolysis on storage or, during the reaction process (Das *et al.*, 2000a; 2000b).

2.3 Scope of the Present Investigation

The present study describes the aqueous based chemical synthesis of nanocrystalline powders of $CuNb_2O_6$ through a metal ion-ligand complex based precursor route, using

water soluble niobium tartrate as the source of the nobium ion. In the developed process, the aqueous based metal ion-ligand complex precursor solution is obtained by mixing aqueous solution of copper nitrate and niobium tartrate with triethanolamine (TEA) in the required amounts. The precursor solution is then pyrolyzed to voluminous carbonaceous mass through oxidative decomposition of the metalo-organic complexes. This solid precursor is calcined at 700 °C for 2 h to obtain the nanocrystalline powders of $CuNb_2O_6$.

In the present study, the sensing characteristics of the prepared nanocrystalline $CuNb_2O_6$ composition towards different reducing gases (such as, H_2, liquefied petroleum gas (LPG), and NH_3) have also been investigated. The response of a sensor material towards test gases is intimately related to their grain size, surface morphology, and internal porosity. The nanocrystalline sensor materials are thus expected to exhibit increased sensitivity towards the test gases compared to their bulk counter parts due to high specific surface area and reduced size of their grains.

2.4 Synthesis of Nanocrystalline $CuNb_2O_6$ Powders

2.4.1 The Raw Materials Used in the Developed Synthesis Method

i) Copper nitrate, ii) Niobium pentoxide, iii) Triethanolamine (TEA), iv) Tartaric acid, vi) Ammonia (25%), vii) Hydrofluoric acid (40%), viii) Ammonium oxalate, and ix) Nitric acid (70%). All the materials were procured from M/S Aldrich (U.S.A).

In this study, aqueous solution of niobium tartrate was prepared in the laboratory and stocked for use as a source of niobium in the process.

2.4.1.1 Preparation of Aqueous Solution of Niobium Tartrate

Aqueous solution of niobium tartrate was prepared starting from its hydrous oxide [$Nb_2O_5.nH_2O$]. To begin with, niobium oxide (Nb_2O_5) was dissolved in hydrofluoric acid (>7 M) by heating the mixture over a water bath for 28-30 h to obtain a clear

solution of the niobium-fluoride complex (i.e., $NbOF_5^{2-}$ or NbF_7^{2-}). Freshly prepared aqueous solution of ammonium oxalate (>4 M) was then added to this clear solution of niobium-fluoride complex. Hydrous niobium oxide ($Nb_2O_5.nH_2O$) was then precipitated out from this clear solution of niobium-fluoride complex by drop wise addition of diluted ammonia (ammonia to water ratio was maintained as 1:1). The precipitate was finally washed with 5% ammonia to make it free from fluoride ions. This hydrous oxide was then slowly dissolved in an aqueous solution of tartaric acid (two moles per mole of the niobium ion) with constant stirring to obtain the aqueous solution of niobium tartrate. The niobium content in the solution was estimated by the gravimetric assay. The schematic representation of the preparative method of aqueous solution of niobium tartrate is shown in Figure 2.1.

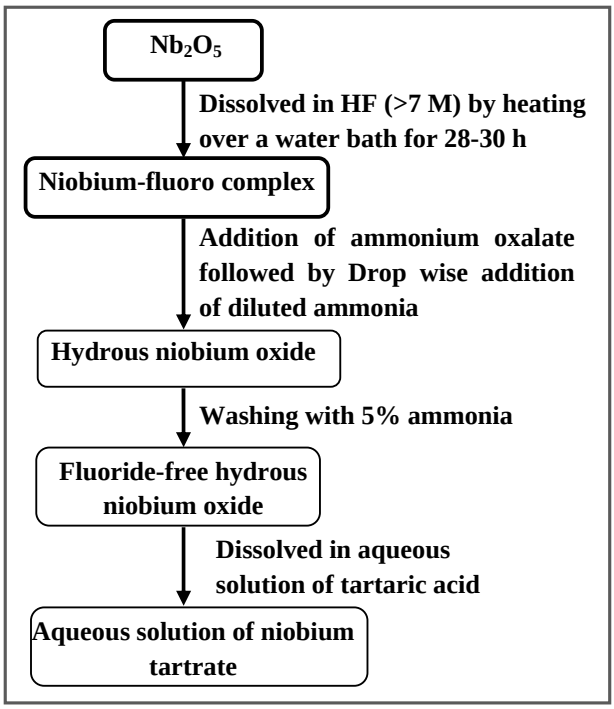

Figure 2.1: *Schematic representation of the preparation of the aqueous solution of niobium tartrate.*

The hydrated oxide precipitates when obtained by adding only diluted ammonia in absence of ammonium oxalate tends to form long polymeric chains of the poly-nuclear hydrous niobium oxides during the precipitation and washing process, which suppresses the dissolution of the precipitate in tartaric acid. Addition of ammonium oxalate into the solution of niobium-fluoro complex before the precipitation helps to truncating the polymeric chains of the poly-nuclear of the hydrous niobium oxide by occupying the coordinating sites of niobium ions during the precipitation process. Therefore, the addition of aqueous solution of ammonium oxalate into the solution of niobium fluoro complex serves to facilitate the dissolution of hydrous niobium oxide precipitates, obtained by diluted ammonia, in tartaric acid.

2.4.2 Synthesis Procedure of Nanocrystalline $CuNb_2O_6$ Powders

100 ml of aqueous solution of copper nitrate (0.1 M) was mixed with 200 ml of aqueous solution of niobium tartrate (0.1 M), maintaining the molar ratio of Cu^{2+}: Nb^{5+} at 1:2 in the solution mixture. TEA (4 moles per mole of cations present in the solution mixture) was then added into the solution mixture under constant stirring. To avoid any undesired precipitation, the final solution mixture was maintained at almost neutral pH by the addition of nitric acid. This solution was then heated at about 200 ºC until complete dehydration occurred and metalo-organic complexes underwent oxidative-decomposition with the evolution of dense fumes to generate a voluminous fluffy carbonaceous mass. The black fluffy mass was then crushed into powders. Calcination of this carbonaceous precursor powders at 700 ºC for 2 h produced carbon-free yellow colored nanocrystalline powders of $CuNb_2O_6$ in the monoclinic phase. The method for the preparation of nanocrystalline $CuNb_2O_6$ powders is schematically depicted in Figure 2.2.

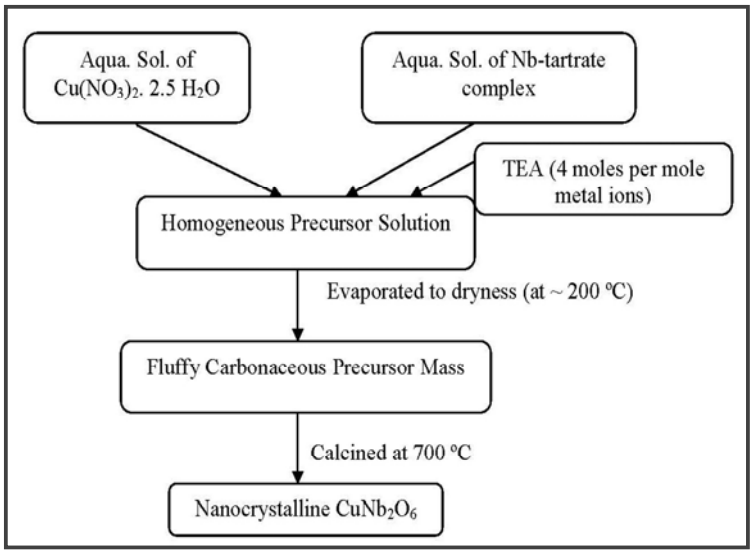

Figure 2.2: *Schematic representation of the preparation of the nanocrystalline $CuNb_2O_6$.*

2.5 Techniques for Characterization of the Prepared Nanocrystalline $CuNb_2O_6$ Powders

Carbonaceous precursor of $CuNb_2O_6$ was characterized with simultaneously recorded thermogravimetric and differential thermal analysis (TG and DTA) in air at a heating rate of 5 °C/min using Perkin Elmer instruments (Pyris Diamond TG/DTA). The $CuNb_2O_6$ powders, calcined at 700 ºC for 2 h, were characterized by X-ray powder diffraction (XRD) using an X'Pert-pro diffractometer operated at 40 kV and 25 mA with Cu$K\alpha$ radiation and a Ni filter. Measurement was performed at room temperature under vacuum to minimize air scatter. The data were collected over the 2θ angle range of $10^o \leq 2\theta \leq 70^o$ with a step size of 0.05º. The step time was 2 s. For phase identification, the obtained XRD pattern was analyzed by comparing with PCPDFWIN (Copyright 1999 JCPDS-ICDD) data file. Rietveld refinement of the observed data was carried out using the X'pert high score plus software package to obtain information on its crystal structure. The crystallite size (D) of the compositions was calculated using Scherrers equation to the full widths at half maximum (FWHM) of the diffraction peaks after introducing the correction for instrumental broadening

with respect to standard silicon. The actual FWHMs were calculated by the following equations considering the peaks to be of the Gaussian type:

$$\left(\beta^{\circ}\right)^2 = \left(\beta^m\right)^2 - \left(\beta^s\right)^2 \qquad \text{and} \qquad D = \frac{0.9\lambda}{\beta^o \cos\theta}$$

where β^o = FWHM considering the particle size effect, β^m = integral of FWHM, β^s = FWHM due to instrumental effect for the standard Si, θ = half incident angle of the X-ray for the chosen diffraction peaks, and λ = wavelength of the target material (λ = 1.5406 Å). The transmission electron microscopy (TEM) studies were carried out with 200 keV electron beams using JEOL 2010 (ultrahigh-resolution model) for studying the morphological details of prepared powders. For the TEM experiment, the samples were prepared by suspending the heat-treated powder in ethyl alcohol by sonication and taking a drop of the suspension on a 200-mesh carbon coated copper grid. The morphology of the synthesized nanocrystalline powders and the morphology of the surface of the pellets, derived from nanocrystalline powders were studied using a JEOL-JSM6500 field-emission scanning electron microscope (FESEM) equipped with an energy dispersive X-ray (EDX) analyzer (Oxford). The BET (Brunauer-Emmett-Teller) specific surface areas of the calcined powders (after out-gassing the powders at 200 ^oC for 4 h) were determined through N_2 adsorption isotherms at 77 K using a Beckman Coulter SA3100 surface area analyzer.

2.6 Results and Discussion

2.6.1 Thermal Studies of the Nanocrystalline $CuNb_2O_6$ Precursors

Thermogravimetric (TG) and differential thermal analysis (DTA) of the carbonaceous precursor powders of $CuNb_2O_6$ were carried out in aerial atmosphere. The TG and DTA curve of the precursor powders for $CuNb_2O_6$ are shown in Figure 2.3. The DTA curve for the carbonaceous precursor mass showed a broad exothermic peak extended from 270 °C to ~530 °C. This is because of oxidation of organic matters present in the carbonaceous precursor generated from the decomposition of the metalo-organic

complexes and TEA. Evolution of large amounts of gases (such as, water vapor, oxides of carbon, oxides of nitrogen etc.) during the oxidation of the carbonaceous matter was manifested by a single step weight loss in the TG curve (around 60%). No further weight loss after ~530 °C ensured complete removal of carbon residue from the powders calcined above this temperature.

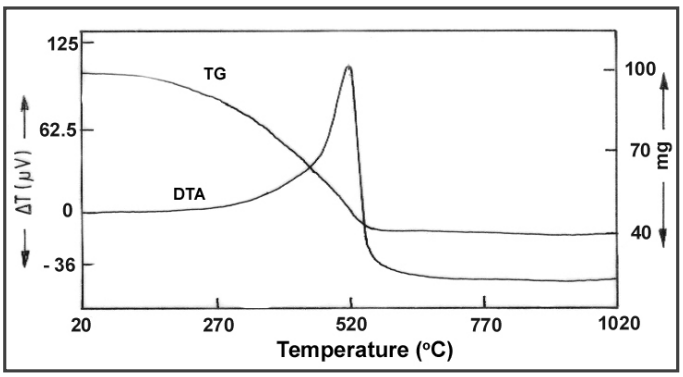

Figure 2.3: *Simultaneously recorded TGA/DTA plots of the carbonaceous precursors of $CuNb_2O_6$.*

2.6.2 Composition, Phase and Structural Analysis of the Nanocrystalline $CuNb_2O_6$ Powders

Phase analysis and structural characterization of the prepared $CuNb_2O_6$ powders were carried out through room temperature X-ray powder diffraction (XRD) studies. Figure 2.4a shows the XRD pattern of the $CuNb_2O_6$ powders obtained on calcination of the carbonaceous precursor at 700 ºC for 2 h. The diffraction lines in the XRD of these greenish yellow powders confirmed the monoclinic phase of $CuNb_2O_6$ as per the standard data in JCPDS file (card no. 830-369). This observation is in agreement with the available literature, which states that the monoclinic phase is the predominant and stable polymorph of $CuNb_2O_6$ at temperature between 700 ºC and 900 ºC. Rietveld refinements of the X-ray data (figure 2.4b) were carried out for detail characterization of the monoclinic phase of $CuNb_2O_6$. The lattice parameters obtained through Rietveld refinement of the X-ray data [a = 5.002(1) Å, b = 14.157(4) Å, c = 5.752(1) Å, and β = 91.52 (1)] matched closely with the standard lattice parameter values

reported in the JCPDS file. Few other data on the monoclinic phase of $CuNb_2O_6$ have been summarized in Appendix A. The average crystallite size of $CuNb_2O_6$ (obtained on calcination of precursors at 700 ºC for 2 h) was calculated using Scherrers equation and the value was found to be 25 nm.

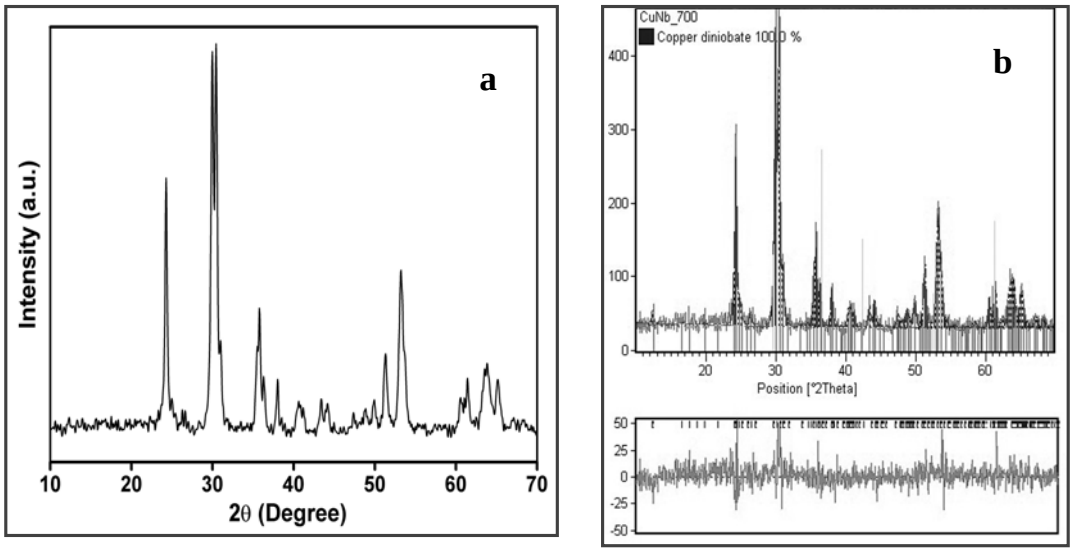

Figure 2.4: ***(a)*** *X-Ray diffractogram (using CuK_α radiation) of the $CuNb_2O_6$ precursors after calcination at 700 ºC for 2 h.* ***(b)*** *Rietveld refinement of monoclinic $CuNb_2O_6$ calcined at 700 ºC for 2 h. Vertical bars show the positions of Bragg reflections.*

The chemical composition of the calcined powders at 700 °C was analyzed using Energy dispersive X-ray spectroscopy (EDX). Spot EDX analysis (Figure 2.5) at various locations on the micrograph confirmed the homogeneous composition of powders and the expected chemical composition of $CuNb_2O_6$ with the observed stoichiometric ratio of Cu: Nb in the compound of 1:2.

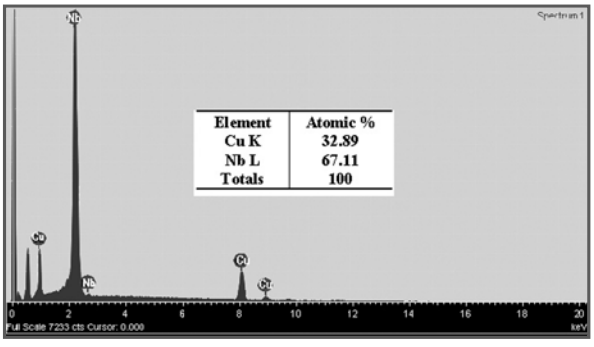

Figure 2.5: *EDX analysis of the $CuNb_2O_6$ after calcination at 700 ºC for 2 h.*

2.6.3 Morphology and Microstructural Studies of the Nanocrystalline $CuNb_2O_6$ Powders

The microstructural information of the calcined powders of $CuNb_2O_6$ was obtained through transmission electron microscopy (TEM) studies. Figure 2.6a shows the bright field electron micrograph of synthesized $CuNb_2O_6$. The smallest particles visible in the micrograph can be identified as single crystallites and/or their aggregates with particle size in the range of 20-38 nm. The characteristic selected-area electron diffraction (SAED) pattern of the powders (Figure 2.6b) showed distinct rings corresponding to the (011), (031), $(\bar{1}31)$ and (200) planes in a monoclinic lattice of $CuNb_2O_6$. The ring pattern also indicated the powders to be polycrystalline in nature.

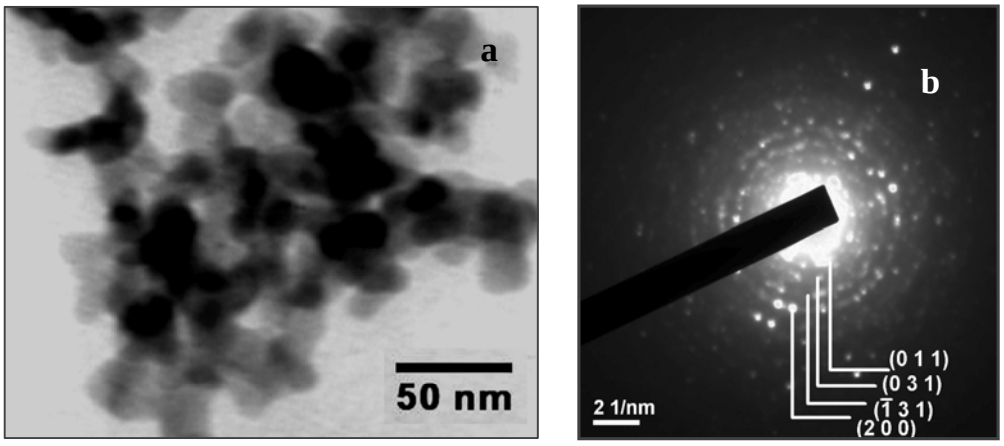

Figure 2.6: ***(a)*** *Bright field TEM micrograph of the calcined (at 700 ºC for 2h) $CuNb_2O_6$.* ***(b)*** *SAED pattern of the calcined (at 700ºC for 2h) $CuNb_2O_6$.*

Field-emission scanning electron microscopy (FESEM) studies were carried out using both, the calcined powders of $CuNb_2O_6$ and porous pellet of the calcined $CuNb_2O_6$ powders. FESEM micrograph, depicting the particle morphology of the calcined $CuNb_2O_6$ powders, is shown in Figure 2.7. The micrograph revealed that powders were composed of particles with distinct grain boundaries and they were uniformly distributed with the size in the range of 20-40 nm.

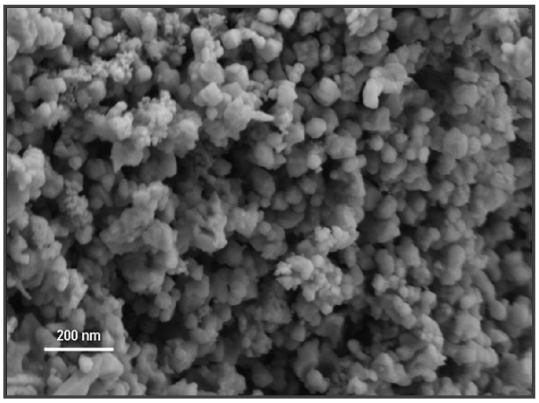

Figure 2.7: *FESEM image of nanocrystalline $CuNb_2O_6$ powders.*

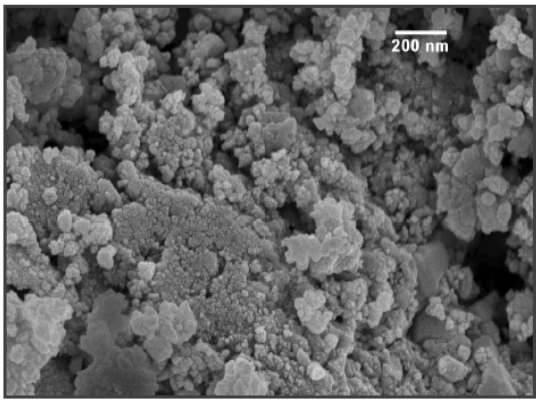

Figure 2.8: *FESEM image of pellet surface derived from nanosized $CuNb_2O_6$ powders.*

FESEM micrograph of the pellets of calcined $CuNb_2O_6$ powders (shown in Figure 2.8) provided information of the microstructure and topology of the pellet surface. The micrograph clearly showed the presence of large porous aggregates composed of smaller individual particles on the surface of the pellets which were obtained by compressing the nanocrystalline powders of $CuNb_2O_6$. Porous morphology of the pellet surfaces is desirable for gas sensor applications since it offers higher surface area for adsorption of the test gases onto the pellet surface. The figure 2.8 shows large number of individual particles or weakly bound agglomerates with the particle sizes in the nanometer range, lying atop one another thereby creating the porous surface. Flattening of the agglomerated structures in some portion of the micrograph may be attributed to the flattening of the surface due to the compression of the powder on pelletization.

The interaction of porous and compact surfaces of the sensor materials with surrounding gases is quite different (Figure 2.9). In compact surfaces, the interaction with gases takes place only at their geometric surfaces whereas in porous surfaces, the whole volume of the surface layer is accessible to the gases. The gas-active surface in porous layers is therefore much larger than that of compact layers. The gas sensor behavior being a kind of surface catalyzed reaction would be expected to improve

with high gas-active surfaces and thus for the porous layers. Porous and compact surfaces also differ in the way how gas-induced changes in the gas-active surfaces get transduced in a sensor output signal such as, sensor resistance. The conduction mechanism of the sensors in porous and compact surfaces has been shown schematically in the Figure 2.9. For compact layers, the current can be considered to flow through two parallel resistances, one being equivalent to the electron depleted geometric surface which is affected by reactions between analyte gas and chemisorbed oxide species, and the other corresponds to the gas-unaffected bulk. In case of porous layers the situation is different, since each grain possesses an electron depleted surface and current has to pass through the intergranular contacts, thus, the resistances of gas-unaffected bulk and electron depleted surface in series.

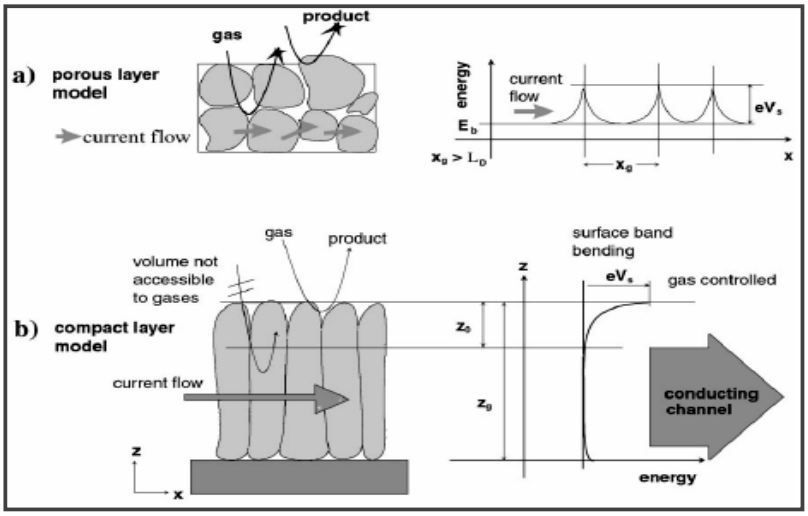

Figure 2.9: *Schematic representation of (a) porous and (b) compact sensing layer with geometry and energy band. x_g grain size, L_D Debye length, eV_s band bending, z_o thickness of the depleted surface layer and z_g layer thickness. Reproduced after* Simon *et al.,* 2001.

The BET surface area of the calcined powders of $CuNb_2O_6$ was found to be 55 m^2g^{-1}. Gas sensing phenomenon being a kind of the surface catalyzed reaction, samples with higher surface area are anticipated to enhance the rate of the reaction and hence the sensing behavior.

2.6.4 Electrical Measurements and Gas Sensing Studies of the Nanocrystalline $CuNb_2O_6$ System

Electrical resistances as well as gas sensing properties of the synthesized material were studied by two probes *dc* conductivity measurements. For the experiment, the nanocrystalline powders were compressed into pellets under pressing in presence of 1 or, 2 drops of poly vinyl alcohol (PVA) (2%). The pellets were then heat-treated at 450 ºC for 4 h to remove any residual polymer making the pellet surface porous solid. Electrical resistances and gas sensing properties of compressed pellets were measured using an experimental setup which was designed, fabricated and standardized for the present study (in house). The photograph of the experimental setup is displayed in Figure 2.10. The diagram of the setup is also presented in Figure 2.11.

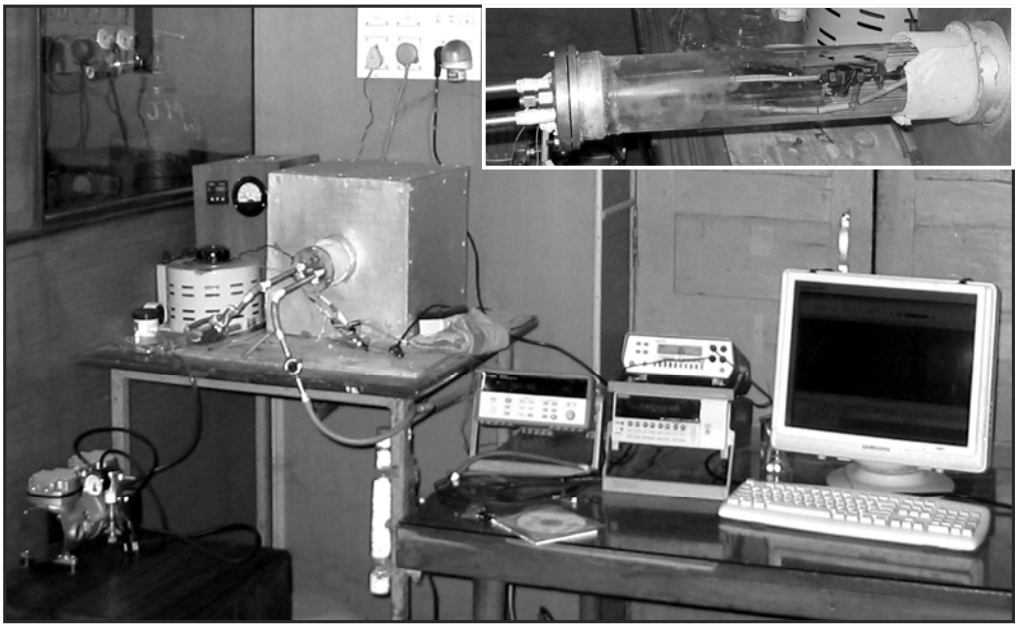

Figure 2.10: *Photograph of the setup equipment for resistance measurements and the cylindrical test-chamber with steel made sample holder (Inset).*

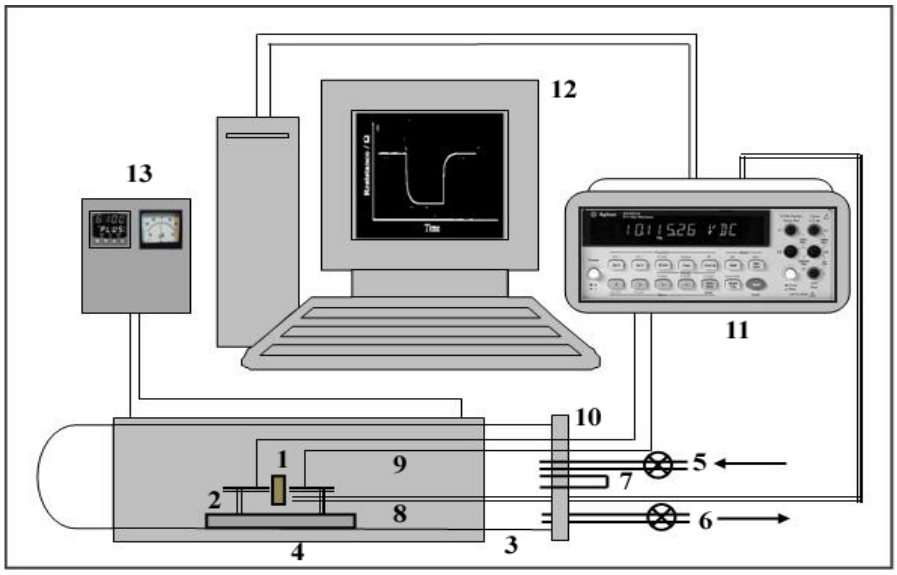

Figure 2.11: *Setup equipment for in-situ resistance measurements: 1) Pellet sample; 2) Two probe sample holder; 3) Quartz test chamber; 4) Furnace; 5) Gas inlet; 6) Gas outlet; 7) Gas injection port; 8) Thermocouple; 9) Platinum wires; 10) Flung; 11) Digital multimeter; 12) Personal computer; 13) Temperature controller (PID controller).*

For carrying out the electrical and gas sensing measurements, the porous pellet with two thin platinum electrodes was housed inside a cylindrical shaped quartz test-chamber. A stainless steel sample holder was used for holding the pellet sample inside the quartz test-chamber. The cylindrical quartz test-chamber was permanently closed at one end while the other end was closed using a flung system. The flung system had provisions for inserting a thermocouple inside the test chamber (in close proximity of the sample pellet) and an outlet for connecting the two thin platinum electrodes from the sample pellet, placed inside the test chamber, to the multimeter, placed outside of the system. The flung system of the test chamber also had parts for gas inlet, gas outlet and for test gas injection. The entire test-chamber was made leak proof and inserted inside a resistance furnace which used a coil of nichrome wire as the heating element. The furnace was connected to power supply (through a Variac) and the temperature inside the quartz test-chamber was monitored using a PID temperature controller. The sensor operational temperature was measured with a type-K

thermocouple, installed in proximity to the sensor material (i.e. the sample pellet, placed inside the test chamber) while the furnace temperature was monitored using a separate independent thermocouple that was located close to the heating elements of the furnace. The thermocouple located inside the furnace supplied the feedback signal to the PID controller. Application of two thermocouples helped to obtain an accurate sensor operational temperature inside the test chamber without any significant temperature fluctuation. The sensor response was measured up to the maximum temperature of 400 ºC, the typical working temperature range of a gas sensor. The resistance behavior of the heating elements was monitored and stabilized by heating from room temperature up to 400 ºC, at a heating rate of 1 ºC/min.

The resistance of the sensor was measured by two probe *dc* conductivity measurements using the data acquisition units such as, autoranging microvolt DMM (Model 197A, M/s Keithley Instruments, USA) for low temperatures (when the resistance is higher than 100 MΩ) and Agilent Data Acquisition/Switch Unit (model no. 34970A) with a multichannel data input facility for higher temperatures. The sensor operational temperature inside the test-chamber was recorded using the same Agilent Data Acquisition/Switch Unit (model no. 34970A) via a type-K thermocouple. The data were collected in a time interval of 5 s. Agilent Data Acquisition/Switch Unit was connected to a computer via interface (RS-232 connector). All scanned data/readings stored in memory of Data Acquisition/Switch Unit were displayed on a computer monitor through graphs/script charts. At each sensor operating temperature, the test gas was injected into the chamber through the gas injection port after a steady base line resistance in air was established. The corresponding change of electrical resistance of the material was measured as a function of time till a constant resistance value was achieved. Next, the chamber was purged with dry air for 4-5 min and the changes in the electrical resistance was measured only after a steady base line value of resistance was attained. The response of the material to the test gases was calculated using the following equation:

$$\text{Response (\%)} = \left[\frac{R_a - R_g}{R_a} \right] \times 100$$

In the above equation, R_a denotes the resistance in air and R_g the resistance in the presence of a test gas. The response of the material was examined towards H_2, liquefied petroleum gas (LPG), and NH_3 in the temperature range of 200-400 ºC. There were three tests made for each gas at each operating temperature to confirm the results. The reproducibility of the experiments was checked by repeating the same experiment with two more pellets of the composition. Prior to carrying out the sensor experiments, the sample pellets were thermally conditioned by annealing in dry air at 300 ºC, to remove any adsorbed water and to allow the samples to equilibrate with oxygen under the flow of air. The response value, response time and recovery time of the sensors were determined from the decrease of resistance in presence of a reducing gas (i.e. response process) and the regain of the initial value of resistance in air (recovery process) through air purging in the test-chamber with change of time. Response time is defined as the time required for achieving 90% of final change in conductance after the test gas is injected and recovery time is taken as the time needed for the sensor to attain a conductance 10% above the original value in air.

2.6.4.1 Electrical Measurements of the Nanocrystalline $CuNb_2O_6$ System

Electrical conduction in metal oxides is a thermally activated process. The variation of electrical conductivity of $CuNb_2O_6$ pellets was studied as a function of temperature, in the range of 200-400 °C. Figure 2.12 shows temperature dependence of the *dc* electrical conductivity of the pellet of $CuNb_2O_6$ in the temperature range of 200–400 °C. The *dc* electrical conductivity (σ) followed the Arrhenius law,

$$\sigma = \sigma_o e^{\frac{E_a}{KT}}$$

where σ_o is a pre-exponential factor and E_a, k, and T are, respectively, the activation energy for conduction, Boltzmann's constant, and absolute temperature. From the Arrhenius plot (Figure 2.12) it could be seen that the logarithm of conductivities (Ln σ) of the sample had a linear relationship with reciprocal of temperature (1/T), as is expected for a typical semiconducting material, with no hysteresis during heating and

cooling cycles. The activation energy (E_a), determined from the slope of the Arrhenius plot, was found to be 0.55 eV (correlation factor of the linear least-squares fit R > 0.9996). Conductivity in the sample at lower temperature region arose due to changes in the surface conduction (Chambon *et al.*, 1995). The sample showed typical *n*-type conductivity behavior, which was indicated by decrease in the electrical resistance in presence of reducing gases and increase when exposed to O_2.

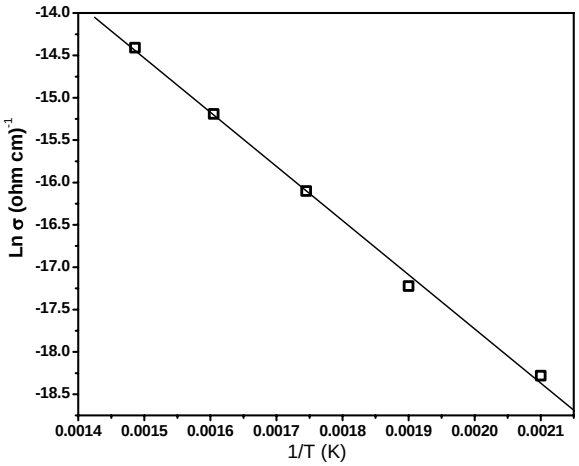

Figure 2.12: *Arrhenius plot for electrical conductivity of $CuNb_2O_6$ in air.*

2.6.4.2 Gas Sensing Studies of the Nanocrystalline $CuNb_2O_6$ System

Figures 2.13-16 show the typical temperature dependence of response of compressed powder of $CuNb_2O_6$ towards 500 ppm of H_2, LPG, and NH_3 respectively. For 500 ppm H_2, the response was around 68% at 200 ºC. It increased to 73% at 250 ºC. The maximum response of 84% was observed at 300 ºC. The response was found to decrease to 74% at 350 ºC and then to 68% at 400 ºC. For 500 ppm LPG, responses observed at 200 ºC and 250 ºC were 65 and 74%, respectively. For LPG, the maximum response was found to be around 80% at 300 ºC. The response (to LPG) was observed to decrease to 71% at 350 ºC and then to 66% at 400 ºC. Responses towards 500 ppm NH_3 observed at 200 ºC, 250 ºC, 300 ºC, 350 ºC and 400 ºC were 10%, 15%, 26%, 48%, and 56%, respectively. Due to high responses of the sample

pellets towards H_2 and LPG at 300 ºC, this temperature was selected for calibration experiments at different concentrations of test gases.

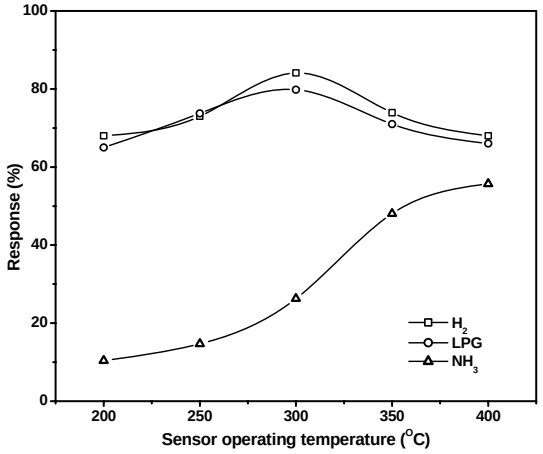

Figure 2.13: *Sensing characteristics of porous pellets of nanocrystalline $CuNb_2O_6$ towards 500 ppm each of H_2, LPG, and NH_3 in air as a function of temperature.*

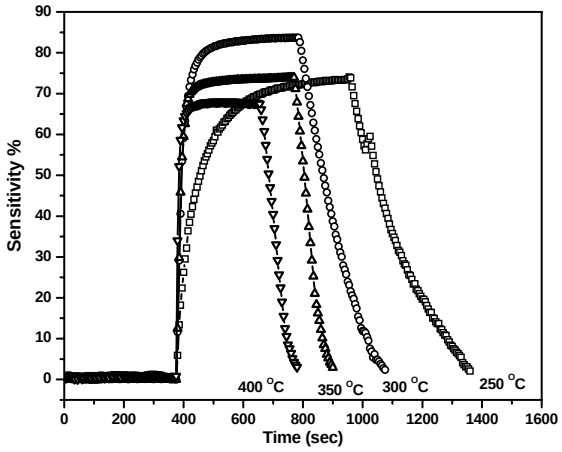

Figure 2.14: *Responses of porous pellets of nanocrystalline $CuNb_2O_6$ towards 500 ppm of H_2 in air at different temperatures.*

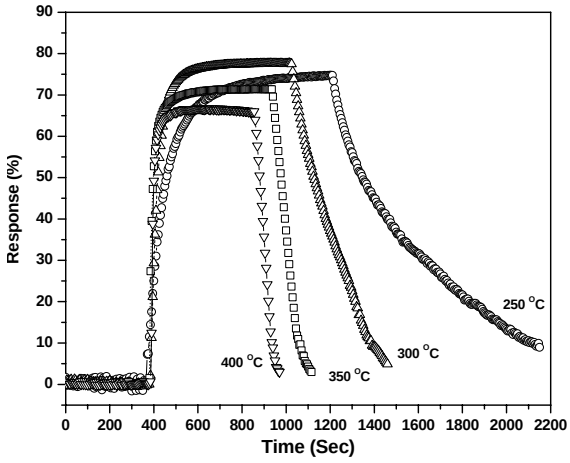

Figure 2.15: *Responses of porous pellets of nanocrystalline $CuNb_2O_6$ towards 500 ppm of LPG in air at different temperatures.*

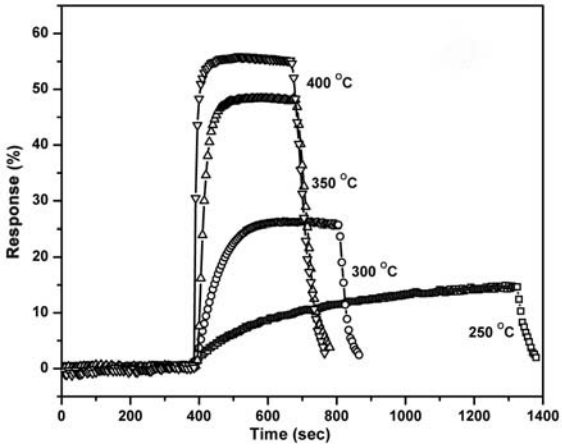

Figure 2.16: *Responses of porous pellets of nanocrystalline $CuNb_2O_6$ towards 500 ppm of NH_3 in air at different temperatures.*

There were three tests were made for each gas at each operating temperature to confirm the results. Figures 2.17 represents three cycles of response-recovery characteristics of the material exposed to 500 ppm H_2, LPG at 300 ºC and NH_3 at 400 ºC.

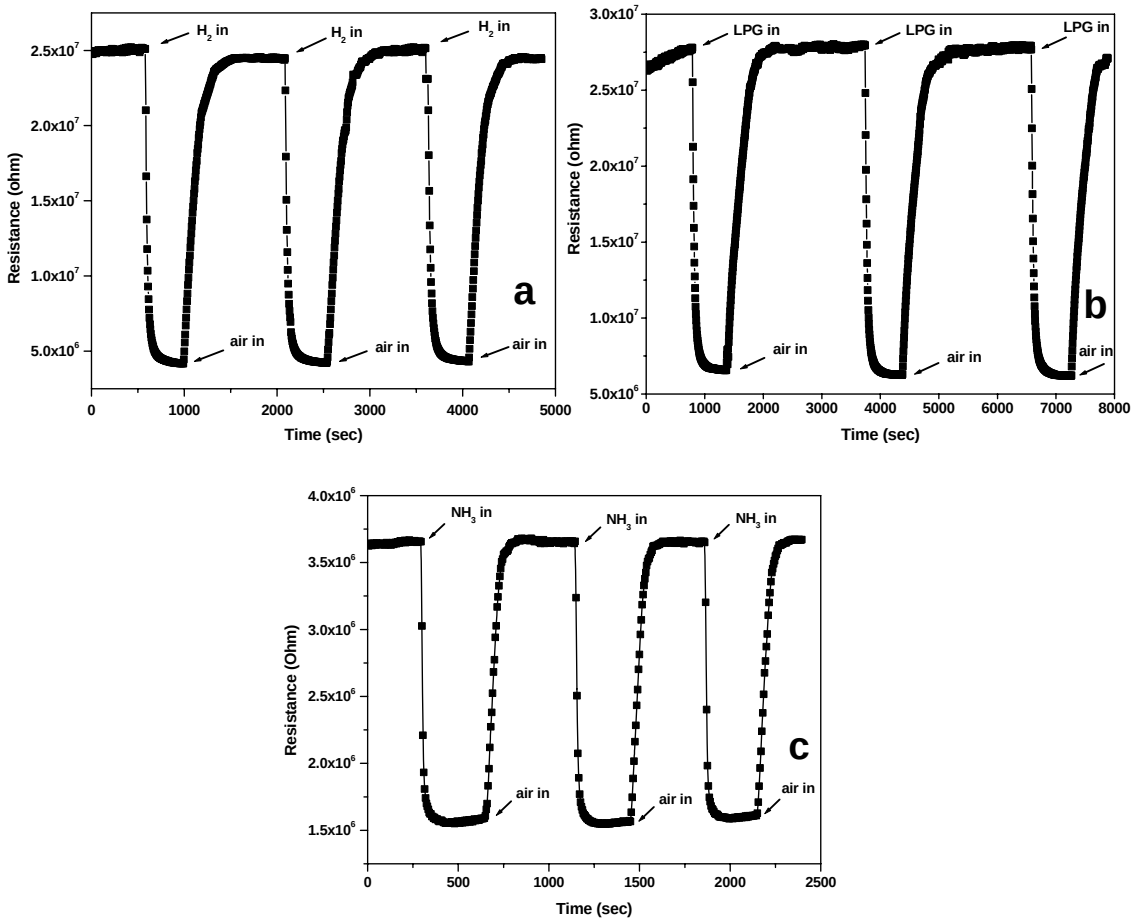

Figure 2.17: *Electrical resistance of porous pellets of $CuNb_2O_6$ in alternating environments of air and* ***(a)*** *500 ppm H_2* ***(b)*** *500 ppm LPG at 300 ºC and* ***(c)*** *500 ppm NH_3 at 400 ºC.*

Figure 2.18 shows the response of the sample pellets of $CuNb_2O_6$ towards different concentrations (100, 300 and 500 ppm) of H_2 and LPG at 300 ºC. The responses to both the gases were found to increase almost linearly with concentration. Typical response and recovery characteristics of the sample pellets (operating at different temperatures towards) towards 500 ppm of the gases are shown in Figure

2.19. The response and recovery time (at the temperature when maximum response was achieved) for the sample pellets of $CuNb_2O_6$ towards H_2 were observed to be around 100 s and 270 s respectively (at 300 ºC), and towards LPG, the responses and recovery times were 144 s and 430 s respectively (at 300 ºC) while towards NH_3, the respective values were 46 s and 95 s (at 400 ºC).

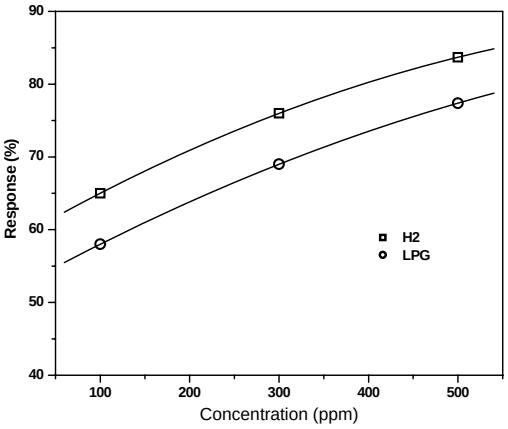

Figure 2.18: *Variation of response of porous pellet of $CuNb_2O_6$ with concentration of H_2 and LPG at 300 ºC.*

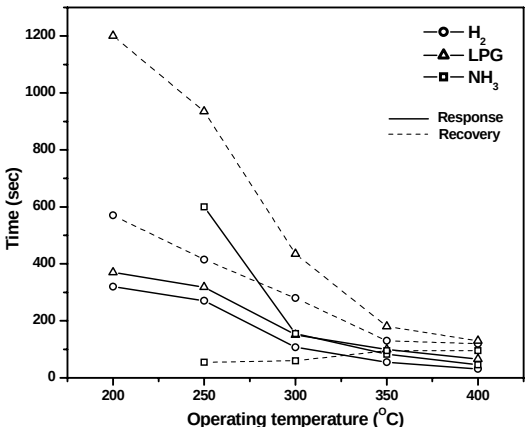

Figure 2.19: *Temperature variation of response time and recovery time for $CuNb_2O_6$ for 500 ppm H_2, LPG and NH_3.*

The response was found to decrease at higher operating temperatures as can be seen in figure 2.12. This behavior can be explained by considering the temperature dependence of the surface coverage of chemisorbed species. Chemisorptions of the gas molecules on the sensor surface takes place at high temperature while physisorption process is predominant only at low temperature and decreases with rise in temperature. At high temperature region, the surface coverage by chemisorbed species decreases with increasing temperature, because at high temperature region, the desorption rate is greater than the adsorption rate. This competition between the rates of adsorption and that of desorption at different temperatures can be shown through the Lennard–Jones equation which is stated below (Madou *et al.*, 1989).

$$\frac{d\theta}{dt} = k_{ads} e^{\frac{-\Delta E_A}{kT}} - k_{des} e^{\frac{-\Delta E_A + \Delta H_{chem}}{kT}}$$

where θ is the fraction of available surface sites covered, k_{ads} and k_{des} are respectively the rate constants for adsorption and desorption reactions, ΔE_A the activate energy of chemisorptions and ΔH_{chem} the heat of chemisorption. In our case, chemisorption was the dominant process in the operating temperature range 200 to 400 ºC and the maximum of sensitivity under the reducing gases at any concentration was generally observed at around 300 ºC. At this temperature the rate of desorption can be considered as negligible and the rate of adsorption predominates. Beyond 300 ºC when the temperature rises, the surface coverage can be considered to decrease, so that the sensitivity decreases also.

Additionally, the physical properties of the semiconducting sensor material such as, charge carrier concentration, the Debye length are influenced by temperature. At higher temperature, the charge carrier concentration increases and the Debye length for an *n*-type semiconductor decreases. This may also be one of the possible reasons for the decrease in the response at higher temperatures (Mizsei, 1995; Wagh *et al.*, 2007). Therefore, it can be interpreted that at high temperatures, as the Debye length decreases the grains become incompletely depleted (Kiss *et al.*, 2001) and as a consequence, the response decreases (Schierbaum *et al.*, 1991; Xu *et al.*, 1999). The decrease of response with shrinking the Debye length at high temperatures can be comprehended from the following two relations (Cosandey *et al.*, 2000):

$$L_D = \left(\frac{\varepsilon_o KT}{n_o e^2} \right)^{\frac{1}{2}} \qquad \text{and} \qquad S = \frac{\Delta n}{n_o} L_D$$

where ε_o is the static dielectric constant, n_o is the total carrier concentration, e is the carrier charge, K is the Boltzmann constant, T is the absolute temperature, S is the response, Δn is the change in the carrier concentration.

The gas sensing phenomenon involves the change of electrical resistance of the sensor material in the presence of gases due to the oxidation of the reducing gases by the surface chemisorbed oxygen species (like O^-, O^{2-}, O_2^-, etc.), which releases the electrons and thus increases the charge in the conduction band of the *n*-type oxide and

hence the conductivity gets increased (i.e. decrease of the potential barrier). The response characteristics to different reducing gases are guided by the trend of reactivity towards the surface chemisorbed oxygen ions. The extent of adsorbed oxygen ions and existence of their different chemical forms (O^-, O^{2-}, O_2^-, etc.) on the sensor surface are controlled by the sensor operating temperature.

$$O_2(g) + e^- \rightarrow O^-_{2\,(ads)}$$

$$O^-_{2\,(ads)} + e^- \rightarrow 2O^-_{(ads)}$$

The oxidation reactions of H_2 and LPG could be represented as follows (Meixner *et al*., 1995):

$$C_pH_{2p+2} + (3p+1)O^-_{(ads)} \rightarrow pCO_2 + (p+1)H_2O(g) + (3p+1)e^-$$

(LPG is a mixture of hydrocarbons like *n*-propane and *n*-butane, so *p = 3 or 4*. This equation is valid for H_2 when *p = 0*).

The oxidation reactions of NH_3 could be represented as follows (Rout *et al*., 2007):

$$2NH_3 + 3O^-_{(ads)} \rightarrow N_2 + 3H_2O + 3e^-$$

2.7 Major Findings in the present Investigation

- Nanocrystalline $CuNb_2O_6$ powders have been synthesized by aqueous based metal ion-ligand complex based precursor route.
- The preparative method established the use of niobium tartrate which is a stable water-soluble source of niobium.
- The orthorhombic phase of $CuNb_2O_6$ formed only at 700 ºC. The low processing temperature involved in this method prevented grain growth in the powders.

- The crystallite sizes, average particle sizes and specific surface areas determined from XRD, TEM and BET surface area measurement were found to be 25 nm, 25-40 nm and 55 m^2g^{-1} respectively.
- Nanocrystalline $CuNb_2O_6$ was *n*-type semiconductor.
- In present study, nanocrystalline $CuNb_2O_6$ in the temperatures range of 200-400 ºC showed the sensitivities to H_2, LPG and NH_3. Sensitivity of $CuNb_2O_6$ has not been documented in the previous reports.
- The maximum responses towards H_2 and LPG are found to be around 84%, and 80% respectively, at 300 ºC, while a response 56% is observed to NH_3 at 400 ºC.

References

Chambon, L., Maleysson, C., Pauly, A., Germain, J. P., Demarne, V. and Grise, A. (1997), Investigation, for NH_3 Gas Sensing Applications, of the Nb_2O_5 Semiconducting Oxide in the Presence of Interferent Species such as Oxygen and Humidity, Sensors and Actuators B: Chemicals, Vol. 45, pp. 107–114.

Cosandey, F., Skandam, G. and Singhal, A. (2000), Materials and Processing Issues in Nanostructured Semiconductor Gas Sensors, JOM-e, Vol. 52, pp.10.

[http://www.tms.org/pubs/journals/JOM/0010/Cosandey/Cosandey-0010.html]

Cruz, A. M., Alcaraz, N. L., Fuentes, A. F., and Martínez, L. M. T. (1999), Electrochemical Lithium Insertion in Some Niobates MNb_2O_6 (M = Mn, Co, Ni, Cu, Zn and Cd), Journal of Power Sources, Vol. 81-81, pp. 255-258.

Das, R. N., Ray, J. C. and Pramanik P. (2000), Low Temperature Chemical Synthesis of Nanocrystalline $Pb(Mg_{1/3}Nb_{2/3})O_3$ and $(1-x)Pb(Mg_{1/3}Nb_{2/3})O_3$-$xPb(Fe_{1/2}Nb_{1/2})O_3$ (x = 0.1, 0.2, and 1) Ceramics, Journal of Material Research, Vol. 15, No. 11, pp. 2273-2277.

Das, R.N. and Pramanik, P. (2000), Chemical Synthesis of Fine Powder of Lead Magnesium Niobate Using Niobium Tartrate Complex, Materials Letter, Vol. 46, No. 1, pp. 7–14.

Drew, M. G. B., Hobson, R. J., and Padayatchy, V. T., (1993), Synthesis, Single-crystal Structure and Magnetic Properties of Orthorhombic $CuNb_2O_6$, Journal of Materials Chemistry, Vol. 3, No. 8, pp. 889-892.

Drew, M. G. B., Hobson, R. J., and Padayatchy, V. T., (1995), Synthesis, Structure and Magnetic Properties of Monoclinic $CuNb_2O_6$ and the Electronic Spectra of both Polymorphs of $CuNb_2O_6$, Journal of Materials Chemistry, Vol. 5, No. 11, pp. 1779-1783.

Felten, E. J. (1967), The preparation of $CuNb_2O_6$ and $CuTa_2O_6$, Journal of Inorganic and Nuclear Chemistry, Vol. 29, pp. 1168-1171.

Kiss, G., Pintér, Z., Perczel, I. V., Sassi, Z., Réti, F. (2001), Study of Oxide Semiconductor Sensor Materials by Selected Methods, Thin Solid Films, Vol. 391, pp. 216-223.

Kodama, K., Harashina, H., Sasakia, S., Kanada, M., Katoa, M., Satoa, M., Kakurai, K. and Nishi, M. (1999), Magnetic Excitations of $CuNb_2O_6$, Journal of Physics and Chemistry of Solids, Vol. 60, pp. 1129–1132.

Koo, H.-J. and Whangbo, M.-H. (2001), Examination of the Anisotropic Spin Exchange Interactions of CuM_2O_6 (M = Sb, V, Nb) by Spin Dimer Analysis, Journal of Solid State Chemistry, Vol. 156, pp. 110-116.

Langbein, H. and Wölki, G. (1995), Preparation of Copper Niobates by Thermal Decomposition of Freeze-Dried Complex Oxalate Solutions, Thermochimica Acta, Vol. 264, pp. 67-73.

Madou, M. J. and Morrisson, S. R. (1989), Chemical Sensing with Solid State Devices, Solid/Gas Interfaces, Academic Press, Chapter 3, pp. 67–72.

Meixner, H., Gerblinger, J., Lampe, U., Fleischer, M. (1995), Thin-film Gas Sensors Based on Semiconducting Metal Oxides, Sensors and Actuators B: Chemical, Vol. 23, pp. 119-125.

Mizsei, J. (1995), How Can Sensitive and Selective Semiconductor Gas Sensors Be Made? Sensors and Actuators B, Chemical, Vol. 23, pp. 173-176.

PCPDFWIN version 2.02 May 1999 Copyright 1999 JCPDS-ICDD.

Pullar, R. C., Breeze, J. D. and Alford N. M. (2005), Characterization and Microwave Dielectric Properties of $M^{2+}Nb_2O_6$ Ceramics, Journal of the American Ceramic Society. Vol. 88, No. 9, pp. 2466–2471.

Rout, C. S., Hegde, M., Govindaraj, A., Rao, C. N. R. (2007), Ammonia Sensors Based on Metal Oxide Nanostructures, Nanotechnology, Vol. 18, pp. 205504.

Schierbaum, K. D., Weimar, U., Göpel, W. and Kowalkowski, R. (1991), Conductance, Work Function and Catalytic Activity of SnO_2-Based Gas Sensors, Sensors and Actuators B: Chemicals, Vol. 3, pp. 205-214.

Sato, M. and Hama, Y. (1995), Lithium Insertion Characteristics of $CuNb_2O_6$, Journal of Solid State Chemistry, Vol. 118, pp. 193-198.

Wagh, M. S., Jain, G. H., Patil, D. R., Patil, S. A. and Patil, L. A. (2007), Surface Customization of SnO_2 Thick Films Using RuO_2 as A Surfactant for the LPG Response, Sensors and Actuators B: Chemicals, Vo. 122, pp. 357- 364.

Wahlström, E., and Marinder, B.-O. (1977), Phase Analysis Studies in the Copper-Niobium-Oxygen System, Inorganic and Nuclear Chemistry Letters, Vol. 13, No. 11, pp. 559-564.

Xu, C., Tamaki, J., Miura, N., Yamazoe, N., (1999), Grain Size Effects on Gas Sensitivity of Porous SnO_2-Based Elements, Sensors and Actuators B: Chemicals, Vol. 3, pp. 147-155.

Chapter 3

Synthesis of Nanocrystalline Powders of $FeNbO_4$ (with and without Pt Impregnation) and Studies on their Gas Sensing Behavior towards Ammonia, Hydrogen, and Liquefied Petroleum Gas

Chapter 3

Synthesis of Nanocrystalline Powders of $FeNbO_4$ (with and without Pt Impregnation) and Studies on their Gas Sensing Behavior towards Ammonia, Hydrogen, and Liquefied Petroleum Gas

3.1 Introduction

ABO_4 type oxides containing transition metal ions have significant contribution in many areas of applications such as, in gas sensors, catalysis, and in various semiconductors and photodetector technologies. Iron niobate ($FeNbO_4$), a well known compound of the ABO_4 family has in particular gained considerable attention for the potential applications in gas sensors, catalysis, photodetectors and as magnetic materials (Harrison *et al.*, 1989; Koenitzer *et al.*, 1980; Pourroy *et al.*, 1990a, 1990b; Roth *et al.*, 1964; Schmidbauer *et al.*, 1997; Tena *et al.*, 1996). $FeNbO_4$ exhibits semiconducting (Leiva *et al.*, 1982; Tena *et al.*, 1996) as well as magnetic behavior (Harrison *et al.*, 1989; Noda *et al.*, 1979; Pourroy *et al.*, 1990) consistent with the coexistence of Fe^{2+} and Fe^{3+} ions. Electrical studies reveal that $FeNbO_4$ behaves as an extrinsic semiconductor and its total conduction can be attributed to mixed valence semiconduction (Tena *et al.*, 1996). Additionally, $FeNbO_4$ is being realized as a possible photoanode material for photoelectrochemical application (Koenitzer *et al.*, 1980). $FeNbO_4$ is also an important precursor for the preparation of single-phase perovskite $Pb(Fe_{1/2}Nb_{1/2})O_3$ (PFN), which is an important material for multilayer ceramic capacitor (MLCC) applications. Synthesis of such lead-based complex oxides through the conventional solid-state method often introduces secondary phases, chiefly the pyrochlore phase, which are undesirable and severely degrades the dielectric properties of the final products (Kim *et al.*, 2003; Shrout *et al.*, 1987). The use of $FeNbO_4$ as a precursor has been found to be an effective way of producing PFN powders in the pure perovskite phase.

$FeNbO_4$ comprises of two transition metal ions with similar ionic radii but different valence states and exhibits semiconducting behavior similar to other transition metal oxides. In recent years, $FeNbO_4$ has been investigated for its gas

sensing behavior for the detection of toxic and inflammable gases such as, Cl_2 gas (Dawson, *et al.*, 1996), CO (Henshaw *et al.*, 1996), H_2S, H_2, and liquefied petroleum gas (LPG) (Gnanasekar *et al.*, 1999). In most cases, the sensitivities of $FeNbO_4$ towards trace amount of these gases (in air) have been investigated using compressed powders (Gnanasekar *et al.*, 1999; Henshaw *et al.*, 1996) or a thick film (Dawson, *et al.*, 1996) at various operating temperatures.

3.2 Reported Methods for the Synthesis of $FeNbO_4$

The preparation of $FeNbO_4$ has most commonly been reported through the conventional solid-state method and very limited literature is available on the use of chemical methods for this purpose. Some of the reported methods of the synthesis of $FeNbO_4$ composition are summarized below.

3.2.1 Conventional Solid-State Method for the Synthesis of $FeNbO_4$

The conventional solid-state method is a frequently used process for the preparation of bulk $FeNbO_4$ powders, where stoichiometric amounts of the raw materials (such as: α-Fe_2O_3 and Nb_2O_5) are thoroughly mixed and heated (usually) in air and at temperatures higher than 1000 ºC for a period of about 24 to 48 h to produce the desired phase (Dawson, *et al.*, 1996; Gnanasekar *et al.*, 1999; Henshaw *et al.*, 1996; Koenitzer *et al.*, 1980; Schmidbauer *et al.*, 1997). In 1999, Ananta *et al.* reported a modified solid-state route for the synthesis of $FeNbO_4$ powders using the rapid vibro-milling technique. The reported technique involves mixing, drying, grinding, sieving of the raw materials (such as, Fe_2O_3 and Nb_2O_5) and calcinations at 1150 °C for 4 h followed by further sieving of the product.

The high temperature solid-state method is however disadvantaged by the formation of chemical inhomogeneous final product, a finding, which has been collaborated by investigations carried out by Pourroy *et al.* (1990a). Their studies reveal that the major drawback of the solid-state method in the preparation of $FeNbO_4$

powders arise due to reduction of α-Fe_2O_3 into Fe_3O_4 which leads to an incomplete reaction between the raw materials (i.e. α-Fe_2O_3 and Nb_2O_5) and hence chemically in a chemically inhomogeneous product. Similar observations of chemical homogeneity in the final product have been reported by Koenitzer *et al.* (1980) on heating α-Fe_2O_3 and Nb_2O_5 at 1330 °C for 25 h. They identified a small amount of α-Fe_2O_3 in $FeNbO_4$ which supports the formation of $FeNb_2O_6$ as secondary phases. Roth *et al.* (1964) on the other hand have noticed an increase in the unit cell dimensions of $FeNbO_4$ powders when prepared through a solid-state method by heating the raw materials at increasingly higher temperatures (1085 °C < T < 1380 °C) followed by quenching to room temperatures.

3.2.2 Chemical Method for the Synthesis of $FeNbO_4$

Although the high temperature solid-state method is a simple and inexpensive processing technique for synthesizing $FeNbO_4$, it cannot afford to control the grain size and chemical homogeneity in the final product. The process generally requires high processing temperatures, which result in products that have chemically inhomogeneous and large agglomerated particles with low specific surface area. In contrast, solution based chemical methods are convenient for the synthesis of chemically homogeneous, nanocrystalline powders. In a wet chemical synthesis route better control of homogeneity as well as stoichiometry can be achieved through atomic level mixing of the starting materials in solution and hence can be processed at lower temperatures. Despite the advantages of the solution based chemical methods only few literature reports are available for the preparation of $FeNbO_4$ powders through such processes.

Pourroy *et al.* (1990a) have reported the wet chemical synthesis of $FeNbO_4$ powders through a coprecipitation method using iron oxalate and niobium oxalate as precursors and a large volume of ammonium hydroxide as precipitant. Crystalline powders of $FeNbO_4$ with orthorhombic structure are obtained on heat-treatment of the hydroxide coprecipitates at 800 °C for 72 h.

Tana *et al.* (1996) demonstrated the synthesis of $FeNbO_4$ powders through two types of gel processing such as, the colloidal gel processing and the polymeric gel processing. In the colloidal gel method, gelation takes place when ammonium hydroxide is added into the suspension of $NbCl_5$ and $FeCl_3$, $6H_2O$ in water, with pH of the medium being 5 to 6. Subsequently, the gel is dried with an infrared lamp and heat treated at 1000 °C to obtain $FeNbO_4$ with orthorhombic structure. Conversely, in the polymeric gel method, the gel is obtained by refluxing a solution of $NbCl_5$ in ethanol at 70 °C for 15 h, followed by addition of Fe(III) acetylacetone and again refluxing the solution mixture at 70 °C for 24 h, and acidified with 3M HNO_3. The resulting gel is dried and heat-treated at 1000 °C to obtain $FeNbO_4$ with orthorhombic structure.

Literature survey shows that only few chemical methods exist for the synthesis of powders of $FeNbO_4$. As has been stated in previous chapter (Chapter 2, Section 2.2), the major complication associated with the chemical synthesis of any niobium based oxide systems is the scarcity of appropriate niobium source. The common niobium precursors such as, niobium alkoxides and $NbCl_5$ are not only expensive but are also inhibited by easy hydrolysis due to their moisture susceptibility. In the present investigation, an aqueous based chemical synthesis process has been developed for the preparation of nanocrystalline $FeNbO_4$ powders based on simple metalo-organic complex chemistry where niobium tartrate has been used as the niobium source. The developed synthetic method is less cumbersome, versatile for the preparation of a large variety of multicomponent niobium oxide based systems at relatively low temperatures. The developed method is also proficient in large scale synthesis of nanocrystalline powders of $FeNbO_4$.

3.3 Scope of the Present Investigation

The present study describes the aqueous based chemical synthesis of nanocrystalline powders of $FeNbO_4$ through metal ion-ligand complex based precursor route using water soluble niobium tartrate complex. In the developed process, the aqueous based metal ion-ligand complex precursor solution is obtained by mixing aqueous solution

of iron nitrate and niobium tartrate with triethanolamine (TEA) in the required amounts. The precursor solution is then pyrolyzed to voluminous carbonaceous mass through oxidative decomposition of the metalo-organic complexes. This solid precursor is calcined at 850 °C for 3 h to obtain the nanocrystalline powders of $FeNbO_4$.

In all the gas sensitivity studies reported in literature for $FeNbO_4$, the powders have been prepared through the conventional solid-state method, which produces chemically inhomogeneous composition with large agglomerated particles having low specific surface area. In the present study, the response of the prepared nanocrystalline powders of $FeNbO_4$ has also been investigated towards H_2, liquefied petroleum gas (LPG) and NH_3. Since the response of a sensor towards the analyte gases is intimately related to the grain size, surface morphology, and internal porosity of the sensor material, therefore, the sensor material based on the nanocrystalline powders of $FeNbO_4$ are expected to exhibit increased sensitivity to the test gases compared to that reported so far.

In the present study, a batch of the prepared nanocrystalline powders of $FeNbO_4$ was further impregnated with 1 wt% of platinum and their response towards the mentioned reducing gases were investigated and compared with the non-impregnated sample.

3.4 Synthesis of Nanocrystalline $FeNbO_4$ Powders

3.4.1 The Raw Materials Used in the Developed Synthesis Method

i) Ferric nitrate, ii) Niobium pentoxide, iii) Triethanolamine (TEA), iv) Platinum nitrate, v) Tartaric acid, vi) Ammonia (25%), vii) Hydrofluoric acid (40%), viii) Ammonium oxalate and ix) Nitric acid (70%). All the materials were procured from M/S Aldrich (U.S.A).

In this study, nanocrystalline powders of $FeNbO_4$ were synthesized using niobium tartrate complex solution as a source of niobium which was prepared in the laboratory and stocked for use.

3.4.1.1 Preparation of Aqueous Solution of Niobium Tartrate Complex

In the synthesis of nanocrystalline powders of $FeNbO_4$, the aqueous solution of niobium tartrate complex was prepared following the procedure described in Chapter 2 (Section 2.4.1.11; Figure 2.1).

3.4.2 Procedure for the Synthesis of Nanocrystalline $FeNbO_4$ Powders

100 ml of 0.1 M aqueous solution of iron nitrate was mixed with 100 ml of 0.1 M aqueous solution of niobium tartrate maintaining the equal mole ratio of Fe^{3+}: Nb^{5+} in the solution mixture. TEA (4 moles per mole of cations present in the solution mixture) was then added into the solution mixture under constant stirring. To avoid any undesired precipitation, the pH of the final solution mixture was always maintained at 4 with the help of nitric acid. This solution was then heated at about 200 ºC until complete dehydration occurred and metalo-organic complexes underwent oxidative-decomposition with the evolution of dense fumes to generate a voluminous fluffy carbonaceous mass. The resultant black mass was calcined at various temperatures (ranging between 500-850 ºC) for 3 h to obtain the carbon-free nanocrystalline powders of $FeNbO_4$ in the orthorhombic phase. The method of preparation is schematically depicted in Figure 3.1.

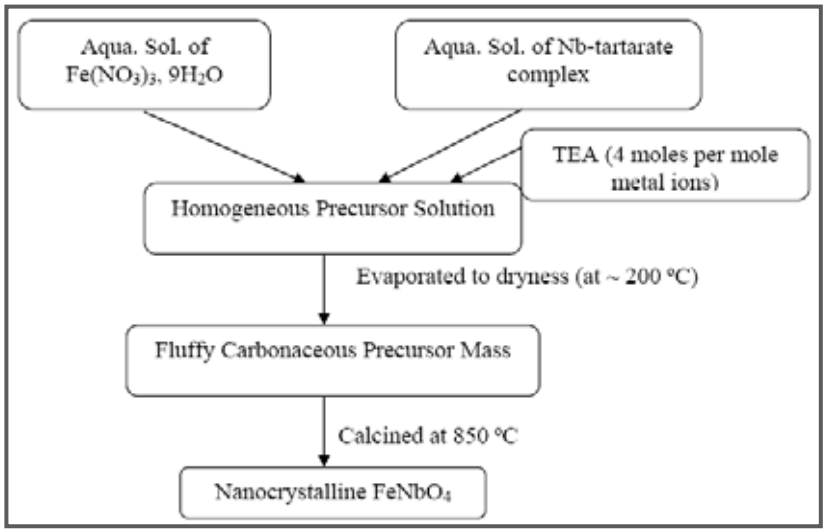

Figure 3.1: *Schematic representation of the preparation of the nanocrystalline powders of $FeNbO_4$.*

3.4.3 Procedure for the Synthesis of Platinum (1 wt%) Incorporated Nanocrystalline $FeNbO_4$ (Pt-$FeNbO_4$) Powders

The nanocrystalline Pt-$FeNbO_4$ powders were synthesized by impregnation method, which involved well mixing of nanocrystalline powders of $FeNbO_4$ with required amount of platinum nitrate solution followed by drying of the powder at 200 ºC and heat-treatment at 850 ºC for 1 h.

3.5 Techniques for Characterization of the Prepared Nanocrystalline $FeNbO_4$ and Pt-$FeNbO_4$ Powders

Thermal studies of the carbonaceous precursor of $FeNbO_4$ were carried out using simultaneously recorded thermo-gravimetric and differential thermal analysis (TG and DTA) in air. The phase identification in both powder samples ($FeNbO_4$ and Pt-$FeNbO_4$) was performed using room temperature X-ray powder diffraction (XRD) with CuK_α radiation and Ni filter. In the XRD studies, the powders obtained at different heat-treatment temperatures were recorded in the 2θ range from 15º to 60º. The average crystallite size of the compositions was calculated using the Scherrers

equation. The microstructural information of the synthesized powders was obtained through transmission electron microscopy (TEM) studies. An energy dispersive x-ray (EDX) analyzer (Oxford) equipped with TEM instrument was used for chemical compositional analysis of the synthesized powders. The specific surface areas of the calcined powders were determined using the BET technique. The instruments, used for the characterization remained same as is mentioned in Chapter 2 (Section 2.5).

3.6 Results and Discussion

3.6.1 Thermal Studies of the Nanocrystalline $FeNbO_4$ Precursors

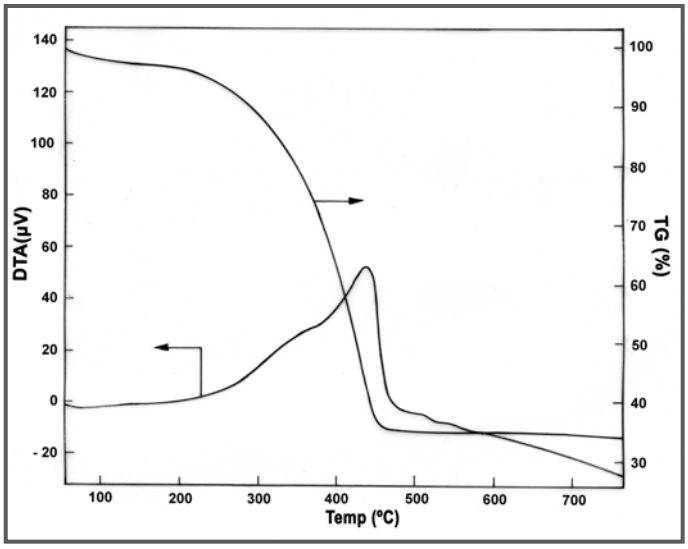

Figure 3.2: *Simultaneously recorded TGA/DTA plots of the carbonaceous precursors of $FeNbO_4$.*

Figure 3.2 shows the simultaneously recorded thermogravimetry (TG) and differential thermal analysis (DTA) plots of the carbonaceous precursor of $FeNbO_4$, produced after complete dehydration of the precursor solution and subsequent decomposition of the metalo-organic complex at around 200 ºC. DTA plot showed a broad exothermic peak extended between 250 °C and 470 °C. This exothermic peak can be attributed to the oxidation of organic substances present in the black carbonaceous precursor. TG

plot showed a sharp and single step weight loss (around 65%) in the corresponding temperature range (i.e., between 250 °C and 470 °C) can be assigned to the evolution of various gases (such as: water vapor, oxides of carbon and nitrogen) during oxidation of the precursor, that was manifested by exothermic thermal effect in the DTA curve. Constant TG curve, observed beyond 470 °C, reflected the constant weight of the sample and ensured complete removal of carbon residue from the powder above 470 °C. The thermal effect associated with the crystallization of the oxide phase was not distinctly visible from the DTA curve, probably due to much higher scale for the oxidative reaction of the organic matter.

3.6.2 Composition, Phase and Structural Analysis of the Nanocrystalline $FeNbO_4$ and Pt-$FeNbO_4$ Powders

Phase analysis and structural characterization of the prepared $FeNbO_4$ powders were carried out through room temperature X-ray powder diffraction (XRD) studies. Figure 3.3a shows the XRD patterns of the carbonaceous precursor of $FeNbO_4$ calcined at different temperatures ranging from 550 ºC to 850 ºC for 3 h. The carbonaceous

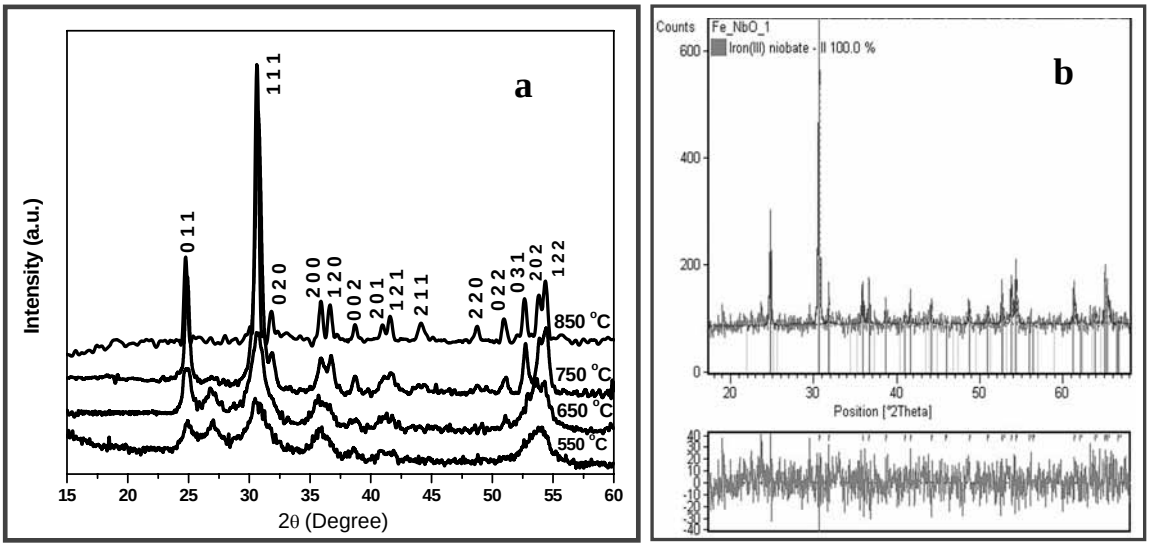

Figure 3.3: ***(a)*** *X-ray diffractograms (using CuK_α radiation) of the $FeNbO_4$ precursor on calcination at various temperatures.* ***(b)*** *Rietveld refinement of orthorhombic $FeNbO_4$ obtained on calcination of the precursor at 850 ºC for 3 h. Vertical bars show the positions of Bragg reflections.*

precursor mass of $FeNbO_4$, when calcined below 550 ºC was amorphous to XRD. The amorphous precursors started to crystallize when calcined at 550 ºC for 3 h. The orthorhombic phase of $FeNbO_4$ was completely realized after calcination of the precursors at 850 ºC for 3 h. Absence of any additional diffraction lines in the XRD of the sample (calcined at 850 ^oC for 3 h), confirmed a pure orthorhombic phase of $FeNbO_4$ as per the standard data reported in JCPDS file (card no. 84-1981) and the diffraction lines were indexed accordingly. The peak at around 2θ = 27º which was present in XRD patterns of the precursors calcined at low temperatures (at 550 and 650 ºC) and disappeared at calcination temperatures higher than 750 ºC could indicate the formation of monoclinic phase (with $AlNbO_4$ crystal structure and C/2m symmetry) of $FeNbO_4$ at temperatures below 750 ºC. Rietveld refinements of the X-ray data (Figure 3.3b) were carried out for detail characterization of the orthorhombic phase of FeNbO4. The lattice parameters obtained through Rietveld refinement of the X-ray data [a = 5.002 Å, b = 5.609 Å and c = 4.635 Å] for the sample matched closely with the standard lattice parameter values. The average crystallite size of $FeNbO_4$, obtained on calcination of the precursors at 850 ºC for 3 h, were calculated using the Scherrers equation and was found to be 20 nm.

It may be noted that for the nanocrystalline powders, prepared through the developed chemical route the orthorhombic phase of $FeNbO_4$ has been realized at low temperature condition and short heat-treatment duration compared to those reported in literature. For example, the existing literature reports state that the monoclinic phase of $FeNbO_4$ can be obtained by heating the raw materials at 1000 ºC for 16 h (Pourroy *et al.,* 1990b), 1000 ºC for 48 h (Gnanasekar *et al.*, 1999), 1000 ºC for 192 h (Schmidbauer *et al.*, 1997) while the orthorhombic phase can be obtained by heating the respective raw materials at 1000 ºC for 12 h (Tana *et al.,* 1996), 1000 ºC for 24 h (Noda *et al.*, 1979), 1150 ºC for 4 h (Ananta *et al.*, 1999), 1150 ºC for 48 h (Koenitzer *et al.* 1980), and 1200 ºC for 24 h (Harrison *et al.*, 1989).

Figure 3.4 shows the XRD pattern of the Pt-$FeNbO_4$ after heat-treatment at 850 ºC for 1 h, which identifies the orthorhombic crystal structure of Pt-$FeNbO_4$. No characteristics diffraction lines corresponding to Pt were observed in the XRD pattern, possibly due to high dispersion of Pt particles in the oxide matrix. EDX analysis

(Figure 3.5) of the powders calcined at 850 ºC confirmed the expected chemical composition of the Pt-$FeNbO_4$ sample with the stoichiometric ratio of Fe: Nb in the composition being 1:1.

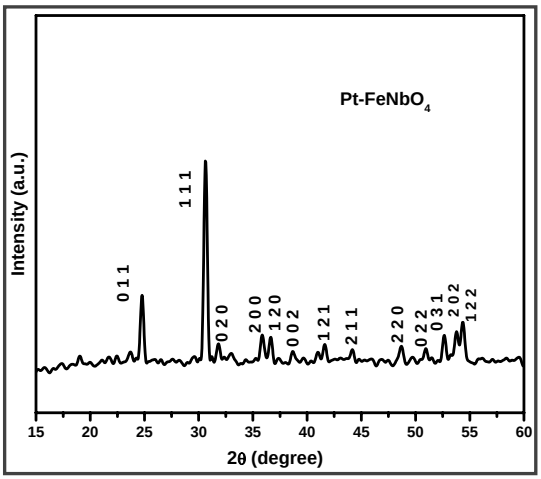

Figure 3.4: *X-ray diffractogram (using* CuK_α *radiation) of the platinum incorporated* $FeNbO_4$ *after calcination at 850 ºC for 1 h.*

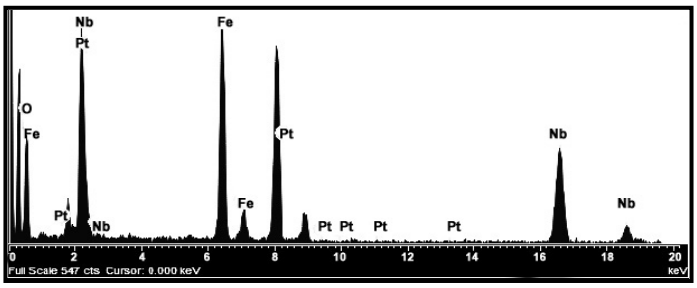

Figure 3.5: *EDX pattern of (1 wt%) platinum incorporated* $FeNbO_4$ *after calcinations at 850 ºC for 1 h.*

3.6.3 Morphology and Microstructural Studies of the Nanocrystalline $FeNbO_4$ *and Pt-*$FeNbO_4$ *Powders*

The microstructural information of the synthesized $FeNbO_4$ and Pt-$FeNbO_4$ powders was obtained through transmission electron microscopy (TEM) studies. Figure 3.6 and 3.7 show the bright field electron micrographs of the synthesized $FeNbO_4$ and Pt-

$FeNbO_4$ powders respectively. The smallest particles visible in the micrograph can be identified as single crystallites and/or their aggregates with particle size in the range of 35-60 nm. Introduction of platinum in $FeNbO_4$ matrix did not reveal any significant change in the particle size of nanocrystalline powders as can be seen from the TEM micrographs. The selected-area electron diffraction (SAED) pattern of the heat-treated (850 ºC for 1 h) Pt-$FeNbO_4$ powders (inset Figure 3.7) showed spotty ring pattern, a characteristics of an assembly of polycrystallites diffracting coherently.

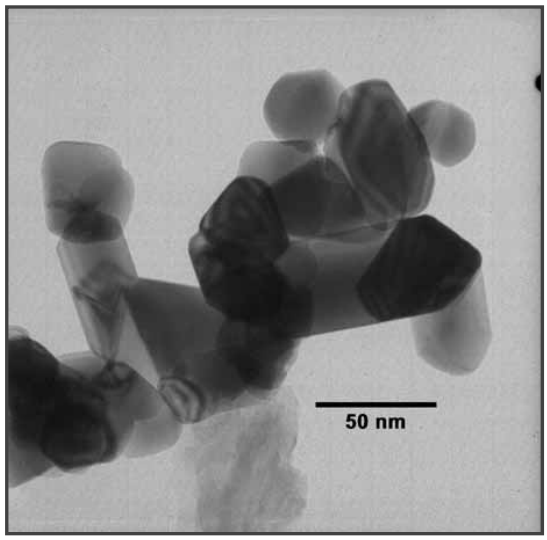

Figure 3.6: *Bright field TEM micrograph of the calcined (at 850 ºC for 3 h) $FeNbO_4$.*

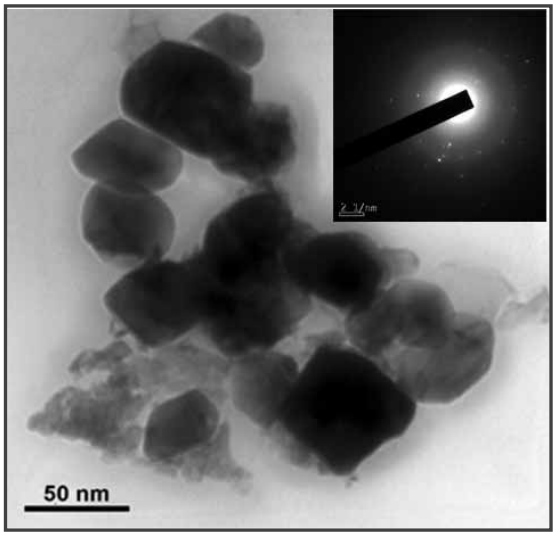

Figure 3.7: *Bright field TEM micrograph of Pt-$FeNbO_4$ after calcination (at 850 ºC for 1 h). (Inset) SAED pattern of Pt-$FeNbO_4$.*

Field-emission scanning electron microscopy (FESEM) studies were carried out using porous pellets which were obtained by compression of the prepared nanocrystalline powders of $FeNbO_4$ and Pt-$FeNbO_4$. Figure 3.8 and 3.9 illustrate the FESEM micrographs of the pellets surface, obtained from $FeNbO_4$ and Pt-$FeNbO_4$ respectively. Surfaces of both the pellets showed sufficient porosity as well as microstructural irregularities resulting from grain growth during the pellet fabrication. The large porous aggregates were observed to be composed of weekly bound smaller individual particles on the surface of the pellets of both, $FeNbO_4$ and Pt-$FeNbO_4$. Porous surface of the pellets is desirable for a gas sensor, since in the porous surface

the volume of the surface layer is also accessible to the gases and thus, the active-surface area for the test gas the adsorption becomes much higher in comparison to the geometric one.

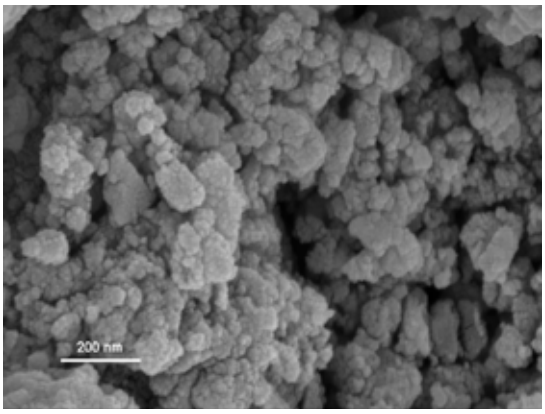

Figure 3.8: *FESEM micrograph of pellet derived from the calcined (at 850 ºC for 2 h) powders of the nanocrystalline $FeNbO_4$.*

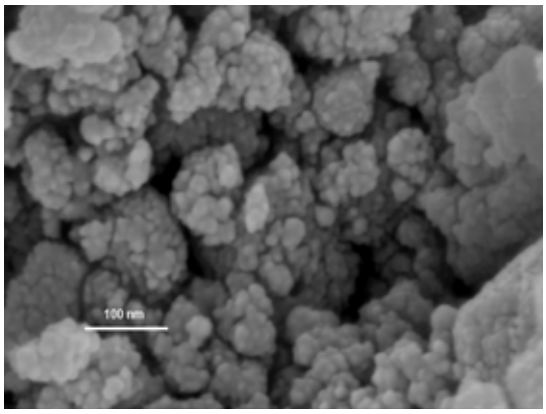

Figure 3.9: *FESEM micrograph of pellet derived from the calcined (at 850 ºC for 1 h) powders of the nanocrystalline Pt-$FeNbO_4$.*

Figure 3.10 depicts BET isotherms for the nanocrystalline powders of $FeNbO_4$ and platinum (1 wt%) incorporated $FeNbO_4$. It has been found that the sensor materials having larger surface areas would be more sensitive to analyte gases. The surface areas measurements through BET technique showed that both, $FeNbO_4$ and Pt-

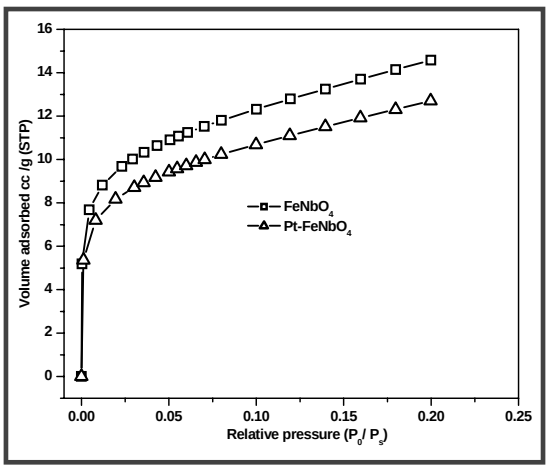

Figure 3.10: *BET isotherms of nanocrystalline $FeNbO_4$ and platinum (1 wt%) incorporated $FeNbO_4$.*

$FeNbO_4$ had almost similar specific surface areas and they were found to be 51 (±2) m^2g^{-1} and 48 (±2) m^2g^{-1} respectively. BET surface area measurements inferred that incorporation of platinum in the nanocrystalline $FeNbO_4$ matrix did not alter their particle size and specific surface area significantly.

3.6.4 Electrical Measurements and Gas Sensing Studies of the Nanocrystalline $FeNbO_4$ and Pt-$FeNbO_4$

Electrical resistances as well as gas sensing properties of the synthesized material were studied by two probes *dc* conductivity measurements. The electrical and gas sensing measurement procedures followed for the study have been detailed in the previous chapter (Chapter 2, Section 2.6.4). The setup used and the methodology followed for the electrical and gas sensing studies for the synthesized nanocrystalline powders of $FeNbO_4$ and Pt-$FeNbO_4$ remained the same. Resistances of the sensors were measured using an electrometer (Model 616, M/s Keithley Instruments, USA). The responses of the material were examined towards H_2, LPG and NH_3 in the temperature range of 150-400 ºC.

3.6.4.1 Electrical Measurements of the Nanocrystalline $FeNbO_4$ and Pt-$FeNbO_4$

The electrical conductivities for the $FeNbO_4$ as well as the Pt-$FeNbO_4$ pellets were measured in dry air at different temperatures (150-400 ºC). The effect of the temperature on the *dc* electrical conductivity (σ) for both the sample pellets has been illustrated in Figure 3.11. The plots of logarithms of conductivities of the sample pellets (of both the compositions) versus reciprocal temperatures (1/T) (Figure 3.11) showed that the electrical conductivities (σ) of both the materials increased with the temperature. This could be attributed to the increase in mobility of electric charge carriers, which are thermally activated upon increase in temperature. The observed increase in conductivities (σ) with the temperature is a normal behavior for all semiconductors, which follows the Arrhenius relation,

$$\sigma = \sigma_o e^{\frac{E_a}{KT}}$$

where σ_o is a pre-exponential factor while E_a, k, and T are the activation energy for conduction, Boltzmann's constant, and absolute temperature, respectively. The logarithms of conductivities of both the sample pellets were found to be varied linearly with reciprocal temperature (1/T) with no hysteresis during heating and cooling cycles.

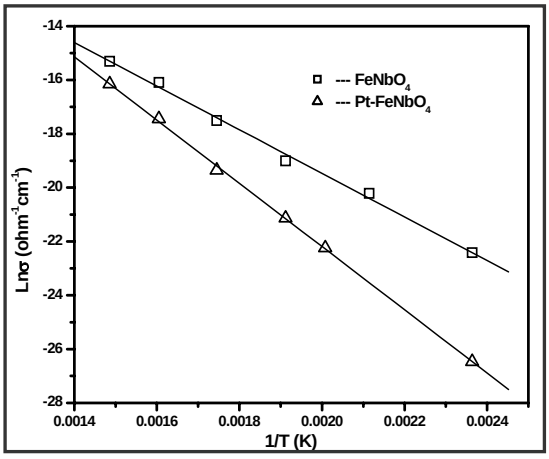

Figure 3.11: *Arrhenius plot for electrical conductivity for the $FeNbO_4$ and platinum (1 wt %) incorporated $FeNbO_4$ pellets in air.*

The semiconductor behavior of $FeNbO_4$ and Pt-$FeNbO_4$ can be attributed to oxygen deficiency (Gnanasekar *et al.*, 1999) which leads to the generation of small fraction of Fe^{2+} ions (Schmidbauer *et al.*, 1997). The activation energies for $FeNbO_4$ and Pt-$FeNbO_4$, as estimated from the plots, were found to be 0.698 eV and 1.03 eV respectively. In the low temperature range, the activation energy for $FeNbO_4$ with orthorhombic structure may be due to the extrinsic conduction for oxygen vacancies (Schmidbauer *et al.*, 1997). Since the particle/crystallite sizes of $FeNbO_4$ and Pt-$FeNbO_4$ were found to be comparable (from TEM and XRD studies), thus the contribution of particle size (Neri *et al.*, 2006) towards higher activation energy of Pt-$FeNbO_4$ can then be ruled out. The higher value of activation energy of the Pt-$FeNbO_4$ system can therefore, be attributed to the alteration of the oxygen stoichiometry on the oxide surface due to incorporation of platinum (Safonova *et al.*, 2001). In presence of

platinum, the adsorption and dissociation of molecular oxygen is enhanced and the dissociated oxygen can spill over on to the $FeNbO_4$ surface and trap the electrons from metal oxide conduction band. This increases the Schottky electron barrier height and consequently the resistance of Pt-$FeNbO_4$. Both the materials showed typical *n*-type conductivity behavior since a reducing gas reduces their electrical resistance and their resistance increases when exposed to O_2.

3.6.4.2 Gas Sensing Studies of the Nanocrystalline $FeNbO_4$ and Pt-$FeNbO_4$

The gas sensing characteristics of the pellet sensors made from nanocrystalline powders of $FeNbO_4$ and Pt-$FeNbO_4$ were investigated towards LPG, H_2 and NH_3 at various temperatures in the range of 150-400 ºC. Figure 3.12 shows the response characteristics of the pellets of $FeNbO_4$ and Pt-$FeNbO_4$ towards 500 ppm of LPG, H_2 and NH_3 at various operating temperatures ranging from 150-400 ºC. $FeNbO_4$ pellets exhibited the maximum sensitivity towards H_2 (93%) at 250 ºC, and towards LPG (92%), and NH_3 (52%) at 300 ºC. Incorporation of Pt in the nanocrystalline $FeNbO_4$ was observed to reduce the sensor operating temperatures. Pt-$FeNbO_4$ pellets showed the maximum response towards H_2 (94%) at 175 ºC, towards LPG (94.5%) at 200 ºC, and towards NH_3 (61.5%) at 250 ºC. However, the response was found to decrease with increase in the operating temperatures. Incorporation of platinum in the nanocrystalline powders of $FeNbO_4$ thus improved the sensor quality of the material by reducing the response time and the sensor recovery time, as can be seen from the Figure 3.13, which compares the response characteristics of $FeNbO_4$ and platinum (1 wt%) incorporated $FeNbO_4$ towards 500 ppm of LPG at 200 ºC. The response and recovery time (at the temperature when maximum response was achieved) for the Pt-$FeNbO_4$ pellets were observed to be around 55 seconds and 90 seconds respectively for H_2 (at 175 ºC) and for NH_3, the respective values were 100 seconds and 150 seconds (at 250 ºC). The basic signal quality (of three such cycles) for the Pt-$FeNbO_4$ pellet is shown in Figure 3.14, which represents the reproducibility and durability of the sensor material. The gas sensing phenomenon is intimately related to the surface catalyzed reaction; therefore the high surface areas of the sensors are expected to

increase the rate of the reaction and hence the sensing behavior. Since both the samples showed almost equal surface areas, improvement in the sensing properties of Pt-$FeNbO_4$ pellets compared to that of the $FeNbO_4$ pellets could be attributed to the incorporation of platinum. The typical responses of Pt-FeNbO4 pellets towards LPG of different concentration (100, 300, 500 ppm) at 200 ºC were found to increase almost linearly with concentrations.

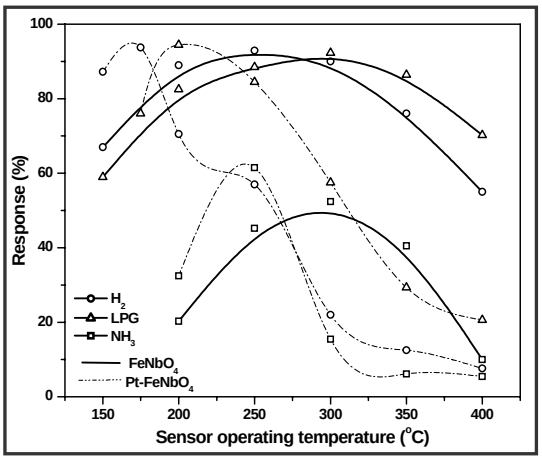

Figure 3.12: *Response characteristics of nanocrystalline $FeNbO_4$ and Pt-$FeNbO_4$ in porous pellet forms towards 500 ppm each of H_2, LPG, and NH_3 in air as a function of temperature.*

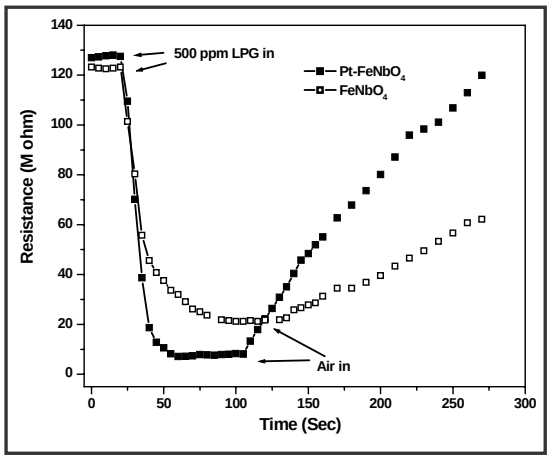

Figure 3.13: *Response characteristics of $FeNbO_4$ and platinum (1 wt %) incorporated $FeNbO_4$ for 500 ppm of LPG at 200 ºC.*

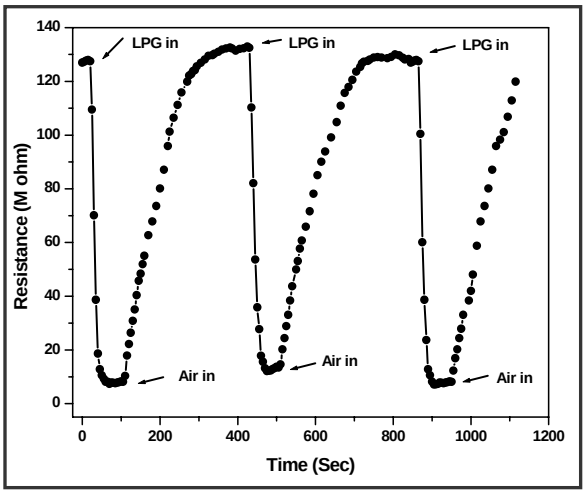

Figure 3.14: *Electrical resistance of Pt-$FeNbO_4$ in alternating environments of air and LPG (500 ppm) at 200 ºC.*

The observed decrease in response at higher operating temperatures for $FeNbO_4$ and Pt-$FeNbO_4$ samples, as can be seen in Figure 3.12 might be due to the increase of desorption kinetics on the surface of the sensor materials at higher temperature. The physical properties of the semiconducting sensor material such as, concentration of charge carriers, Debye length are also influenced by temperature. At higher temperature the carrier concentration of the oxide sensors increases and the Debye length decreases. This may be one of the possible reasons for the decrease in the response of the sensor material towards test gases at higher temperatures. The possible causes of the decrease of responses at higher operating temperatures have been elaborately discussed in Chapter 2, Section 2.6.4.2 of this thesis

In gas sensing phenomenon, the reducing gas e.g. H_2, LPG etc. gets oxidized by the surface chemisorbed oxygen ions (like O^-, O^{2-}, O_2^-, etc.), releasing the electrons, which enhance the charge in the conduction band of the *n*-type oxide and hence increase the conductivity (decrease the potential barrier). The probable reactions taking place on the oxide sensor surface have been discussed in Chapter 2, Section 2.6.4.2.

3.7 Major Findings in the present Investigation

- Nanocrystalline powders of $FeNbO_4$ have been synthesized by aqueous based metal ion-ligand complex based precursor route.
- The preparative method established the use of niobium tartrate which is a stable water-soluble source of niobium.
- The orthorhombic phase of $FeNbO_4$ was realized at 850 ºC, which is the lowest temperature reported in the literature so far, and thus large agglomeration in the powders were prevented.
- Platinum incorporated $FeNbO_4$ was prepared by impregnation method.
- The average crystallite sizes, average particle sizes and specific surface areas for both $FeNbO_4$ and Pt-$FeNbO_4$ systems (determined from XRD, TEM and

BET surface area measurements) were found to be comparable and their values were 20 nm, 35-60 nm and 48-51 m^2g^{-1} respectively.

- Both nanocrystalline $FeNbO_4$ and platinum incorporated nanocrystalline $FeNbO_4$ showed n-type semiconductor behavior.

- In present study, nanocrystalline $FeNbO_4$ and platinum incorporated nanocrystalline $FeNbO_4$ in the temperatures range of 150-400 ºC showed the higher sensitivities to H_2, LPG and NH_3 compared to all previous reports.

- Compressed pellets of both, nanocrystalline powders of $FeNbO_4$ and Pt-$FeNbO_4$, showed almost similar sensitivities towards H_2, LPG and NH_3 in the temperatures range of 150-400 ºC, but the platinum incorporation improved the sensor quality of $FeNbO_4$ by reducing the sensor operating temperature along with a decrease in the response time and sensor recovery time.

References

Ananta, S., Brydson, R. and Thomas, N. W. (1999), Synthesis, Formation and Characterisation of $FeNbO_4$ Powders, Journal of the European Ceramic Society, Vol. 19, No. 4, pp. 489-496.

Dawson, D. H. and Williams, D. E. (1996), Gas-Sensitive Resistors: Surface Interaction of Chlorine with Semiconducting Oxides, Journal of Materials Chemistry, Vol. 6, No. 3, pp. 409-414.

Gnanasekar, K.I., Jayaraman, V., Prabhu, E., Gnanasekaran, T. and Periaswami, G. (1999), Electrical and Sensor Properties of $FeNbO_4$: A New Sensor Material, Sensors and Actuators B, Vol. 55, 170-174.

Harrison, W. T. A. and Cheetham, A. K. (1989), Structural and Magnetic Properties of $FeNbO_4$-II, Materials Research Bulletin, Vol. 24, pp. 523-527.

Henshaw, G. S., Morris, L., Gellman L. J. and Williams, D. E. (1996), Selectivity and Compositional Dependence of Response of Gas-Sensitive Resistors Part 4.-Properties of Some Rutile Solid Solution Compounds, Journal of Materials Chemistry, Vol. 6, No. 12, pp. 1883-1887.

Kim, E.S., Jeon, J.S. and Yoon, K.H. (2003), Effect of Sintering Method on The Microwave Dielectric Properties of $(Pb_{0.45}Ca_{0.55})(Fe_{0.5}Nb_{0.5})O_3$ Ceramics, Journal of the European Ceramic Society, Vol. 23, No. 14, pp. 2583-2587.

Koenitzer, J., Khazai, B., Hormadaly, J., Kershaw, R., Dwight, K. and Wold, A. (1980), Preparation and Photoelectronic Properties of FeNbO4, Journal of Solid State Chemistry, Vol. 35, pp. 128-132.

Leiva, H., Sieber, K., Khazai, K. and Wold, A. (1982), Structural and Electronic Relationships between Conducting Iron Niobates and Iron Tungstates, Journal of Solid State Chemistry, Vol. 44, No. , pp. 113-118.

Neri, G., Bonavita, A., Micali, G., Donato, N., Deorsola, F. A., Mossino, P., Amato, I. and Benedetti, B. D.(2006), Ethanol Sensors Based on Pt-Doped Tin Oxide Nanopowders Synthesised by Gel-Combustion, Sensors and Actuators B: Chemicals, Vol. 117, No. 1, pp. 196-204.

Noda, Y., Shimada, M., Koizumi, M. and Kanamaru, F. (1979), Magnetic and Electrical Properties and Mössbauer effect in the Solid Solution $Fe(Nb_{1-x}W_x)O_4$ $(0\leq x\leq 1)$, Journal of Solid State Chemistry, Vol. 28, pp. 379-384

[a]Pourroy, G., Malats, I., Riera, I., Poix, P. and Poinsot, R. (1990), Low Temperature Syntheses of $NbFeO_4$ and $TaFeO_4$. Influence of Recrystallization on the Magnetic Properties, Journal Solid State Chemistry, Vol. 88, pp. 476-484.

[b]Pourroy, G., Lutanie, E. and Poix, P. (1990), Transition Orthorhombic Rutile in $xMFeO_4$-$(1-x)ZnF_2$ Phases (M=Ta, Nb and x> 0.7), Journal of Solid State Chemistry, Vol. 86, pp. 41-49.

Roth, R. S. and Waring, J. L. (1964), Ixiolite and Other Polymorphic Types of $FeNbO_4$, American Mineralogist, Vol. 49, pp. 242-246.

Safonova, O.V., Rumyantseva, M. N., Ryabova, L. I., Labeau, M., Delabouglie, G. and Gaskov, A. M. (2001), Effect of Combined Pd and Cu Doping on Microstructure, Electrical and Gas Sensor Properties of Nanocrystalline Tin Dioxide, Material Science and Engineering B, Vol. 85, No. 1, pp. 43-49.

Schmidbauer, E. and Schneider, J. (1997), Electrical Resistivity, Thermopower, and ^{57}Fe Mössbauer Study of $FeNbO_4$, Journal of Solid State Chemistry, Vol. 134, pp. 253-264.

Shrout, T. R. and Halliyal, A. (1987), Preparation of Lead-Based Ferroelectric Relaxors for Capacitors, American Ceramic Society Bulletin, Vol. 66, pp. 704-711.

Tena, M. A., Garcia-Belmonte, G., Bisquert, J., Escribano, P., Colomer, M. T. and Jurado, J. R. (1996), Impedance Spectroscopy Studies of Orthorhombic $FeNbO_4$, Journal of Materials Science, Vol. 31, pp. 2043-2046.

Chapter 4

Synthesis of Nanocrystalline Powders of $CuGa_2O_4$ and Studies on their Gas Sensing Behavior towards Ammonia, Hydrogen and Liquefied Petroleum Gas

Chapter 4

Synthesis of Nanocrystalline Powders of $CuGa_2O_4$ and Studies on their Gas Sensing Behavior towards Ammonia, Hydrogen and Liquefied Petroleum Gas

4.1 Introduction

Metal oxide based semiconductors materials are recognized for their gas sensing properties but the search for innovative metal oxide compositions/properties for superior detection of inflammable and toxic gases in air continue to be one of the major fields of sensor research till date. Importance of the semiconductor metal oxide based solid state gas sensors (usually operating at temperatures higher than ambient) can be attributed to their high sensitivity, fast response, high chemical & thermal stability, high reliability, low cost, and to their compact size.

Of the various oxide materials, the transition metal based composite/ complex oxide compositions have attracted great attention in recent years for their enhanced response towards different reducing/oxidizing or inflammable & toxic gases in air (Mohammadi *et al.*, 2007). Titanates (Gerblinger *et al.*, 1994; Chu *et al.*, 1999), stannates (Fergus, 2007; Jayaraman et al., 1996; Tao *et al.*, 2000), niobates (Dawson *et al.*, 1996; Gnanasekar *et al.*, 1999), ferrites (Baruwati *et al.*, 2007; Lee *et al.*, 2006; Liu *et al.*, 2005; Sun *et al.*, 2007) and tantalates (Moseley *et al.*, 1988) are among the significant transition metal based complex oxide compositions that have been prepared and extensively investigated for their gas sensing behaviors towards different gases. A number of spinel ferrite systems, with a general formula of AB_2O_4, have also been reported for their gas-sensing characteristics (Lou *et al.*, 2007).

Review of the available literature on gas sensors material reveals that transition metal gallates are among the least investigated oxide systems so far. $ZnGa_2O_4$ (Satyanarayana *et al.*, 1998) and $Cd_{1-x}Mg_xGa_2O_4$ (Jihua *et al.*, 2006) with spinel structures, are the only two transition metal gallate systems that have been

studied for their gas sensing behavior till date. The present study embarks up on the preparation of the spinel structured copper gallate ($CuGa_2O_4$) and investigates their sensing property towards various inflammable and toxic reducing gases for the very time.

$CuGa_2O_4$ has a magnetic spinel with tetrahedral and octahedral lattice sites, in which approximately 84% of the Cu^{2+} ions occupy the octahedral sublattice sites, while the Ga^{3+} ions fill the rest. Thus, the structure of the $CuGa_2O_4$ can be represented by the formula: $(Cu_{1-\delta}Ga_{\delta})^{tet}[Cu_{\delta}Ga_{2-\delta}]^{oct}O_4$, where δ is the inversion coefficient (0.84) (Stone *et al.*, 1985). High degree of inversion in the spinel is due to tetrahedral preference of the Ga^{3+} ions. Such a preference is a common among d^{10} ions in spinel structures, due to the strong covalent contribution, which can be developed in the bond between a four coordinated cation and an anion. Although there are a number of examples of spinel-type oxides that demonstrate good gas sensing properties, information on the gas sensing characteristics of nanocrystalline spinel $CuGa_2O_4$ system is conspicuously absent in the literature so far. The present chapter on targets this inadequacy and thus, focuses on the synthesis of nanocrystalline $CuGa_2O_4$ powders through the developed chemical process, and studies of their sensing response towards different reducing gases such as, H_2, liquefied petroleum gas (LPG), and NH_3.

4.2 Reported Methods for the Preparation of $CuGa_2O_4$

$CuGa_2O_4$ has been prepared and studied by a number of groups for determining its crystal structure. Preparation of spinel $CuGa_2O_4$ has usually been reported through the conventional solid-state method, the chemical synthesis of $CuGa_2O_4$ is rare in literature. Some of the existing reports for the synthesis of $CuGa_2O_4$ are summarized below.

4.2.1 Conventional Solid-State Method

Similar to the $CuNb_2O_6$ and $FeNbO_4$ compositions, the common technique for the preparation of $CuGa_2O_4$ powders is also found to be the conventional solid-state reaction, which requires mechanical mixing of stoichiometric amounts of the raw materials (such as, CuO and Ga_2O_3) followed by repeated milling and calcination. Stone *et al.* (1985) have reported the preparation of polycrystalline $CuGa_2O_4$ powders through the solid-state method by mixing Ga_2O_3 and CuO in an appropriate proportion and annealing at around 950 ºC for 24 h. González *et al.* (1985) have also prepared polycrystalline $CuGa_2O_4$ powders by solid-state method and have reported the distributions ions in the spinel structure.

4.2.2 Chemical Method

Despite the advantages of better chemical homogeneity offered through the chemical synthesis process in comparison to solid-state method, there is no report on the preparation of $CuGa_2O_4$ through wet chemical method in literature. In the present investigation, an aqueous based chemical synthesis process has been developed for the preparation of nanocrystalline $CuGa_2O_4$ powders using simple metalo-organic complex chemistry.

4.3 Scope of the Present Investigation

The present study describes the aqueous based chemical synthesis of nanocrystalline powders of $CuGa_2O_4$ through metal ion-ligand complex based precursor route. In the developed process, the aqueous based metal ion-ligand complex precursor solution is obtained by mixing aqueous solution of copper nitrate and gallium nitrate with triethanolamine (TEA) in the required amounts. The precursor solution is then pyrolyzed to voluminous carbonaceous mass through oxidative decomposition of the metalo-organic complexes. This solid precursor is calcined at 750 °C for 2 h to obtain the nanocrystalline powders of $CuGa_2O_4$.

In the present study, the sensing characteristics of the prepared nanocrystalline $CuGa_2O_4$ powders towards different reducing gases (such as, H_2, liquefied petroleum gas (LPG), and NH_3) have also been investigated. The nanocrystalline sensor materials are expected to exhibit increased sensitivity towards the test gases compared to their bulk counter parts due to high specific surface area and reduced size of their grains.

4.4 Synthesis of Nanocrystalline $CuGa_2O_4$ Powders

4.4.1 The Raw Materials Used in the Developed Synthesis Method

i) Copper nitrate, ii) Gallium metal, iii) Triethanolamine (TEA), iii) Ammonia (25%), and iv) Nitric acid (70%). All the materials were procured from M/S Aldrich (U.S.A).

In this study, aqueous solution gallium nitrate was prepared in the laboratory from gallium metal and stocked for use as a source of gallium in the synthesis of nanocrystalline powders of $CuGa_2O_4$.

4.4.1.1 Preparation of Aqueous Solution of Gallium Nitrate

An aqueous solution of gallium nitrate was prepared by dissolving weighed amount of metallic gallium in minimum quantity of concentrated nitric acid under control heating followed by addition of required amount of deionized water to make a 0.1M aqueous solution of gallium nitrate.

4.4.2 Synthesis of Nanocrystalline Powders of $CuGa_2O_4$

100 ml of aqueous solution of copper nitrate (0.1 M) was mixed with 200 ml of aqueous solution of gallium nitrate (0.1 M), maintaining the molar ratio of Cu^{2+}: Ga^{3+} at 1:2 in the solution mixture. TEA (4 moles per mole of cations present in the solution mixture) was then added into the solution mixture under constant stirring.

The pH of the final solution mixture was maintained at almost 6 with the help of ammonia to avoid any undesired precipitation. This solution was then heated at about 200 ºC until complete dehydration occured and metalo-organic complexes underwent oxidative-decomposition with the evolution of dense fumes to generate a voluminous fluffy carbonaceous mass. The black fluffy mass was then crushed into powders. Calcination of this carbonaceous precursor powders at 750 ºC for 2 h produced carbon-free nanocrystalline powders of $CuGa_2O_4$ in the spinel structure. The method for the preparation is schematically depicted in Figure 4.1.

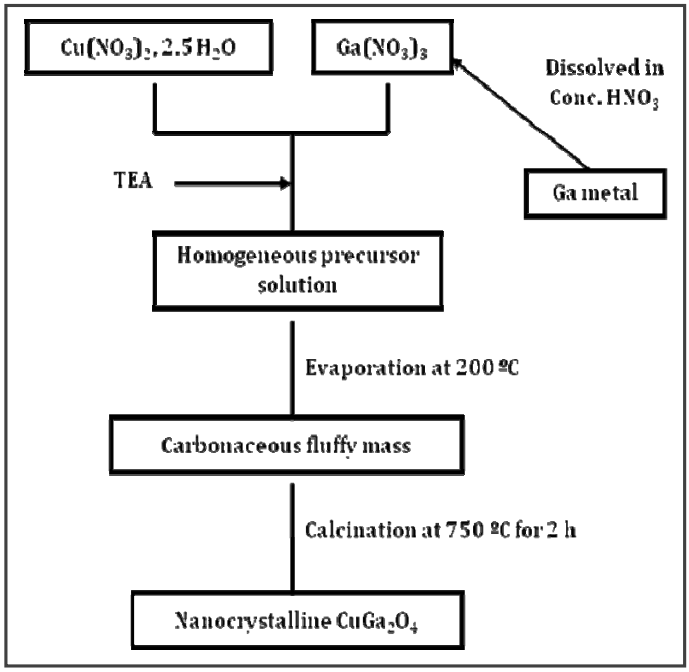

Figure 4.1: *Schematic representation of the preparation of the nanocrystalline powders of $CuGa_2O_4$.*

4.5 Techniques for Characterization of the Prepared Nanocrystalline $CuGa_2O_4$ Powder

The carbonaceous precursor powders of $CuGa_2O_4$ calcined at different temperatures were characterized by X-ray powder diffraction (XRD). The data were collected over the 2θ angle range $20^\circ \leq 2\theta \leq 80^\circ$ with a step size of 0.05°. For the structural

characterization, the Rietveld refinement of XRD data was carried out. The average crystallite size of the compositions was calculated using Scherrers equation. For morphological analysis, TEM and FESEM studies of the synthesized nanocrystalline powders of $CuGa_2O_4$ were carried out. The specific surface areas of the calcined powders were determined using the BET technique. The instruments, used for the characterization remained the same as is mentioned in Chapter 2, Section 2.5.

4.6 Results and Discussion

4.6.1 Composition, Phase and Structural Analysis of the Nanocrystalline $CuGa_2O_4$ Powders

Phase analysis and structural characterization of the prepared $CuGa_2O_4$ powders were carried out through room temperature X-ray powder diffraction (XRD) studies. Figure 4.2a shows the XRD patterns of the carbonaceous powders of $CuGa_2O_4$ calcined at different temperatures (ranging from 550 °C to 750 °C) for 2 h. The onset of crystallization process in the precursor powder sample was noticeable through the

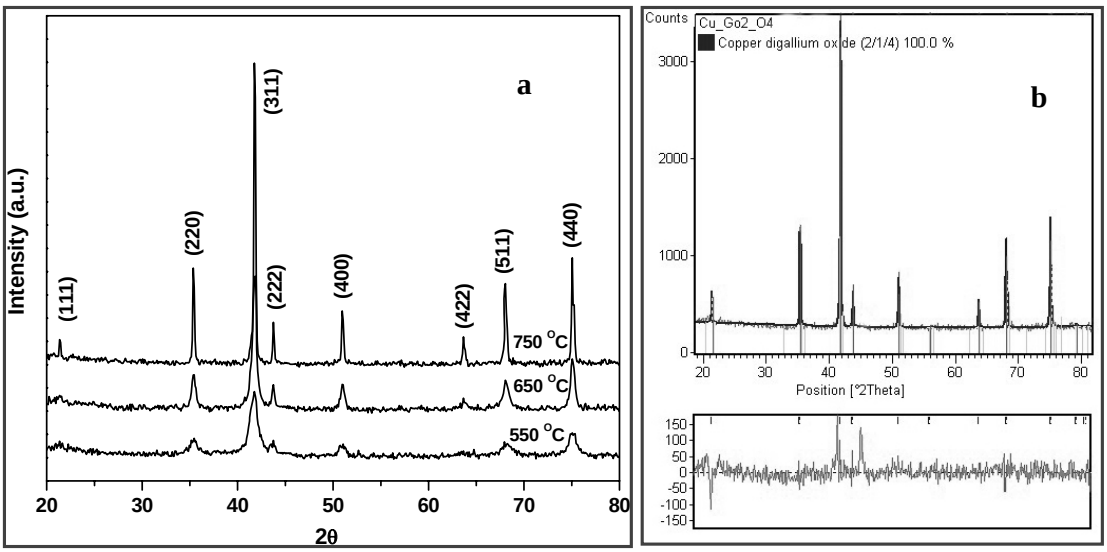

Figure 4.2: ***(a)*** *X-Ray diffractogram (using CoK_α radiation) of the $CuGa_2O_4$ calcined at 750 ºC for 2 h.* ***(b)*** *Rietveld refinement of monoclinic $CuGa_2O_4$ calcined at 750 ºC for 2 h. Vertical bars show the positions of Bragg reflections.*

incipient peaks in the XRD pattern when the carbonaceous precursor of $CuGa_2O_4$ was calcined at 550 °C for 2 h. Calcination at this low temperature could not completely crystallize the material; the low intensity diffraction lines in the XRD pattern indicated a poor crystallinity in the sample on calcination at 550 °C for 2 h. To obtain crystalline powders of $CuGa_2O_4$ sample, the carbonaceous precursor powders of the sample were calcined at 750 °C for 2 h and a single phase $CuGa_2O_4$ was realized after calcination at 750 °C for 2 h. The absence of any additional diffraction lines in XRD of the powders calcined at 750 ^oC for 2 h confirmed the formation of a pure spinel phase of $CuGa_2O_4$ as per the standard data reported in JCPDS file (card no. 044-0183) and the diffraction lines were indexed accordingly. In order to further characterize this system, Reitveld refinements from the X-ray data (Figure 4.2b) was performed. Reitveld refinement did provide precise lattice parameters. The lattice parameters [$a = b = c = 8.2919(6)$ Å and $\alpha = \beta = \gamma = 90$] of the sample matched closely with the standard lattice parameter values. A few more data for spinel $CuGa_2O_4$ have been summarized in Appendix C. The average crystallite size of the synthesized powders evaluated from line broadening analysis using a Scherrers formula was found to be 30 nm.

The chemical composition of the calcined powders at 750 °C was analyzed using Energy dispersive X-ray spectroscopy (EDX). EDX analysis (Figure 4.3) of the calcined powders at 750 ºC confirmed the expected chemical composition of $CuGa_2O_4$ with the observed stoichiometric ratio of Cu: Ga in the compound of 1:2.

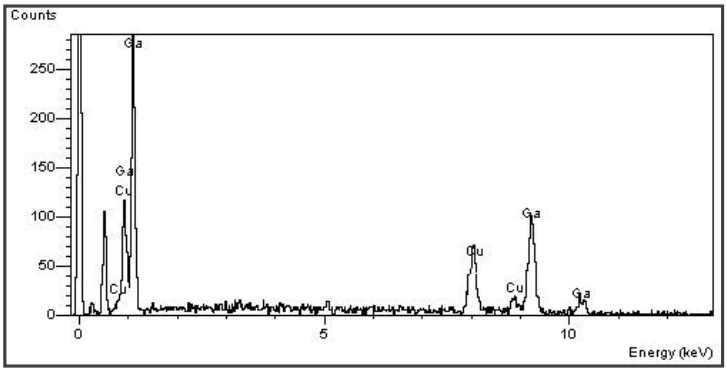

Figure 4.3: *EDX analysis of the $CuGa_2O_4$ after calcination at 750 ºC for 2 h.*

Table 4.1: *EDX analysis of the $CuGa_2O_4$ after calcination at 750 ºC for 2 h.*

Element	Atomic%
Cu K	32.6
Ga L	67.4
Total	100

4.6.2 Morphology and Microstructural Studies of the Nanocrystalline $CuGa_2O_4$ Powders

The microstructure of the calcined powders of $CuGa_2O_4$ was observed by transmission electron microscopy (TEM) studies. Figure 4.4 shows the bright field electron micrograph of the synthesized $CuGa_2O_4$. The smallest particles visible in the micrograph can be identified as nanoparticles with size in the range of 30-60 nm. The micrographs showed that the particles were nearly monodisperse and the particle sizes are comparable with the average crystallite size calculated from XRD data using Scherrers equation.

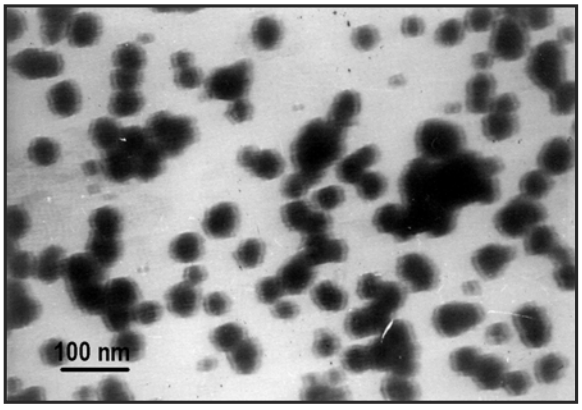

Figure 4.4: *Bright field TEM micrograph of the calcined (at 750 ºC for 2 h) $CuGa_2O_4$.*

Field-emission scanning electron microscopy (FESEM) studies were carried out using both, the calcined powders of $CuGa_2O_4$ and porous pellet of the calcined $CuGa_2O_4$ powders. Figure 4.5 is a FESEM image of the calcined powders of $CuGa_2O_4$ showing a view of morphology of the nanocrystalline particles. The low processing temperature involved in this method prevented hard agglomerations in the powder as seen from the FESEM image. The micrograph revealed that powders were dominated by the approximately spherical particles with distinct grain boundaries that were uniformly distributed with the size in the range of 30-60 nm.

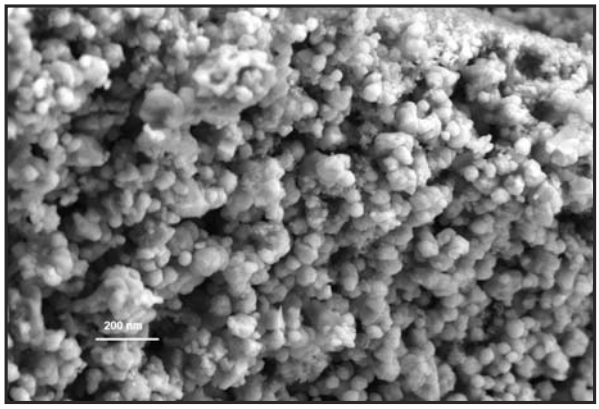

Figure 4.5: *FESEM image of the calcined (at 750 ºC for 2 h) $CuGa_2O_4$ powders.*

The morphological information of the surface of the porous pellets derived from nanocrystalline $CuGa_2O_4$ was obtained from FESEM micrographs. FESEM micrograph of the pellets of calcined $CuGa_2O_4$ powders (Figure 4.6) provided information of the microstructure and topology of the pellet surface. The micrograph clearly showed the presence of large porous aggregates composed of smaller individual particles on the surface of the pellets. It also showed the compression of the powder on pelletization resulted in agglomerations in some portion of the surface of the pellets.

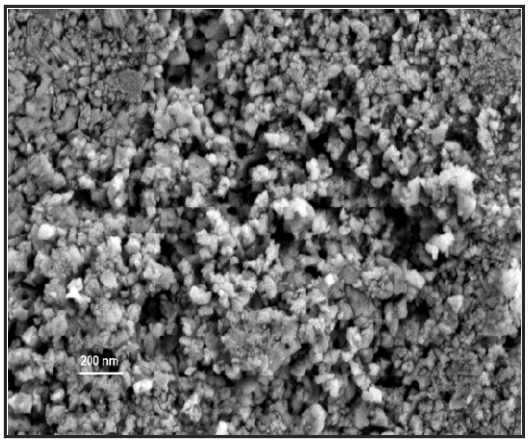

Figure 4.6: *FESEM image of pellet surface derived from nanocrystalline $CuGa_2O_4$ powder.*

The BET surface area of nanocrystalline powders of $CuGa_2O_4$ was found to be 45 m^2g^{-1}.

4.6.3 Electrical Measurements and Gas Sensing Studies of the Nanocrystalline $CuGa_2O_4$ System

Electrical resistances as well as gas sensing properties of the synthesized Nanocrystalline $CuGa_2O_4$ were studied by two probes *dc* conductivity measurements. The electrical and gas sensing measurement procedures followed for this study have been described in detail in the previous chapter (Chapter 2, Section 2.6.4). The setup used and the methodology followed for the electrical and gas sensing studies for the synthesized nanocrystalline powders of $CuGa_2O_4$ remained the same. Resistances of the sensors were measured using DMM (Model 197A, M/s Keithley Instruments, USA) and Agilent Data Acquisition/Switch Unit (model no. 34970A). The responses of the material were examined towards H_2, LPG and NH_3 in the temperature range of 200-400 ºC.

4.6.3.1 Electrical Measurements of the Nanocrystalline $CuGa_2O_4$ System

Electrical conduction in metal oxides is thermally activated process. The variation of electrical conductivity of $CuGa_2O_4$ pellets was measured as a function of temperature in air, and in argon atmosphere in the temperature range of 200-400 °C. Figure 4.7 depicts the *dc* electrical conductivity–temperature behavior of the pellet of $CuGa_2O_4$ in air and in argon which corresponded to Arrhenius-type plots. In the whole temperature range of 200-400 ºC, the conductivity of the material increased almost linearly with temperature with no hysteresis during heating and cooling cycles which indicated the intrinsic characteristic of semiconductor. The activation energies (E_a) determined in terms of the slope of the Arrhenius plots was found to be 0.465 eV in air and 0.488 eV in argon atmosphere (correlation factor of the linear least-squares fit $R > 0.9995$). The material showed typical *n*-type conductivity behavior since its electrical resistance decreased in the presence of reducing gases and the resistance increased when exposed to O_2. The conductivity of $CuGa_2O_4$ pellets in argon was found to be slightly higher than that in air. Due to the absence of oxygen in argon ambience, the adsorbed oxygen on the surface of $CuGa_2O_4$ pellets might be desorbed. This led to a comparatively higher conductivity of the material in argon atmosphere than in air.

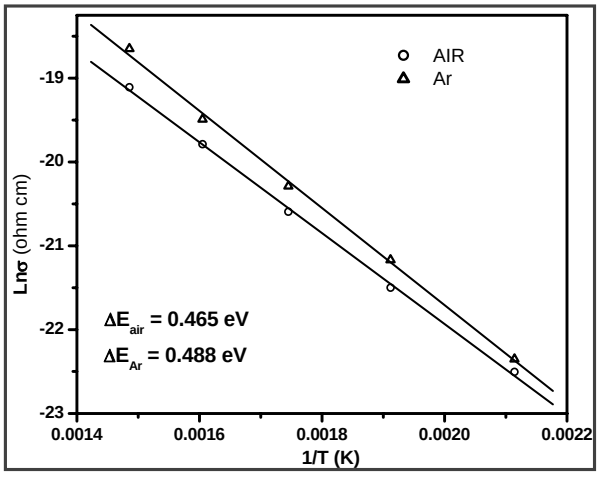

Figure 4.7: *Arrhenius plot for electrical conductivity of $CuGa_2O_4$ in air and argon.*

4.6.3.2 Gas Sensing Studies of the Nanocrystalline $CuGa_2O_4$ System

Figure 4.8-11 demonstrate the typical temperature dependence of response of compressed powder of $CuGa_2O_4$ (sintered at 450 °C for 4 h) towards 500 ppm of H_2, LPG, and NH_3 respectively. Synthesized nanocrystalline $CuGa_2O_4$ showed the maximum responses towards H_2, LPG, and NH_3 at 350 °C. For 500 ppm H_2, the response was found to be around 14% at 200 ºC. It increased to 21% at 250 ºC and then to 35% at 300 ºC. The maximum response of 82% was observed at 350 ºC for the pellets of $CuGa_2O_4$. The response was found to decrease to 66% at 400 ºC. For 500 ppm LPG, observed response of $CuGa_2O_4$ pellets was around 19% at 200 ºC. It increased to 40% at 250 ºC and then to 50% at 300 ºC. For LPG, the maximum response was found to be around 75% at 350 ºC. The response (towards LPG) was observed to decrease to 61% at 400 ºC. Responses towards 500 ppm NH_3 observed at 200 ºC, 250 ºC, 300 ºC, 350 ºC and 400 ºC were 12%, 23%, 25%, 37%, and 36% respectively.

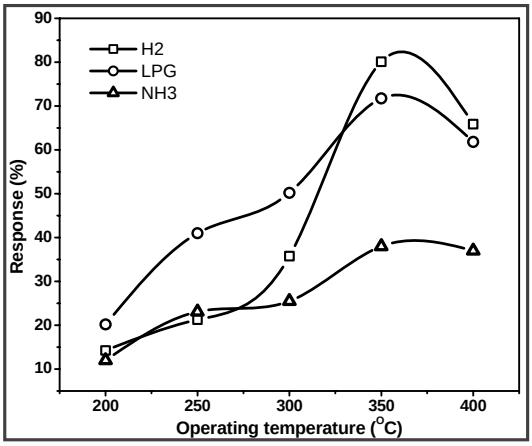

Figure 4.8: *Response characteristics of nanocrystalline $CuGa_2O_4$ in the form of porous pellet towards 500 ppm each of H_2, LPG, and NH_3 in air as a function of temperature.*

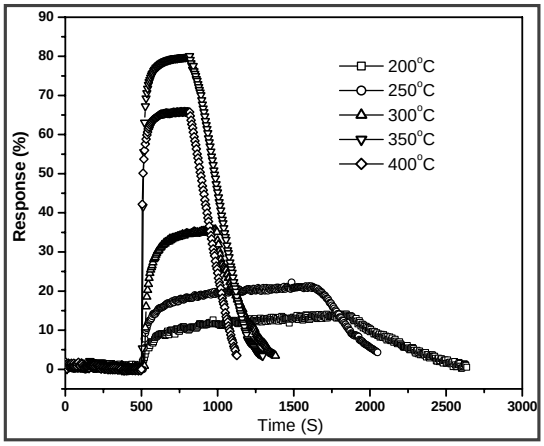

Figure 4.9: *Responses of porous pellet of nanocrystalline $CuGa_2O_4$ towards 500 ppm of H_2 in air at different temperatures.*

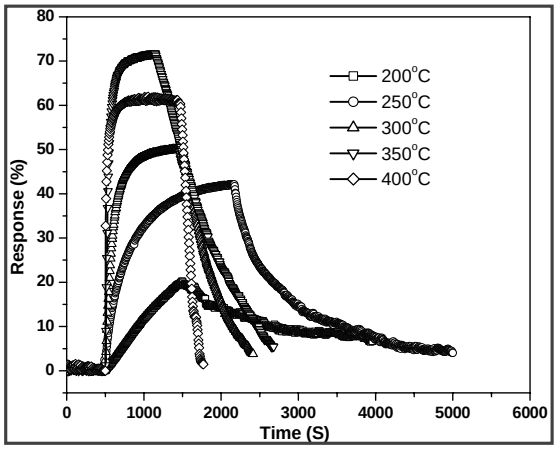

Figure 4.10: *Responses of porous pellet of nanocrystalline $CuGa_2O_4$ towards 500 ppm of LPG in air at different temperatures.*

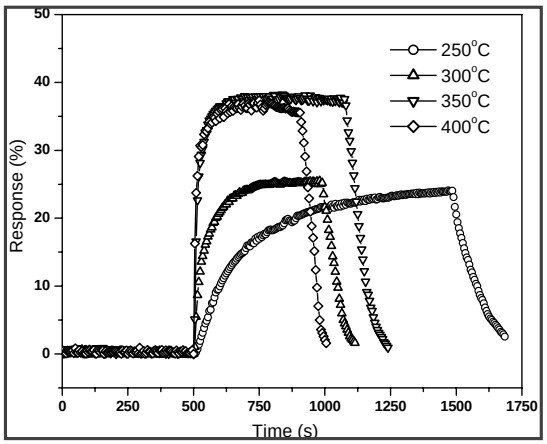

Figure 4.11: *Responses of porous pellet of nanocrystalline $CuGa_2O_4$ towards 500 ppm of NH_3 in air at different temperatures.*

There were three tests were made for each gas at each operating temperature to confirm the results (Chapter 2, Section 2.6.4). Figure 4.12 represents three cycles of response-recovery characteristics of the material exposed to 500 ppm LPG at 350 ºC.

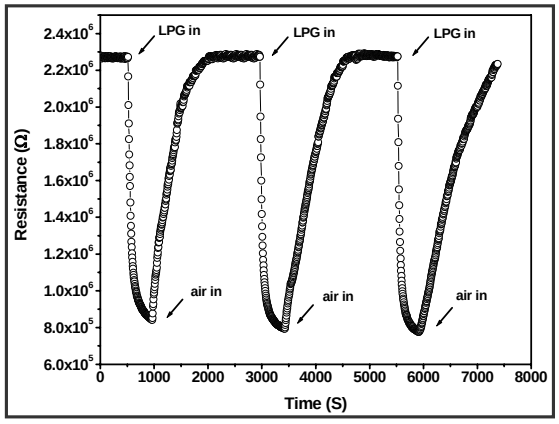

Figure 4.12: *Electrical resistance of porous pellet of $CuGa_2O_4$ in alternating environments of air and 500 ppm LPG at 350 ºC.*

For high responses towards H_2 and LPG at 350 ºC, this temperature was selected for calibration experiments at different concentrations of test gases. Figure 4.13 shows the responses towards H_2 and LPG of different concentrations (100, 300 and 500

ppm) at 350 ºC which were found to be increased almost linearly with gas concentrations.

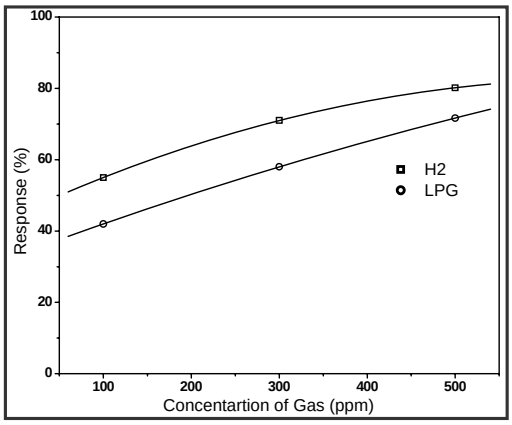

Figure 4.13: *Variation of response of porous pellet of nanocrystalline $CuGa_2O_4$ with concentration of H_2 and LPG at 350 ºC.*

Typical response and recovery characteristics of $CuGa_2O_4$ pellets operating at different temperatures towards 500 ppm of gases are shown in figure 4.14. The response and recovery time (at the temperature when maximum response was achieved) for the pellets of $CuGa_2O_4$ towards H_2 were found to be around 120 s and 460 s respectively (at 350 ºC), and towards LPG, they are 285 s and 1110 s respectively (at 350 ºC), while towards NH_3 the respective values were 105 s and 140 s (at 350 ºC).

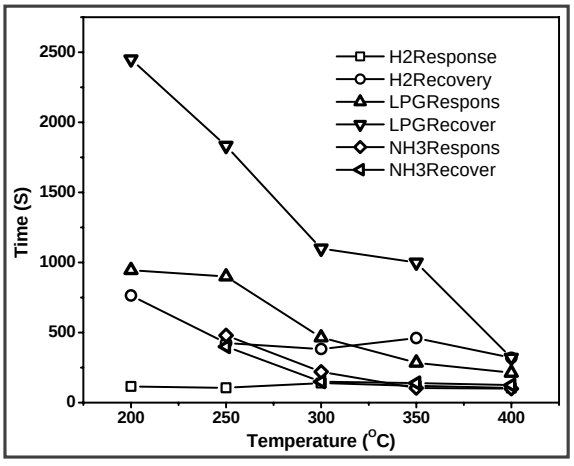

Figure 4.14: *Temperature variation of response time and recovery time for $CuGa_2O_4$ for 500 ppm H_2, LPG and NH_3.*

In gas sensing phenomenon, the reducing gas e.g. H_2, LPG etc. gets oxidized by the surface chemisorbed oxygen ions (like O^-, O^{2-}, O_2^-, etc.), releasing the electrons, which enhance the charge in the conduction band of the *n*-type oxide and hence increase the conductivity (decrease the potential barrier). The probable reactions taking place on the oxide sensor surface have been discussed in the previous chapter (Chapter 2, Section 2.6.4.2).

4.7 Major Findings in the present Investigation

- Nanocrystalline $CuGa_2O_4$ powders have been synthesized by aqueous based metal ion-ligand complex precursor route.
- The spinel structure of $CuGa_2O_4$ was realized at 750 ºC. The low processing temperature in this method prevented grain growth in the powder.
- TEM images showed the average particle sizes in the range of 30-60 nm.
- Nanocrystalline $CuGa_2O_4$ composition showed *n*-type semiconducting behavior.
- Nanocrystalline $CuGa_2O_4$ showed the sensitivities towards H_2, LPG and NH_3.
- The maximum responses of $CuGa_2O_4$ towards H_2, LPG and NH_3 were found to be around 82%, 75%, and 37% at 350 ºC respectively.

References

Baruwati, B., Rana, R. K. and Manorama, S. V. (2007), Further Insights in the Conductivity Behavior of Nanocrystalline $NiFe_2O_4$ in Presence of Liquefied Petroleum Gas, Journal of applied physics, Vol. 101, pp. 0143021-01430217.

Chu, X., Liu, X., Wang, G. and Meng, G. (1999), Preparation and Gas-Sensing Properties of Nano-$CoTiO_3$, Materials Research Bulletin, Vol. 34, No. 10-11, pp. 1789-1795.

Dawson, D. H. and Williams, D. E. (1996), Gas-Sensitive Resistors: Surface Interaction of Chlorine with Semiconducting Oxides, Journal of Materials Chemistry, Vol. 6, No. 3, pp. 409-414.

Fergus, J. W. (2007), Perovskite Oxides for Semiconductor-Based Gas Sensors, Sensors and Actuators B: Chemical, Vol. 123, pp. 1169–1179.

Gerblinger, J., Lampe, U., Meixner, H., Perczel, V. and Giber, J. (1994), Cross-Sensitivity of Various Doped Strontium Titanate Films to CO, CO_2, H_2, H_2O and CH_4, Sensors and Actuators B: Chemical, Vol. 18-19, pp. 529-534.

González, J. M. R. and Areán, C. O. (1985), X-Ray Diffraction Determination of the Cation Distribution and Oxygen Positional Parameter in Polycrystalline Spinels, Journal of the Chemical Society Dalton Transactions, pp. 2155-2159.

Gnanasekar, K.I., Jayaraman, V., Prabhu, E., Gnanasekaran, T. and Periaswami, G. (1999), Electrical and Sensor Properties of $FeNbO_4$: A New Sensor Material, Sensors and Actuators B: Chemical, Vol. 55, 170-174.

Jayaraman, V., Mangamma, G., Gnanasekaran, T. and Periaswami, G. (1996), Evaluation of $BaSnO_3$ and $Ba(Zr,Sn)O_3$ Solid Solutions as Semiconductor Sensor Materials, Solid State Ionics, Vol. 86-88, No. 2, pp. 1111-1114.

Jihua, W., Xiutao, G. and Xingqin, L. (2006), Preparation of Spinel-Type $Cd_{1-x}Mg_xGa_2O_4$ Gas-Sensing Material by Sol–Gel Method, Sensors and Actuators B: Chemicals, Vol. 115, pp. 622–625.

Lee, P.Y., Ishizaka, K., Suematsu, H., Jiang, W. and Yatsui, K. (2006), Magnetic and Gas Sensing Property of Nanosized $NiFe_2O_4$ Powders Synthesized by Pulsed Wire Discharge, Journal of Nanoparticle Research, Vol. 8, pp. 29–35.

Liu, Y.-Li., Liu, Z.-M., Yang, Y., Yang, H.-F., Shen, G.-L. and Yu, R.-Q. (2005) Simple Synthesis of $MgFe_2O_4$ Nanoparticles as Gas Sensing Materials, Sensors and Actuators B: Chemical, Vol. 107, pp. 600-604.

Lou, X., Shi, D., Liu, S. and Peng, C. (2007), Preparation of $CdIn_2O_4$ Powder by Sol–Gel Method and its Cl_2 Sensitivity Properties, Sensors and Actuators B: Chemicals, Vol. 123, pp. 114–119.

Mohammadi, M. R. and Fray D. J. (2007), Semiconductor TiO_2–Ga_2O_3 Thin Film Gas Sensors Derived from Particulate Sol–Gel Route, Acta Materialia, Vol. 55, pp. 4455–4466.

Moseley, P. T., Williams, D. E., Norris, J. O. W. and Tofield, B. C. (1988), Electrical Conductivity and Gas Sensitivity of Some Transition Metal Tantalates, Sensors and Actuators, Vol. 14, No. 1, pp. 79-91.

Satyanarayana, L., Reddy, C. V. G., Manorama, S. V. and Rao, V. J. (1998), Liquid-Petroleum-Gas Sensor Based on a Spinel Semiconductor, $ZnGa_2O_4$, Sensors and Actuators B: Chemicals, Vol.46, pp. 1–7.

Stone, F. S., Areán, C. O., Viñuela, J. S. D., Platerro, E. E. (1985), Structural Characterization of Cadmium-Copper Gallium Oxide ($Cd_xCu_{1-x}Ga_2O_4$) Spinels, Journal of the Chemical Society, Faraday Transactions I, Vol.81, pp. 1255-1261.

Sun, Z., Liu, L., Jia, D. Z. and Pan, W. (2007), Simple Synthesis of $CuFe_2O_4$ Nanoparticles as Gas-Sensing Materials, Sensors and Actuators B: Chemical, Vol. 125 pp. 144–148.

Tao, S., Gao, F., Liu, X. and Sørensen O. T. (2000), Ethanol-Sensing Characteristics of Barium Stannate Prepared by Chemical Precipitation, Sensors and Actuators B: Chemical, Vol. 71, No. 3, pp. 223-227.

Chapter 5

Synthesis of Nanocrystalline Powders of $Ni_{0.1}W_{0.1}Ti_{0.8}O_2$ and $BaNiTi_7O_{16}$ for Pigment Applications

Chapter 5

Synthesis of Nanocrystalline Powders of $Ni_{0.1}W_{0.1}Ti_{0.8}O_2$ and $BaNiTi_7O_{16}$ for Pigment Applications

5.1 Introduction

The most known yellow inorganic pigments are praseodymium-zircon yellow; vanadium–zirconia yellow; tin–vanadium yellow; chromates of alkaline earth metal ions (e.g. calcium, strontium, barium), lead and zinc, litharge (lead oxide); naples yellow (lead antimonate); cadmium yellow; iron oxide yellow (α and γ-FeOOH); and nickel-antimony doped rutile phase TiO_2. Among these inorganic yellow pigments, the application of iron oxide yellow gets constrained due to thermal stability only up to 220 ˚C (Cornell *et al.*, 1996), while the toxicity (Badenes *et al.*, 2002) of chromium (VI), cadmium and lead based yellow pigments restricts their commercial usage. Praseodymium-zircon yellow, tin–vanadium yellow, and vanadium–zirconia yellow though popular in the market of yellow inorganic pigments, have limitations in bulk coloration of porcelainized stoneware at high temperatures (Sorlí *et al.,* 2004a, b).

Nickel-doped TiO_2, with rutile as well as priderite structures are well known intense and brilliant yellow ceramic pigments (Maloney, 2002). They are non-toxic, chemically inert, thermally stable, photochemically inactive, and have tinting strength for the outdoor application and hence satisfy most of the characteristics requisite for pigment application. Despite their partial solubility in transparent glazes above 1000 ºC (Dondi *et al.,* 2006), they have gained considerable attention in recent years as potential alternatives to praseodymium zircon yellow pigment because of their high thermal stability (Bondioli *et al.*, 1999).

Sorlí *et al.* (2004a) have reported the structure and color of nickel doped rutile phase yellow pigment with compositions: $Ni_xA_{1-3x}B_{2x}O_2$ [A = Ti(IV), Sn(IV); B = Sb(V), Nb(V)]. The same group has also studied the role of different nickel precursors on the color of the prepared pigments (Sorlí *et al.*, 2004b). Matteucci *et al.* (2006; Dondi *et al.,* 2006) have studied the role of counter ions (Mo, Nb, Sb, W) in doped

rutile ceramic pigments with compositions $Ni_xA_{1-3x}B_{2x}O_2$ and $Ni_xA_{1-2x}B_xO_2$ [A = Ti(IV), Sn(IV); B = W (VI), Mo(VI)] and found tungsten to be the most suitable counter ions for the best titanate pigments formulation in glaze applications.

For the formation of TiO_2 based yellow pigments, chromophorous ions, Ni^{2+} having ionic radii (ionic radius = 0.69 Å) slightly higher than Ti^{4+} (0.605 Å) are incorporated into the host rutile (TiO_2) lattice to generate oxide solid solutions with stable colorimetric properties. In formulations such as: $Ti^{IV}(W^{VI}Ni^{II})O_2$, the coloring effect is produced when the Ti (IV), which is surrounded by six neighboring oxygen atoms at the corners of a regular (but slightly distorted) octahedron in the rutile lattice, is substituted by transition metal ions of lower valency Ni^{2+} (ionic radius = 0.69 Å) while the higher valency ions in the lattice (e.g., A = W^{6+}; ionic radius = 0.60 Å) compensate for the charge off set such that their molar ratios ensure an overall electroneutrality in the oxide solid solutions. In the present investigation, nickel doped rutile phase titanate pigment with composition: $Ti^{IV}(W^{VI}Ni^{II})O_2$ has been reported as a prototype. In this composition, molybdenum can play the same role of tungsten producing different yellow color.

$BaNiTi_7O_{16}$ composition is also a recognized yellow pigment having a priderite structure. Priderite is a member of hollandite family and may have tetragonal or monoclinic structure depending on the r_B/r_A ratio. The r_B/r_A ratio of 0.48 corresponds to (approximately) the tetragonal/ monoclinic boundary (at room temperature) where, r_B is the average of the radius of the Ni^{2+} and the Ti^{4+} ions and r_A is the radius of Ba^{2+} ion (Carter *et al.*, 2004). For $Ba_x(Ni_xTi_{8-x})O_{16}$ (with x = 1) composition, since the r_B/r_A value is less than 0.48 therefore, the greenish-yellow compound can be inferred to have a tetragonal structure.

As far as toxicity is concerned, both $Ti^{IV}(W^{VI}Ni^{II})O_2$ and $BaNiTi_7O_{16}$ are safe for the environment, as they are not composed of toxic elements and also because of their low solubility in water and dilute mineral acids.

The ceramic pigments with grain sizes in nanoscale are commercially potent in pigment industries, because of their high surface area which assures higher surface

coverage; higher number reflectance points and hence maximum scattering; and small particle size for uniform dispersion by homogenous mixing with the binders in paint formations, which enhances the mechanical strength of the paint after drying. When properly dispersed, the nanosized pigments exhibit superior effectiveness in critical abrasive and polishing applications also.

5.2 Reported Methods for the Preparation of $Ni_{0.1}W_{0.1}Ti_{0.8}O_2$ and $BaNiTi_7O_{16}$

The common routes for the preparation of $Ni_{0.1}W_{0.1}Ti_{0.8}O_2$ and $BaNiTi_7O_{16}$ colored titanates are through conventional solid-state method, which require high temperatures and repeated mixing/grinding of raw materials (such as, NiO, WO_3 And TiO_2; alternatively, species that yield metal oxides upon heat treatment, such as metal carbonates) and produces coarse particles. Some of the reported method for the preparation of $Ni_{0.1}W_{0.1}Ti_{0.8}O_2$ and $BaNiTi_7O_{16}$ are summarized below.

5.2.1 Conventional Solid-State Methods

Matteucci *et al.* (2006) have reported a procedure for the synthesis of $Ni_xW_xTi_{1-2x}O_2$ with rutile phase by conventional solid-state method, which involves wet mixing of raw materials (such as, anatase (Degussa DT51), NiO and WO_3) in porcelain jar by grinding in alumina media, drying in oven at 105 ºC followed by calcination in alumina crucibles in an electric kiln at 1100 ºC, with heating rate of 200 ºC/h, soaking time of 1 h and cooling to room temperature.

Maloney (2002) has given a general synthesis procedure for the preparation of $BaNiTi_7O_{16}$ using raw materials such as, $BaCO_3$, basic nickel carbonate, and TiO_2 thorugh a high temperature solid-state reaction. Sometimes the final product is observed to be contaminated by the formation of secondary phases such as, $BaTiO_3$, $BaTi_2O_5$, $BaTi_4O_9$. These are the very common disadvantages associated with solid-state reactions.

5.2.2 Chemical Method

Reports on the chemical synthesis of $Ni_xTi_{1-2x}W_xO_2$ and $BaNiTi_7O_{16}$ have not been found in literature so far. Therefore, the chemical methods for the syntheses of $Ni_xTi_{1-2x}W_xO_2$ and $BaNiTi_7O_{16}$ powders can be established, which is a less cumbersome and low temperature method for the large scale preparations. The advantages associated with the chemical methods are the better control of homogeneity and stoichiometry in the final product at the molecular level.

5.3 Scope of the Present Investigation

The present study describes the aqueous based chemical synthesis of nanocrystalline powders of $Ni_xTi_{1-2x}W_xO_2$ and $BaNiTi_7O_{16}$ through metal ion-ligand complex based precursor route using dimethyl ammonium tungstate and titanium oxalate as innovative and stable water-soluble sources of tungsten and titanium respectively. In the developed process, the aqueous based metal ion-ligand complex precursor solutions are obtained by mixing aqueous solution of nickel nitrate, dimethyl ammonium tungstate and titanium oxalate with triethanolamine (TEA) in the required amounts. The precursor solutions are then pyrolyzed to voluminous carbonaceous mass through oxidative decomposition of the metalo-organic complexes. These solid precursors are calcined at respective calcination temperature to obtain the nanocrystalline powders of $Ni_xTi_{1-2x}W_xO_2$ and $BaNiTi_7O_{16}$.

In the present study, the structural and colorimetric properties of the prepared nanocrystalline powders of $Ni_xTi_{1-2x}W_xO_2$ and $BaNiTi_7O_{16}$ have been investigated.

5.4 Synthesis of Nanocrystalline Powders of $Ni_{0.1}W_{0.1}Ti_{0.8}O_2$ and $BaNiTi_7O_{16}$

5.4.1 The Raw Materials Used in the Preparation of Nanocrystalline Powders of $Ni_{0.1}W_{0.1}Ti_{0.8}O_2$ and $BaNiTi_7O_{16}$

5.4.1.1 The Raw Materials Used in the Preparation of Nanocrystalline Powders of $Ni_{0.1}W_{0.1}Ti_{0.8}O_2$

i) Nickel nitrate hexahydrate (Merck India Lt), ii) Sodium tungstate (Merck India Lt), iii) Titanium (IV) oxide (Merck India Lt), iv) Oxalic acid dihydrate (Merck India Lt), v) Triethanolamine (TEA) (Merck India Lt), vi) di-Ammonium oxalate monohydrate (Merck India Lt), vii) HCl (35%) (Merck India Lt), viii) HNO_3 (70%) (Merck India Lt.), ix) Ammonia (25%) (Merck India Lt.), ix) Dimethyl amine (40%) (Merck India Lt.), x) HF (40%) (Merck India Lt.).

5.4.1.2 The Raw Materials Used in the Preparation of Nanocrystalline Powders of $BaNiTi_7O_{16}$

i) Nickel nitrate hexahydrate (Merck India Lt), ii) Barium nitrate (Merck India Lt), iii) Titanium (IV) oxide (Merck India Lt), iv) Oxalic acid dihydrate (Merck India Lt), v) Triethanolamine (TEA) (Merck India Lt), vi) di-Ammonium oxalate monohydrate (Merck India Lt), vii) HNO_3 (70%) (Merck India Lt.), viii) Ammonia (25%) (Merck India Lt.). ix) HF (40%) (Merck India Lt.).

In this study, aqueous solution of dimethylammonium tungstate and titanium oxalate were prepared in the laboratory and stocked for use as source of tungsten and titanium in the synthesis process.

5.4.1.3 Preparation of Aqueous Solution Dimethylammonium Tungstate

Weighed amount of sodium tungstate was dissolved in deionized water and then acidified by drop wise addition of dilute hydrochloric acid (>5 N) to obtain a yellow precipitate of insoluble tungstic acid. The precipitate was filtered and after washing

with deionized water to remove the chloride ions it was dissolved in minimum volumes of dimethylamine (40% solution) and finally the resultant solution was diluted to required volume with deionized water to obtain the stock of solution of dimethylammonium tungstate. The tungsten-content in the solution was confirmed by assay process. The schematic representation of the preparative method is shown in Figure 5.1.

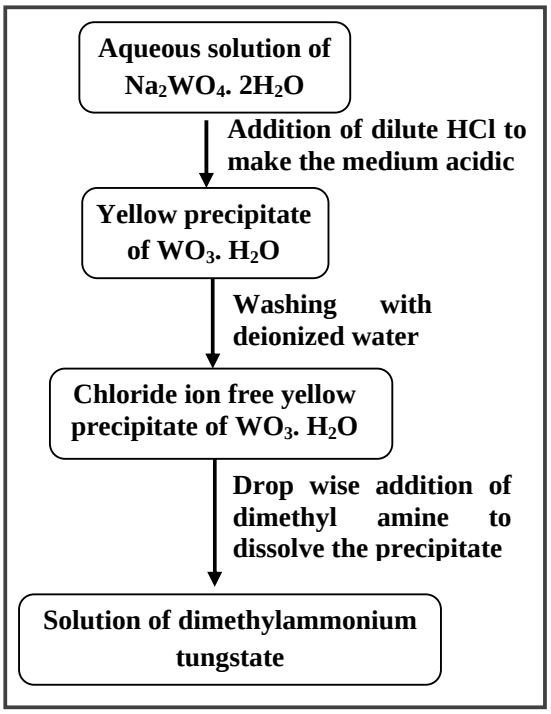

Figure 5.1: *Schematic representation of the preparation of the aqueous solution of dimethylammonium tungstate.*

5.4.1.4 Preparation of Aqueous Solution of Titanium oxalate

Aqueous solution of titanium oxalate was prepared starting from its hydrous oxide [TiO_2. nH_2O]. To begin with, weighed amounts of titanium oxide (TiO_2) (1 M >99%) was dissolved in HF (>7 M) by heating the mixture over a water bath for 28-30 h to obtain a clear solution of the titanium-fluoride complex [TiF_6^{2-}]. Hydrous titanium oxide was then precipitated out from this clear solution by drop wise addition of dilute ammonia, and washed with 5% ammonia to make it free from fluoride ions. The

precipitate was then slowly dissolved in an aqueous mixture of oxalic acid (0.1 M) and ammonium oxalate (0.1 M) with constant stirring to obtain a clear solution, which was diluted to required volume with deionized water to get the stock solution of titanium oxalate. The aqueous mixture of oxalic acid and di-ammonium oxalate (3:1 mole ratio) used for the dissolution was freshly prepared and always used in excess to stoichiometric requirement of two moles per mole of Ti(IV) ion. The titanium content in the solution was estimated by the assay method. The synthetic method has been schematically given in Figure 5.2.

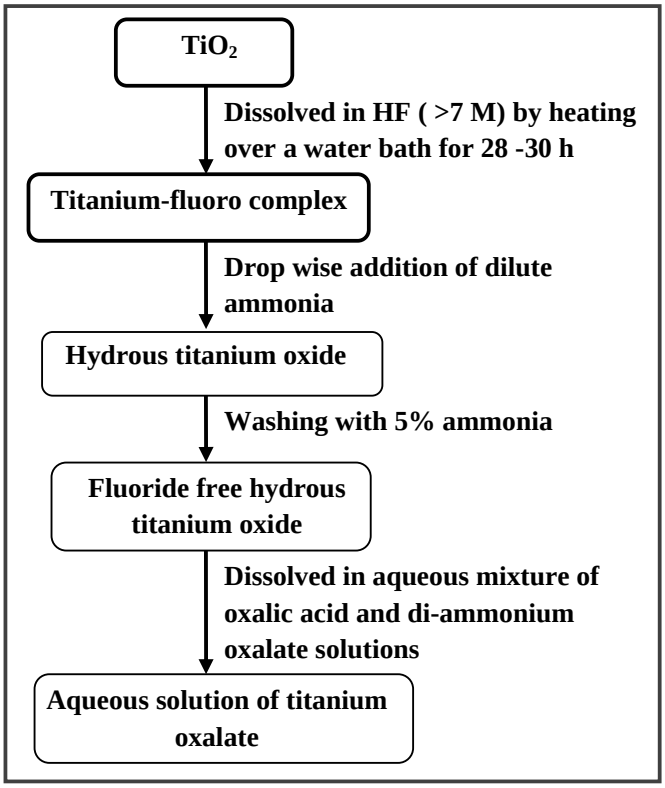

Figure 5.2: *Schematic representation of the preparation of the aqueous solution of titanium oxalate.*

5.4.2.1 Synthesis Procedure of Nanocrystalline $Ni_{0.1}W_{0.1}Ti_{0.8}O_2$ Powders

For the preparation of $Ni_{0.1}W_{0.1}Ti_{0.8}O_2$ solid solution, stoichiometric amount of aqueous solution of nickel nitrate (0.1 M) was taken from a freshly prepared stock,

added into the mixture of stoichiometric amount of aqueous solutions of titanium oxalate and dimethylammonium tungstate taken from their respective stocks and mixed up with constant stirring. TEA was then added into the solution mixture to keep the metal ions in solution through complexation and the pH of the solution was adjusted to ~5 with the help of nitric acid to avoid precipitation. The amount of TEA was always added in excess to the total cations present in the solution mixture (i.e., ~4 moles with respect to the total moles of the metal ions). The resultant precursor solution was homogenized by constant stirring and finally set to dehydrate by heating at ~200 °C. On complete evaporation of the precursor solution, the TEA and the metal-complexes decomposed with the evolution of dense fumes and resulted in a voluminous, fluffy, black organic-based mass. The fluffy carbonaceous mass was crushed to obtain the fine precursor powders, which were calcined for 2 h in alumina crucible (at a heating rate of 5 ^oC/min) in ambient atmosphere with temperatures varying from 450-800 ^oC to obtain pure rutile phased solid solution. The synthetic method has been schematically shown in Figure 5.3.

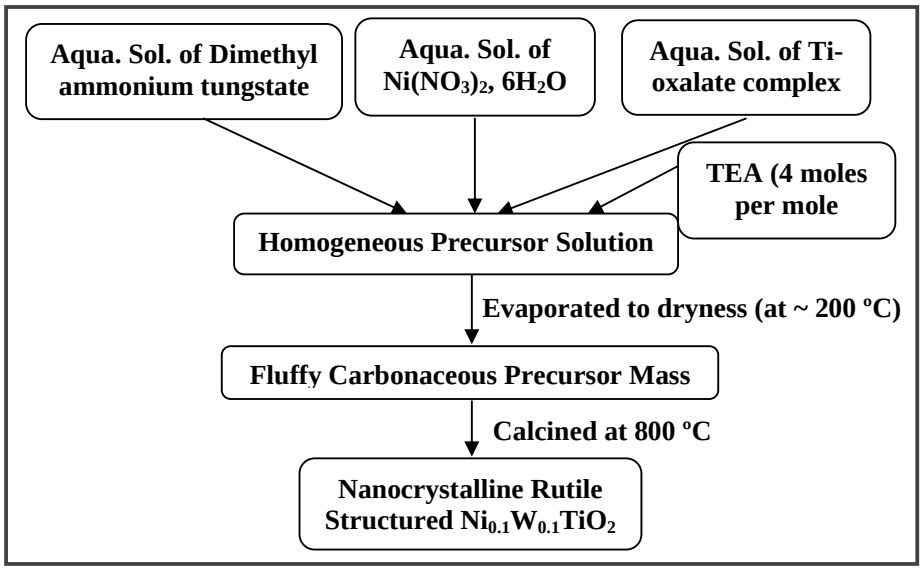

Figure 5.3: *Schematic representation of the preparation of the nanocrystalline powders of* $Ni_{0.1}W_{0.1}Ti_{0.8}O_2$

5.4.2.2 Synthesis Procedure of Nanocrystalline Powders of $BaNiTi_7O_{16}$

For the preparation of $BaNiTi_7O_{16}$ composition, stoichiometric amount of aqueous solution of nickel nitrate (0.1 M) was taken from a freshly prepared stock and added into the mixture of stoichiometric amount of aqueous solutions of titanium oxalate taken from stock. Stoichiometric amount of barium nitrate was complexed with equal mole of ethylene diamine tetra-acetic acid (EDTA) separately with the help of few drops of ammonia. The EDTA-complexed solution was then added to the mixture of nickel nitrate and titanium oxalate solution. The TEA (~4 moles with respect to the total moles of the metal ions) was added in the solution mixture. The resultant precursor solution was homogenized by constant stirring and finally evaporated by heating at ~200 °C. On complete evaporation of the precursor solution, the TEA and the metal-complexes decomposed with the evolution of dense fumes and resulted in a voluminous, black, fluffy, mass. The fluffy carbonaceous mass was crushed to obtain the fine precursor powder, which was calcined for 2 h in alumina crucible (at a heating rate of 5 ^oC/min) in air with temperatures varying from 450-850 ^oC to obtain the priderite phased oxide. The synthetic method has been schematically shown in Figure 5.4.

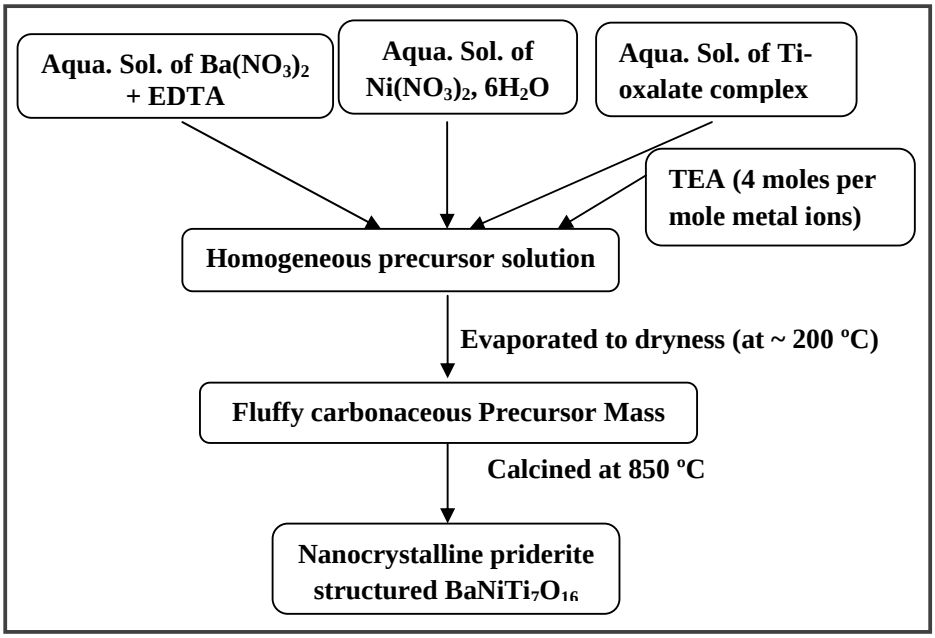

Figure 5.4: *Schematic representation of the synthesis of the nanocrystalline powders of $BaNiTi_7O_{16}$.*

5.5 Techniques for Characterization of the Prepared Nanocrystalline $Ni_{0.1}W_{0.1}Ti_{0.8}O_2$ and $BaNiTi_7O_{16}$ Powders

The phase identification in the synthesized $Ni_{0.1}W_{0.1}Ti_{0.8}O_2$ and $BaNiTi_7O_{16}$ powders was performed using room temperature XRD with CuK_α radiation and Ni filter. In the XRD studies, the powders obtained at different heat treatment temperatures were recorded in the 2θ range from 20˚ to 70˚ for rutile phase and from 15˚ to 70˚ for priderite phase. The crystallite size of both the compositions was calculated using Scherrers equation. The fraction of rutile phase was calculated from the relative intensities of the XRD peaks corresponding to the anatase and the rutile phases in the $Ni_{0.1}W_{0.1}Ti_{0.8}O_2$ composition at various heat-treated temperatures using the Spurr equation (Spurr *et al.*, 1957):

$$F_R = \frac{1}{1+1.26\frac{I_A(101)}{I_R(110)}}$$

where, F_R is the mass fraction of rutile phase in the samples and I_A (101) and I_R (110) are the intensities of d_{101} and d_{110} lines of the anatase and rutile phase respectively. Simultaneously recorded thermogravimetric and differential thermal analysis (TG/ DTA) of the precursor powders were carried out in air at a heating rate of 5 °C/min. UV-visible-NIR spectroscopy studies for the calcined powders were carried out in Ocean Optics SD 2000. The high-resolution transmission electron microscopy (HRTEM) measurements were carried out. Particle size distributions of both the samples were determined by using the UTHSCSA Image Tool program (version 3.00) using three TEM images each containing ~50 particles. The BET specific surface areas of the calcined powders were determined. The color of the pigments was assessed from *CIEL*a*b** color parameter measurements, calculated from the diffuse reflectance spectra taken with a Perkin-Elmer colorimeter using a standard illuminant D. According to the method the parameter *L** represents the brightness of a sample; *L** is a lightness axis [black (0) to white (100)]; *a** represents the green (−) → red (+) axis and *b** the blue (−) → yellow (+) axis. For XRD, TEM, thermal studies and BET

surface area measurements of the synthesized nanocrystalline $Ni_{0.1}W_{0.1}Ti_{0.8}O_2$ and $BaNiTi_7O_{16}$ powders, the instruments which have been specified in the chapter 2, Section 2.5 were used.

5.6 Results and Discussion

5.6.1 Thermal Studies of the Nanocrystalline $Ni_{0.1}W_{0.1}Ti_{0.8}O_2$ and $BaNiTi_7O_{16}$ Precursors

Thermogravimetric (TG) and differential thermal analysis (DTA) of the carbonaceous precursor powders for the composition $Ni_{0.1}W_{0.1}Ti_{0.8}O_2$ were carried out in aerial atmosphere. Figure 5.5a shows the TGA and DTA curves for the carbonaceous precursor powders of the $Ni_{0.1}W_{0.1}Ti_{0.8}O_2$ composition. The TGA curve clearly showed 8% weight loss of up to 200 °C, and a rapid weight loss of ~ 90% between 200 °C and 570 °C. Beyond 570 °C the TGA curve remained constant and showed no further weight loss up to 950 °C. The first weight loss step up to 200 °C in TGA possibly corresponded to the vaporization of absorbed water. The second sharp weight loss between 200 °C and 570 °C in TGA was manifested by four exothermic peaks in the DTA curve in the corresponding temperature range. This exothermic thermal effect could be assigned to the oxidation of the carbonaceous precursors that probably retained some un-decomposed fraction of metal-complexes, nitrates and TEA even after the dehydration process. The accompanying weight loss in the TGA curve could be attributed to the evolution of gases (such as, water vapor, and oxides of carbon and nitrogen) due to decomposition/oxidation of the un-decompose fractions along with that of the carbon retained in the precursor. Emergence of a broad exothermic peak beyond 600 °C in the DTA curve, with no weight loss manifestation in the TG curve in the corresponding region, could be attributed to the gradual transformation of the anatase phase to the rutile form in the oxide solid solution.

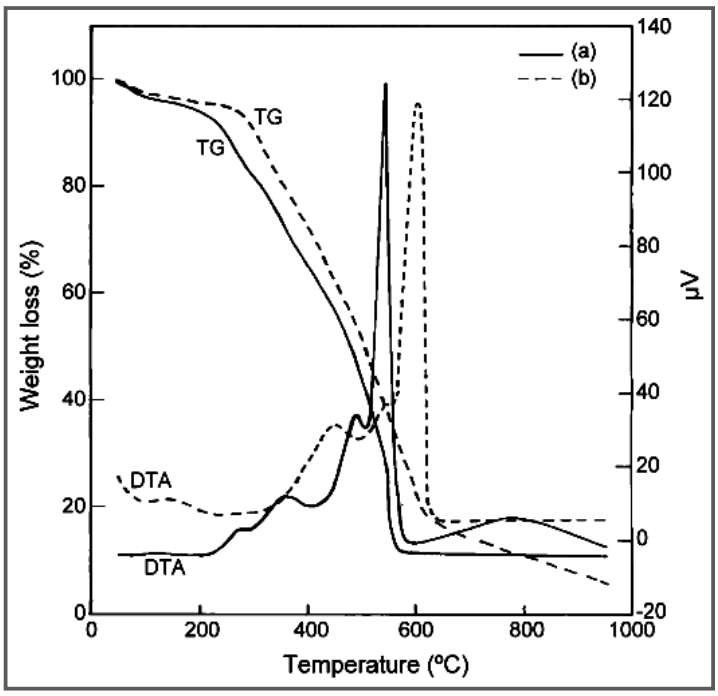

Figure 5.5: *Simultaneously recorded TGA and DTA plots of the carbonaceous precursors of solid solution composition: (a) $Ni_{0.1}W_{0.1}Ti_{0.8}O_2$, (b) $BaNiTi_7O_{16}$.*

Thermogravimetric (TG) and differential thermal analysis (DTA) of the carbonaceous precursor powders for the composition $BaNiTi_7O_{16}$ were also carried out in aerial atmosphere. It can be seen from Figure 5.5b that TGA and DTA curves for the $BaNiTi_7O_{16}$ precursors were found to be similar to that of the $Ni_{0.1}W_{0.1}Ti_{0.8}O_2$ precursors and no significant difference was observed in the thermal behavior of the two precursors. The thermal decomposition of the $BaNiTi_7O_{16}$ precursors also reflected weight loss in the TG curve with simultaneous exothermic thermal effect in the DTA curve up to the ~600 ºC due to oxidation of the un-burnt carbonaceous mass and un-decomposed metal-complexes, nitrates and TEA retained in the precursors after complete evaporation of precursor solution of $Ba(NO_3)_2$, $Ni(NO_3)_2$, titanium oxalate and TEA. There was no exothermic effect or, weight loss observed beyond 600 °C signifying that the heat generated during the oxidation of the carbonaceous precursor between 350 and 600 ºC was sufficient for direct crystallization of the pure priderite phase from the amorphous precursors.

5.6.2 Composition, Phase and Structural Analysis of the Nanocrystalline $Ni_{0.1}W_{0.1}Ti_{0.8}O_2$ and $BaNiTi_7O_{16}$ Powders

Phase analysis and structural characterization of the prepared $Ni_{0.1}W_{0.1}Ti_{0.8}O_2$ powders were carried out through room temperature X-ray powder diffraction (XRD) studies. Figure 5.6 shows the characteristic XRD patterns for the $Ni_{0.1}W_{0.1}Ti_{0.8}O_2$ precursor powder, when heat-treated at various temperatures between 450 ^oC to 800 ^oC for 2 h. The virgin precursors were amorphous to X-ray and the crystallization of the oxide phase began at temperatures higher than 450 °C, which was reflected by the emergence of broad, low-intensity diffraction lines. Up to 550 °C the precursor powder contained gray tint indicating the presence of residual carbon. When heat-treated at 600 °C and above, the powder appeared yellow in color, which indicated the complete burnout of residual carbon from the precursor powders. Increase in the heat-treatment temperatures up to 650 °C resulted only anatase phase in the solid solution indicated by the appearance of d_{101} diffraction line. Beyond 650 °C, the d_{110} plane of rutile began to appear and at 800 °C pure rutile phase was formed.

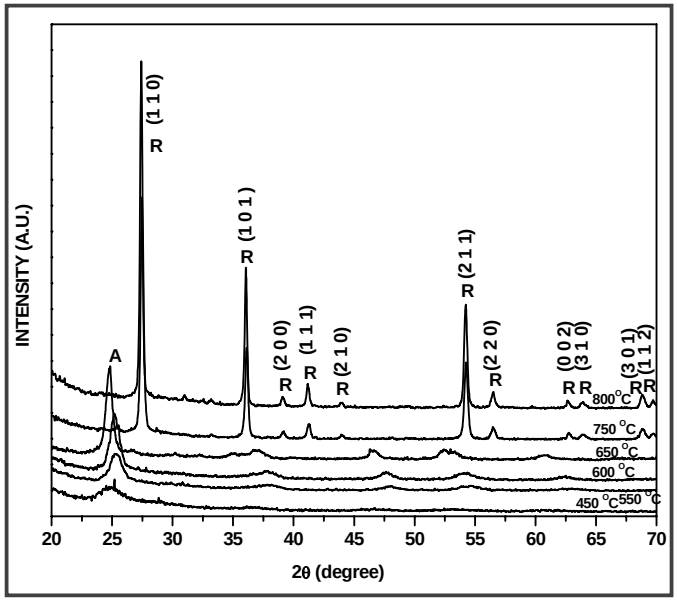

Figure 5.6: *X-ray diffractograms (using CuK_α radiation) of $Ni_{0.1}W_{0.1}Ti_{0.8}O_2$ precursor on calcination at various temperatures.*

Thermodynamically rutile phase of titanium dioxide is stable over anatase phase. Therefore, the rutile phase is desirable for pigment formation. In addition to this the photocatalytic efficiency of rutile phase is also diminished. Gradual increase of calcination temperature resulted the crystal growth and increase in the rutile fraction in the samples, which was evident by gradual sharpening of the d_{110} diffraction line of rutile phase with gradual increase its intensity and simultaneous diminishing of the d_{101} diffraction line of anatase phase from X-ray diffractogram. On heat-treatment of the precursors at 750 °C for 2 h, the percentage of the rutile phase in $Ni_{0.1}W_{0.1}Ti_{0.8}O_2$ was found to be around 95%, and the pure rutile phase was obtained at 800 ^oC for 2 h (Table 5.1). The XRD peaks for the solid solution composition were indexed using the standard data available for the rutile phase (JCPDS card no. 781510). The lattice parameters (i.e., a and c) for the rutile phase $Ni_{0.1}W_{0.1}Ti_{0.8}O_2$ solid solution, heat-treated at (800 ^oC for 2 h) were calculated following the reflection planes (200) and (002) and their values: $a = b = 4.602$ Å and $c = 2.962$ Å; the cell volume 62.74 $Å^3$. The calculated values of a and c were found to be in close agreement with those reported for the standard rutile phased TiO_2 (JCPDS data card no.781510). As there was no evidence of any additional phase in the samples at heat–treatment temperature 800 ^oC for 2 h, and also because the unit-cell parameters fairly matched with the chemical composition, therefore the structure of $Ni_{0.1}W_{0.1}Ti_{0.8}O_2$ solid solution (at heat treatment temperature 800 ^oC) was confirmed to be of purely rutile type.

Table 5.1: *Percentage of rutile phase, and tap densities of the $Ni_{0.1}W_{0.1}Ti_{0.8}O_2$ composition at different calcinations temperatures*

Calcination temperature	Rutile phase (%) for compositions	XRD intensities of the A and R phases for compositions*	Tap[1] densities (g/cc)
600 ºC for 2 h	4.0	A (s), R(w)	0.1367
650 ºC for 2 h	12.0	A(s), R(w)	0.1732
750 ºC for 2 h	95.0	R(s), A(vw)	0.1855
800 ºC for 2 h	100.0	R (s)	0.2387

* Relative XRD Intensities of the Anatase (A) and Rutile (R) Phases; s = strong, w = weak, mw = medium weak, vw= very weak

Phase analysis and structural characterization of the prepared $BaNiTi_7O_{16}$ powders were carried out through room temperature XRD studies. Figure 5.7 shows the characteristic XRD patterns for the $BaNiTi_7O_{16}$ precursor powder at various heat-treatment temperatures between 600 ^oC to 850 ^oC for 2 h. The virgin precursors were amorphous to X-ray below 600 °C and initiation of phase formation of this titanate was found from XRD of the powder at 600 °C. The greenish yellow colored, pure priderite phase with the tetragonal structure of the compound was realized at 850 °C. The XRD peaks for this solid solution were indexed using the standard data available for the priderite phase (JCPDS card no. 741452). The calculated lattice parameters

[1] For the measurement of tap densities of the prepared powders, known amounts of the powders were taken and packed in a graduated cylindrical glass tube under gravity by tapping over a rubber pad for a fixed interval of time until the level of the powder in the tube became almost a constant. The volumes of the compacted powders were then measured and the densities were calculated thereby.

The tap densities were observed to increase with increasing calcination temperature probably because of decrease in the porosity in the material and gradual sintering of the particles. Moreover, trace amounts of free carbon might have been retained in the samples at lower heat-treatment temperatures which would contribute to a lower mass to volume ratios for the samples and hence to lower densities.

(i.e., *a* and *c*) for the $BaNiTi_7O_{16}$ composition, heat-treated at (850 ^oC for 2 h) following the reflection planes (200) and (002) were $a = b = 10.074$ Å and $c = 2.958$ Å, the cell volume 300.19 $Å^3$. The values of *a* and *c* were found to be in close agreement with those reported for the standard priderite structure (JCPDS data card no. 741452). At heat treatment temperature 850 ^oC for 2 h, $BaNiTi_7O_{16}$ was therefore confirmed to be of purely priderite type because of no evidence of any additional phase in the samples, and also the unit-cell parameters matched with the reported data for priderite structure.

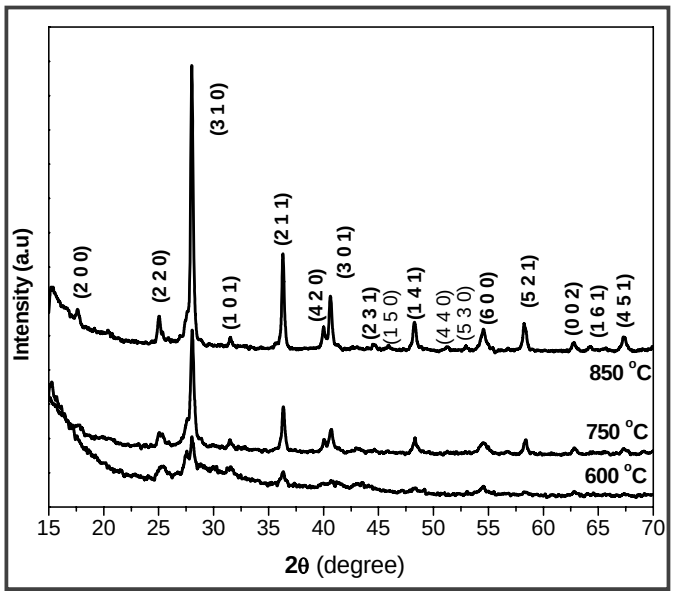

Figure 5.7: *X-ray diffractograms (using CuK_α radiation) of $BaNiTi_7O_{16}$ precursor on calcination at various temperatures.*

The calculated crystallite size obtained from XRD studies for both the oxides were found to be in the range of 25-30 nm. The EDX analysis of both samples also showed an acceptable chemical homogeneity, which in these cases were very close to the theoretical compositions formulated.

5.6.3 Morphology and Microstructural Studies of the Nanocrystalline $Ni_{0.1}W_{0.1}Ti_{0.8}O_2$ and $BaNiTi_7O_{16}$ Powders

Finer microstructural information of the calcined powders of $Ni_{0.1}W_{0.1}Ti_{0.8}O_2$ was obtained through transmission electron microscopy (TEM) study. Figure 5.8 shows a TEM image of $Ni_{0.1}W_{0.1}Ti_{0.8}O_2$ composition heat treated at 800 °C for 2 h. The smallest visible particles in the bright field electron micrograph can be identified as single crystallites and/or their aggregates in the figure. The average diameters of the smallest visible isolated particle/crystallite agglomerate were found to range between 30 and 60 nm. The bright field micrographs represented in Figure 5.8b and 5.8c depict two sections of Figure 5.8a taken at higher resolutions (at 40k and 100k respectively). Figure 5.8d represents a typical HRTEM image (with a resolution 800k) of the

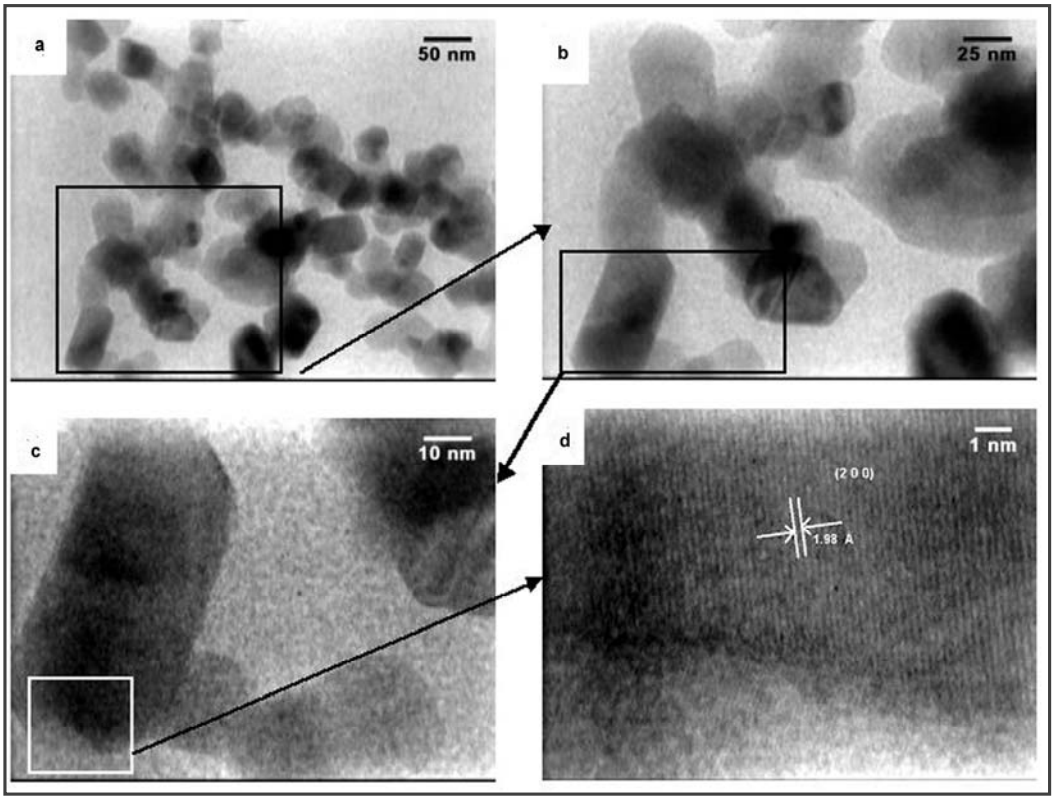

Figure-5.8(a), (b), and (c): *Bright field TEM micrograph of the calcined (800 ºC for 2 h) $Ni_{0.1}W_{0.1}Ti_{0.8}O_2$ solid solution.* **Figure-5.8(d):** *HRTEM image of the calcined (800ºC for 2 h) $Ni_{0.1}W_{0.1}Ti_{0.8}O_2$ solid solution.*

sample, depicting the lattice fringes in their crystal structure. From Figure 5.8d, the lattice spacing was found to be ~ 1.98 Å, which corresponded to the *(200)* plane in the rutile lattice when the crystals were oriented along the (200) plane. The selected-area electron diffraction (SAED) pattern of the samples is shown in Figure 5.9. The characteristics SAED pattern of the heat-treated (800 °C for 2 h) powder showed distinct rings corresponding to the *(101), (200), (220)* planes in a rutile lattice, thus inferring the powders to be rutile structured nanosized polycrystalline.

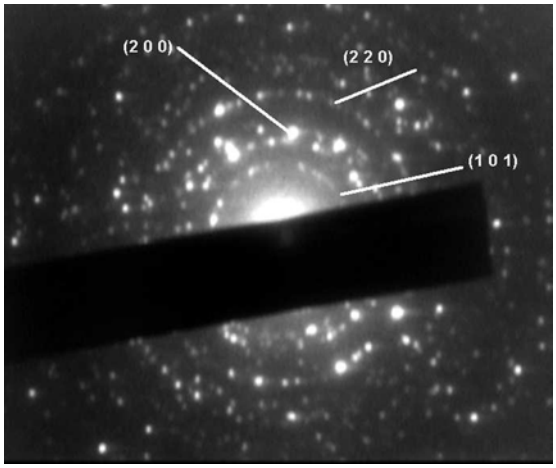

Figure-5.9: *SAED pattern of the calcined (800 ºC for 2 h) $Ni_{0.1}W_{0.1}Ti_{0.8}O_2$ showing distinct rings corresponding to the (1 0 1), (2 0 0), (2 2 0) planes in a rutile lattice.*

For obtaining microstructural information of the calcined powders of $BaNiTi_7O_{16}$, TEM study was carried out. Figure 5.10 shows a bright field TEM image of $BaNiTi_7O_{16}$ composition heat-treated of the respective precursors at 850 °C for 2 h. The particles were mostly spherical with average particle diameters ranging between of 25-45 nm with narrow particle size distribution. Characteristics selected-area electron diffraction (SAED) pattern of $BaNiTi_7O_{16}$ powder (heat-treated 850 ºC for 2 h) (Figure 5.11) showed the powders to be polycrystalline.

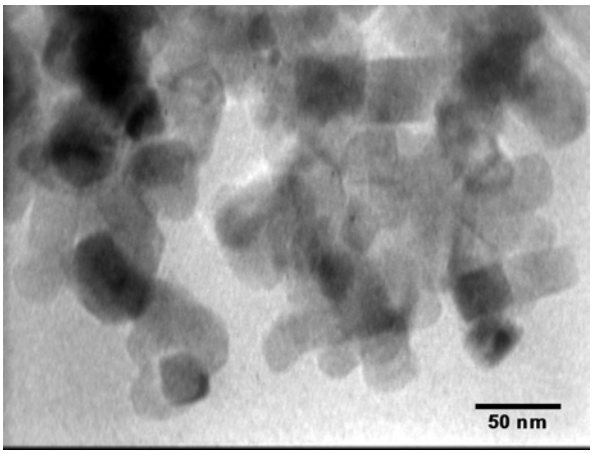

Figure 5.10: *Bright field TEM micrograph of the calcined (850 ºC for 2 h) $BaNiTi_7O_{16}$ composition.*

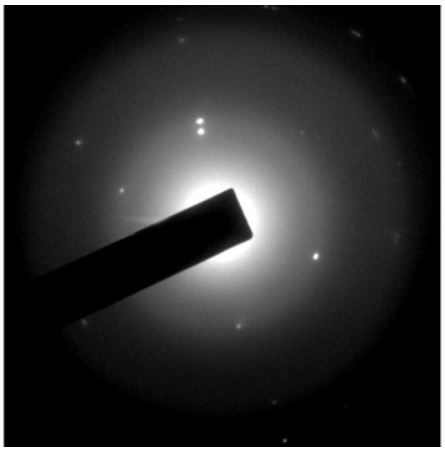

Figure 5.11: *SAED pattern of the calcined (850 ºC for 2 h) $BaNiTi_7O_{16}$ with a priderite structure.*

The BET surface area of both the compositions has been found to be high and they are in the range of 100-120 m^2g^{-1}. The tap densities of the $Ni_{0.1}W_{0.1}Ti_{0.8}O_2$ composition were found to increases with the increase in heat treatment temperatures of the precursor powders and the corresponding values are summarized in Table 5.1.

5.6.4 UV-visible Spectroscopy Studies and Color Measurements of the Nanocrystalline $Ni_{0.1}W_{0.1}Ti_{0.8}O_2$ and $BaNiTi_7O_{16}$ Powders

The UV-visible-NIR absorption spectra for the calcined $Ni_{0.1}W_{0.1}Ti_{0.8}O_2$ (at 800 ºC for 2 h) and $BaNiTi_7O_{16}$ (at 850 ºC for 2 h) compositions are shown in Figure 5.12 and Figure 5.13 respectively. Both the samples showed three distinct absorption bands between 250 and 1200 nm corresponding to the three spin allowed *d-d* transitions from the Ni^{2+} ions in octahedral environment. For the $Ni_{0.1}W_{0.1}Ti_{0.8}O_2$ composition, the three distinct humps are positioned in the ranges: 350–570 nm, 600–950 nm, and 970-1100 nm. These bands were assigned as: $^3A_{2g}(F) \rightarrow {}^3T_{1g}(P)$ (350–570 nm), $^3A_{2g}(F) \rightarrow {}^3T_{1g}(F)$ (600–950 nm) and $^3A_{2g}(F) \rightarrow {}^3T_{2g}(F)$ (970-1100 nm) (Lever, 1968). Similarly, the three spin allowed *d-d* transitions for the $BaNiTi_7O_{16}$ composition are

assigned as: $^3A_{2g}(F) \rightarrow {}^3T_{1g}(P)$ (275–550 nm), $^3A_{2g}(F) \rightarrow {}^3T_{1g}(F)$ (570–950 nm) and $^3A_{2g}(F) \rightarrow {}^3T_{2g}(F)$ (950--1100 nm) (Lever, 1968). For both the compositions the energies of the last two electronic spin allowed transitions exist in the visible light energy range and hence they contribute towards the color of the samples while the first transition lies is in the ultraviolet range and therefore does not affect the color of the samples. Besides these three spin allowed *d-d* transitions from the Ni(II) ion in octahedral environment there may be additional absorption bands in both the compositions (i.e., $Ni_{0.1}W_{0.1}Ti_{0.8}O_2$ and $BaNiTi_7O_{16}$) owing to charge transfers between the constituent metal ions [Ni(II), Ti(IV), W(VI)], and between ligand and metal ions. The absorption bands due to $Ti^{4+} \leftrightarrow O^{2-}$ charge transfer in undoped rutile are very close to the absorption bands corresponding to $^3A_{2g}(F) \rightarrow {}^3T_{1g}(P)$ transitions in the solid solution compositions. The absorption bands corresponding to metal-metal and metal-ligand charge transfers are therefore difficult to distinguish in either of the solid solution compositions as they are expected to overlap with the spin allowed *d-d* transitions of the Ni^{2+} in the UV-visible spectral range. The color of the rutile phased titanate pigments are generally attributed to crystal field transitions (Eppler, 1987) along with some contribution from the Ti–O metal–ligand charge transfer (MLCT), the band gap (Maloney, 2002) or, defects in crystals created by the varying sizes of the constituent metal ions (e.g. chromophores and counterions) (Dondi *et al.*, 2006)

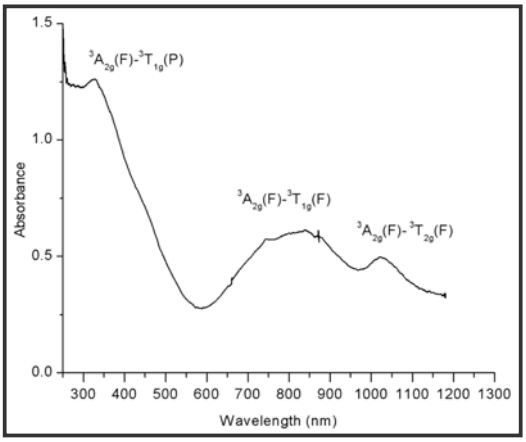

Figure 5.12: *UV-visible-NIR absorption spectra for calcined (at 800 ºC for 2 h) powder of the $Ni_{0.1}W_{0.1}Ti_{0.8}O_2$ solid solution.*

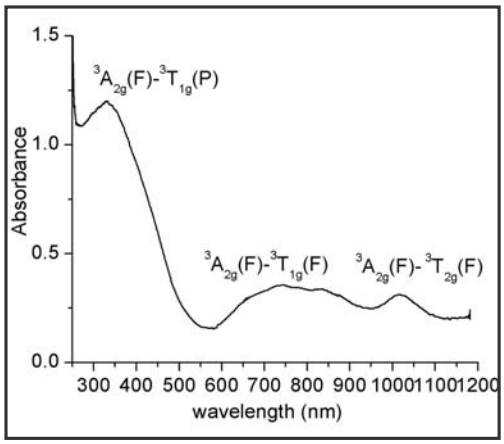

Figure 5.13: *UV-visible-NIR absorption spectra for calcined (at 850 ºC for 2 h) powder of the $BaNiTi_7O_{16}$.*

The *CIE-L*a*b** measurements of $Ni_{0.1}W_{0.1}Ti_{0.8}O_2$ and $BaNiTi_7O_{16}$ compositions heat treated at their calcination temperatures summarized in Table 5.2 represent a yellow color of both the samples (i.e. high *b** and low *a** parameters) and a light color (*L** by ~83-91) in agreement to the UV-Visible-NIR spectra of the samples. The $BaNiTi_7O_{16}$ composition showed higher *b** but lower *a** parameter (more yellow intensity but with greenish shades) and lightness while $Ni_{0.1}W_{0.1}Ti_{0.8}O_2$ had some reddish shade. *CIE-L*a*b** colorimetric parameters for both the samples after heat treatment at 1250 ºC for 1 h are also given in Table 5.2. Both the samples exhibited slight decrease in *L** values indicating the decrease in lightness at 1250 ºC for 1 h. On the other hand increase in *b** values of two compositions represented the enhancement of yellow amount and decrease in a* value indicated the development of slight green amount in the solid oxides.

Table 5.2: *The colour parameters (CIE L*a*b*) for $Ni_{0.1}W_{0.1}Ti_{0.8}O_2$ and $BaNiTi_7O_{16}$ compositions at different temperatures.*

Pigment Composition	Temperature/ duration	*L**	*a**	*b**
$Ni_{0.1}W_{0.1}Ti_{0.8}O_2$	800 ºC for 2 h (phase formation temperature)	87	-5	58
	1250 ºC for 1 h	83	-6	62
$BaNiTi_7O_{16}$	850 ºC for 2 h (phase formation temperature)	91	-11	67
	1250 ºC for 1 h	89	-13	71

For studying the thermal stabilities of the compositions at high temperatures, the final powders were annealed at 1250 ºC for 1 h. The XRD studies of the powders revealed that the phases of the synthesized compositions remained unaltered even when subjected to heat treatment at the temperatures of 1250 ºC for 1 h, thereby establishing the thermal stabilities of the respective oxide compositions at high

temperatures. Furthermore, XRD phase analysis and color parameter measurements of the powders after being subjected to treatment with dilute HCl, dilute HNO_3 and dilute NaOH were found to remain unchanged reflecting the retention of their chemical composition and color even on post treatment thereby validating their chemical inertness under acidic and alkaline conditions.

5.7 Major Findings in the present Investigation

- Nanocrystalline rutile structured $Ni_{0.1}W_{0.1}Ti_{0.8}O_2$ and priderite structured $BaNiTi_7O_{16}$ yellow pigments have been prepared through pyrolysis of Metal ion-ligand complex based precursor solution.
- The preparation method established the use of dimethyl ammonium tungstate and titanium oxalate as respective stable water-soluble sources of tungsten and titanium.
- Pure rutile phase and priderite phase titanates were realized through heat-treatment of the precursor powders at 800 ^oC and 850 ^oC respectively.
- The UV-visible-NIR spectra for both oxides exhibited three absorption bands due to *d-d* transitions of *d*-electrons of Ni^{2+} ions.
- The measurement of the color parameters (*CIE L* a* b**) reflected an intense yellow color with greenish shades for the $BaNiTi_7O_{16}$ composition, while the $Ni_{0.1}W_{0.1}Ti_{0.8}O_2$ samples exhibited yellow coloration with reddish shades.

References

Badenes, J. A., Llusar, M., Tena, M. A., Calbo, J. and Monrós, G. (2002), Praseodymium-Doped Cubic Ca–ZrO_2 Ceramic Stain, Journal of the European Ceramic Society, Vol. 22, No. 12, pp. 1981-1990.

Bondioli, F., Manfredini, T. and Pellacani, G. C. (1999), Inorganic Pigments for Ceramic Tiles: Characteristics and Industrial Applications, Interceram, Vol. 48, No. 6, pp. 414–422. And, Italian Ceramic Society, Colour Pigments and Colouring in Ceramics, SALA, Modena, 2003, pp. 1–129.

Carter, M. L. (2004), Tetragonal to Monoclinic Phase Transformation at Room Temperature in $Ba_xFe_{2x}Ti_{8-2x}O_{16}$ Hollandite Due to Increased Ba Occupancy, Materials Research Bulletin, Vol. 39, No. 7-8, pp. 1075-1081.

Cornell, R. M. and Schwertmann, U. (1996), The Iron Oxides; Structure, Properties, Reactions, Occurrence and Uses, VCH, Verlagsgesellschast mbH, Weinheim, Germany.

Dondi, M., Cruciani, G., Guarini, G., Matteucci, F. and Raimondo, M. (2006), The Role of Counterions (Mo, Nb, Sb, W) in Cr-, Mn-, Ni- and V-Doped Rutile Ceramic Pigments: Part 2. Colour and Technological Properties, Ceramics International, Vol. 32, No. 4, pp. 393-405.

Eppler, R. A. (1987), Effect of Antimony Oxide on the Anatase-Rutile Transformation in Titanium Dioxide, Journal of the American Ceramic Society, Vol. 70, No. 4, pp. C64–C66.

Lever, A. B. P. (1968), Inorganic Electron Spectroscopy, Elsevier, Amsterdam.

Maloney, J. (2002), Titanate Pigments: Colored Rutile, Priderite, and Pseudobrookite Structured Pigments, In High Performance Pigments, Smith, H. M. (Editor), Wiley-VCH, Verlag-GmbH, Weinheim, Germany, pp.53-73.

Matteucci, F., Cruciani, G., Dondi, M. and Raimondo, M. (2006), The Role of Counterions (Mo, Nb, Sb, W) in Cr-, Mn-, Ni- and V-Doped Rutile Ceramic Pigments. Part 1. Crystal Structure and Phase Transformation, Ceramics International, Vol. 32, No. 4, pp. 385-392.

Sorlí, S., Tena, M. A., Badenes, J. A., Calbo, J., Llusar, M. and Monrós, G. (2004a), Structure and Color of $Ni_xA_{1-3x}B_{2x}O_2$ (A=Ti, Sn; B=Sb, Nb) Solid Solutions, Journal of the European Ceramic Society, Vol. 24, No. 8, pp. 2425-2432.

Sorlí, S., Tena, M. A., Badenes, J. A., Llusar, M. and Monrós, G. (2004b), Study of Nickel Precursors in (Ni,M,Ti)O_2 (M = Sb, Nb) Yellow Ceramic Pigments, British Ceramic Transactions, Vol. 103, No. 1, pp. 10-14.

Spurr, R.A. and Myers, H. (1957), Quantitative Analysis of Anatase-Rutile Mixtures with an X-Ray Diffractometer. Analytical Chemistry, Vol. 29, No. 5, pp. 760-762.

Chapter 6

Synthesis of Nanocrystalline Powders of $Cr_{2x}W_xTi_{1-3x}O_2$ (x = 0.05, 0.1, 0.15) for Pigment Applications

Chapter 6

Synthesis of Nanocrystalline Powders of $Cr_{2x}W_xTi_{1-3x}O_2$ (x = 0.05, 0.1, 0.15) for Pigment Applications

6.1 Introduction

Incorporation of chromophorous transition metal ions, having ionic radii similar to Ti^{4+} (0.605 Å), into the host rutile (TiO_2) lattice normally generates oxide solid solutions with stable colorimetric properties. In formulations such as: $Ti^{IV}(A^{V(VI)}B^{II(III)})O_2$ (Huguenin *et al.*, 1998; Ramos *et al.*, 1991; Sorlí *et al.*, 2004a, 2004b; Tavala *et al.*, 1977; Tena *et al.*, 1994), the coloring effect is produced when the Ti (IV) ion, which is surrounded by six neighboring oxygen atoms at the corners of a regular (but slightly distorted) octahedron in the rutile lattice, is substituted by transition metal ions of lower valency at the 'B' site (e.g., B = Cr^{3+}; ionic radius = 0.615 Å) while the higher valency ions at the 'A' site (e.g., A = W^{6+}; ionic radius = 0.60 Å) compensate for the charge off set, such that their molar ratios ensure an overall electroneutrality in the oxide solid solutions.

The patent literature review shows that the development of such doped rutile pigments started at least 1934 only for their application in coloration of ceramic ware. Hund (1962), in his patent, has demonstrated three fundamental rules for the formulation of doped rutile solid solutions with many such compounds. These three fundamental rules are:

1. Substitutional atoms must have ionic sizes similar to Ti^{4+}.
2. Charge balance (electroneutrality) in the compounds should be maintained, and
3. The cation: anion ratio should remain at 1:2, as in TiO_2.

In recent years, chromium (III) doped rutile phased titanium dioxide solid solutions have gained considerable recognition (Malati *et al.*, 1984; Swiler *et al.*,

1993) as durable, chemical resistant inorganic pigments with stability (Maloney, 2002) beyond 1000 ^oC. Doping titanium dioxide with Cr^{3+} ions greatly reduces its tendency to act as a photocatalyst (Herrmann *et al.*, 1984) making the oxides extremely resistant to chalking. Alfred *et al.* (2003) have studied the electronic properties of TiO_2 catalysts doped with different amounts of Cr_2O_3 and WO_3 and discussed the structural defects therein.

The ceramic pigments with grain sizes in nanoscale can serve as potent pigments, because of their high surface area which assures higher surface coverage. Moreover, small sizes of the pigment particles facilitate their uniform dispersion and homogenous mixing with the binders in paint formulations, which in turn enhance the mechanical strength of the coating after drying of the paint.

6.2 Reported Methods for the Preparation of $Cr_{2x}W_xTi_{1-3x}O_2$

The preparation of rutile structured solid solutions doped with Cr^{3+} along with a counterion such as, Nb^{5+}, Sb^{5+}, or W^{6+} have mainly been reported through solid-state reactions, which require several processing steps such as, initial ball milling of the raw materials (usually metal oxides and/or carbonates) for homogenization; calcinations of these mixtures at high temperature (1100-1200 ºC) to obtain the desired crystalline phases and colors; and finally, wet milling to the reduce particle size. The solid-state method usually results in coarse-grained and agglomerated particles which are detrimental for the quality of the colored pigments. The preparations of such rutile structured titanium dioxide based solid solutions are summarized below.

6.2.1 Conventional Solid-State Methods

Tavala *et al.* (1977) have reported the preparation of the oxide systems such as, Cr_2O_3-TiO_2-WO_3 through solid-state method which involves mixing of raw materials such as Cr_2O_3, TiO_2 and WO_3 in required amount followed by calcination at 1100 ºC.

Recently, Matteucci *et al.* (2006) have also reported the preparation of rutile pigments doped with chromium and tungsten through solid-state reaction using the oxides raw materials such as, anatase (Degussa DT51), Cr_2O_3, and WO_3. The synthesis method involves wet mixing of raw materials in porcelain jar with alumina grinding media, drying in oven at 105 ºC followed by calcination in alumina crucibles in an electric kiln at 1100 ºC, with thermal rate of 200 ºC/h, soaking time of 1 h and then cooling to room temperature.

6.2.2 Chemical Method

Chemical synthesis of such doped rutile pigments has rarely been found to be reported in literature. Coprecipitation techniques are reported that they are not suitable for the synthesis of such doped rutile complex solid solutions (such as: $Cr_{2x}W_xTi_{1-3x}O_2$), because they often require high processing temperature and fail to maintain the desired stoichiometry in the products. In the most coprecipitation reactions, the metal ions are precipitated sequentially, not simultaneously and thus an inhomogeneous mix is generated. Additionally, the coprecipitated batches seldom lower the reaction temperature by more than 100 ºC.

6.3 Scope of the Present Investigation

Solution based chemical methods of preparation of the oxide solid solutions in contrast, are attractive alternative to the conventional solid-state synthesis technique. They not only have the advantage of reduced processing steps but also ensure a precise control of composition and stoichiometry in multicomponent formulations, phase purity in the final product, and better control of particle size in the final powders through molecular level mixing of the starting compounds in a solution. Uniformly distributed particles (Richards, 1973) with average grain sizes less than 100 nm obtained through the solution-based methods. In spite of the said advantages, there have been only a few literature reports on the preparation of Cr(III) and W(VI) doped rutile based oxide solid solutions through aqueous solution based chemical

methods so far, because of the diverse solubilities of the constituent ions and also due to scarcity of water-soluble salts of titanium and easy hydrolysis of the available ones, which are costly also. In this paper we report the preparation of Cr(III) doped rutile based oxide solid solutions with compositions – $Cr_{2x}W_xTi_{1-3x}O_2$ (where x = 0.05, 0.10, 0.15) through low temperature thermolysis of precursors obtained through evaporation of aqueous based precursor solutions comprising of soluble complexes of the constituent metal ions and optimum amounts of triethanolamine (TEA). The use of a water-soluble complex of tungstate (i.e., dimethylammonium tungstate) as the source of tungstate ions, and the formation of water-soluble complexes of Ti(IV) and Cr(III) with TEA in solution helps to retain the constituent metal ions in the precursor solution and prevents their hydrolysis and segregation/precipitation during the processing. The method is simple, the processing temperature required is much lower than those reported in literature, and the final product consists of nanosized particles with relatively narrow distribution in sizes. The present method is better than a coprecipitation method because, the synthesis of multi-component complex-systems like Cr and W doped titanium oxides by simple coprecipitation method does not produce nanosized materials maintaining the stoichiometry in the products.

The present study describes the aqueous based chemical synthesis of nanocrystalline powders of $Cr_{2x}W_xTi_{1-3x}O_2$ (where x = 0.05, 0.10, 0.15) through metal ion-ligand complex based precursor route using dimethyl ammonium tungstate and titanium oxalate as innovative and stable water-soluble sources of tungsten and titanium respectively. Solution based this method produces pure and single phased nanocrystalline pigments maintaining the required stoichiometry at temperature lower compared to the conventional solid-state method (Maloney, 2002; Matteucci *et al.,* 2006; Sorlí *et al.*, 2004a). This chapter also describes the structural and colorimetric properties of these mixed metal oxide solid solutions.

6.4 Synthesis of Nanocrystalline Powders of $Cr_{2x}W_xTi_{1-3x}O_2$ (x = 0.05, 0.1, 0.15)

6.4.1 The Raw Materials Used In the Developed Synthesis Method

i) Ammonium dichromate (Merck India Ltd), ii) Sodium tungstate (Merck India Ltd), iii) Titanium (IV) oxide (Merck India Ltd), iv) Oxalic acid dihydrate (Merck India Ltd), v) Triethanolamine (Merck India Ltd), vi) Diammonium oxalate monohydrate (Merck India Ltd), vii) HCl (35%) (Merck India Ltd), viii) HNO_3 (70%) (Merck India Ltd), ix) Ammonia (25%) (Merck India Ltd), x) HF (48%) (Merck India Ltd).

In this study, dimethylammonium tungstate and titanium oxalate complex solutions were prepared as precursors of tungsten and titanium respectively in the laboratory and stored for the use in the synthesis.

6.4.1.1 Preparation of Aqueous Solution Dimethylammonium Tungstate

In the synthesis of nanocrystalline powders of $Cr_{2x}W_xTi_{1-3x}O_2$ (x = 0.05, 0.1, 0.15), the aqueous solution of dimethylammonium tungstate was prepared following the procedure described in the Chapter 5, Section 5.4.1.3.

6.4.1.2 Preparation of Aqueous Solution of Titanium Oxalate Complex

In the synthesis of nanocrystalline powders of $Cr_{2x}W_xTi_{1-3x}O_2$ (x = 0.05, 0.1, 0.15), the aqueous solution of titanium oxalate complex was prepared following the procedure described in the Chapter 5, Section 5.4.1.4.

6.4.2 Synthesis Procedure of Nanocrystalline Powders of $Cr_{2x}W_xTi_{1-3x}O_2$ (x = 0.05, 0.1, 0.15)

Cr(III) doped rutile based oxide solid solutions with compositions – $Cr_{2x}W_xTi_{1-3x}O_2$ (where x = 0.05, 0.1, 0.15) were prepared using freshly prepared aqueous stock

solutions of ammonium dichromate, dimethylammonium tungstate, titanium oxalate and triethanolamine (TEA). Required volume of the aqueous solution of ammonium dichromate (0.1 M) was first taken from a freshly prepared stock and heated in presence of ethanol and few drops of concentrated nitric acid to have the color of the solution changed from orange to bluish green, as Cr(VI) got reduced to Cr(III). Appropriate volumes of the aqueous solutions of titanium oxalate and dimethylammonium tungstate were then taken from their respective stocks as per the required stoichiometries and added to the bluish green solution of Cr(III) under constant stirring. Finally, optimum amount of TEA was added into the solution mixture to keep the metal ions in solution through complexation and the pH of the solution was adjusted to ~5 with the help of nitric acid to avoid precipitation. The amount of TEA was always kept in excess to the total cations present in the solution mixture (i.e., ~4 moles with respect to the total moles of the metal ions). The resultant precursor solution was homogenized by constant stirring and eventually set to evaporate by heating at ~200°C. On complete dehydration of the precursor solution, the TEA and the metal-complexes decomposed with the evolution of dense fumes and resulted in a voluminous, fluffy, black organic-based mass. The fluffy carbonaceous mass was crushed to obtain the fine precursor powders; the rutile structured solid solutions were eventually obtained through calcination of the fine powders for 2 h at temperatures ranging between 450 and 800^oC using alumina crucible, maintaining a heating rate of 10^oC/min in ambient atmosphere. Flow-chart of the process is depicted in Figure 6.1.

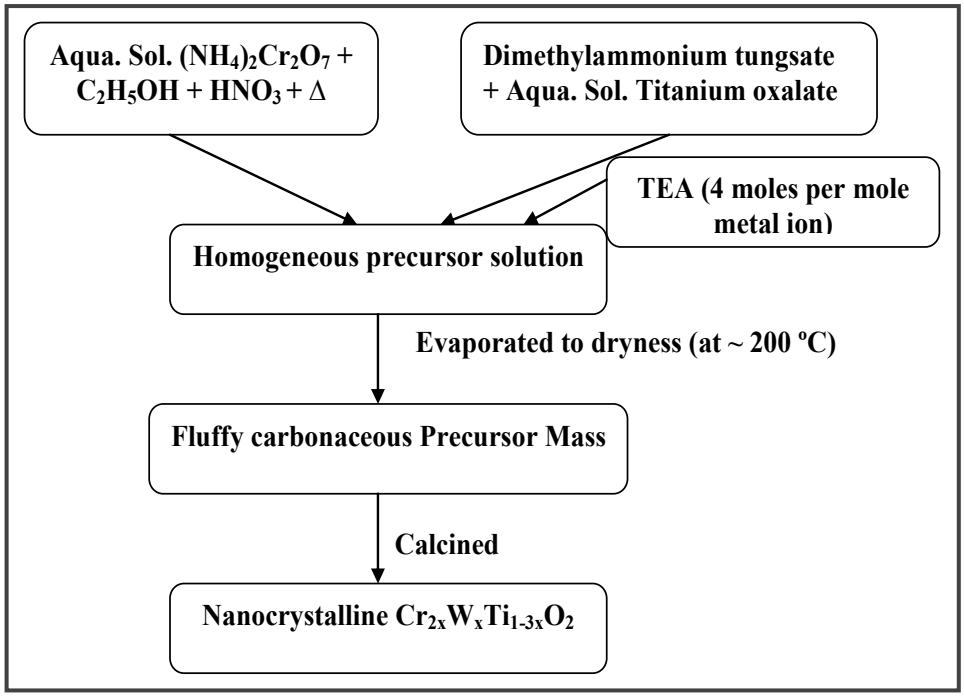

Figure 6.1: *Process for the preparation of the nanocrystalline solid solution compositions of* $Cr_{2x}W_xTi_{1-3x}O_2$.

6.5 Techniques for Characterization of the Prepared Nanocrystalline Powders of $Cr_{2x}W_xTi_{1-3x}O_2$ (x = 0.05, 0.1, 0.15)

The phase identification in the oxide solid solutions was performed using room temperature XRD with CuK_α radiation and Ni filter. In the XRD studies, the powders obtained at different heat treatment temperatures were recorded in the 2θ range from 20˚ to 70˚ for rutile phase. The crystallite size (D) and the effective strain (η) in the solid solution compositions were calculated from the full widths at half maximum (FWHM) of the diffraction peaks (2θ range = 15°-65°; step = 0.025°) after introducing the correction for instrumental broadening using standard silicon. The FWHM were expressed by the following equations (Qadri *et al.*, 1999) considering the peaks to be of the Gaussian type:

$$(\beta^o)^2 = (\beta^m)^2 - (\beta^s)^2 ;$$

and $$\frac{\beta^O \cos\theta}{\lambda} = \frac{1}{D} + \frac{\eta \sin\theta}{\lambda}$$

In the above equation the meaning of the terms such as β^o, β^m, β^s, θ, and λ have been described in the previous chapter of this thesis (Chapter 2, Section 2.5). The crystallite sizes (D) and the effective strains (η) in the powder samples were respectively obtained from the intercept at x = 0 and the slope of the best-fit line plot of ($\beta^{\circ}\cos\theta/\lambda$) versus ($\sin\theta/\lambda$). The fraction of rutile phase was calculated in the compositions at various heat-treated temperatures using the Spurr equation (Spurr *et al.*, 1957). The Spurr equation has been stated earlier (Chapter 5, Section 5.5). Simultaneously recorded thermogravimetric and differential thermal analysis (TG/DTA) of the precursor powders were carried out in air at a heating rate of 5 °C/min. UV-visible-NIR spectroscopy studies for the calcined powders were carried out in Ocean Optics SD 2000. The high-resolution transmission electron microscopy (HRTEM) measurements were carried out for the prepared powders. Particle size distributions of both the samples were determined by using the UTHSCSA Image Tool program (version 3.00) using three TEM images each containing ~50 particles. The BET specific surface areas of the calcined powders were determined. The color of the pigments was assessed from *CIEL*a*b** color parameter measurements. The instruments, used for the characterization remained the same as is mentioned in Chapter 2 and Section 2.5.

6.6 Results and Discussion

6.6.1 Thermal Analysis of the Nanocrystalline $Cr_{2x}W_xTi_{1-3x}O_2$ (x = 0.05, 0.10, 0.15) Precursor

The thermal studies of the carbonaceous precursors for the composition- $Cr_{2x}W_xTi_{1-3x}O_2$ (x = 0.05) are depicted in Figure 6.2. The differential thermal analysis (DTA) curves for all the precursor compositions revealed a broad exothermic thermal affect between 250 °C and 470 °C with their respective peak positioned around 445±10 °C.

This exothermic affect may be attributed to the oxidation of the organic remnants from the decomposed metal-complexes and TEA present in the carbonaceous precursors. The entire thermal affect was accompanied by evolution of large amounts of gases such as, water vapor, and oxides of carbon and nitrogen etc., which was manifested by a sharp, single step weight loss in the thermogravimetric (TG) curve (around 70%) and a single peak in the differential thermogravimetric (DTG) curve. The TG curves in Figure 6.2 shows that the weight loss from the amorphous precursor powders continued beyond the peak temperatures of the exothermic affect revealing that samples were not completely carbon free at around 445±10 °C. Crystallization of the oxide phase (i.e., formation of the oxide solid solution) was not very clearly visible from the DTA curve however, a small kink in the curve at around 500°C, without any visible weight loss in the TG/DTG curves, may be attributed to it. The phase transformation from anatase to rutile form was not detectable from DTA curves because of the small and gradual changes involved.

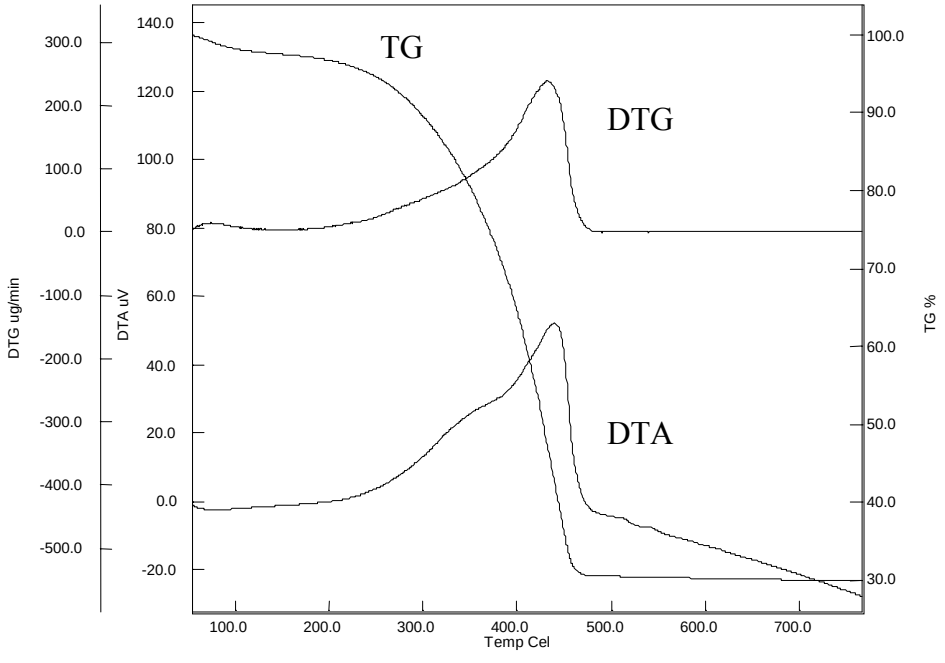

Figure 6.2: *Simultaneously recorded TG/ DTG/ DTA plots of the carbonaceous precursors of $Cr_{2x}W_xTi_{1-3x}O_2$ (x = 0.05) solid solution compositions.*

6.6.2 Composition, Phase and Structural Analysis of the Nanocrystalline $Cr_{2x}W_xTi_{1-3x}O_2$ (x = 0.05, 0.10, 0.15)

Phase analysis and structural characterization of the prepared $Cr_{2x}W_xTi_{1-3x}O_2$ (x = 0.05, 0.10, 0.15) were carried out through room temperature X-ray powder diffraction (XRD) studies. Figure 6.3 shows the characteristic XRD patterns for the $Cr_{2x}W_xTi_{1-3x}O_2$ (x = 0.05) precursor powders, when heat-treated at various temperatures between 450 ^oC to 800 ^oC for 2 h. The virgin precursors were amorphous to X-ray and crystallization of the oxide phase began at calcination temperatures higher than 450 °C, which was reflected by the emergence of broad, low-intensity diffraction lines corresponding to the anatase (d_{101}) and rutile (d_{110}) phases. At calcination temperature of 550 °C for 2 h, the intensities of the d_{101} and d_{110} lines, corresponding to the anatase and the rutile phase respectively, were comparable. Increase in the heat-treatment temperatures to 600 °C (and beyond) resulted in crystal growth and increase in the rutile fraction in the samples, which was evident by gradual sharpening of the diffraction lines, and increase in the intensity of the d_{110} lines corresponding to the rutile phase and diminishing of the d_{101} corresponding to the anatase phase.

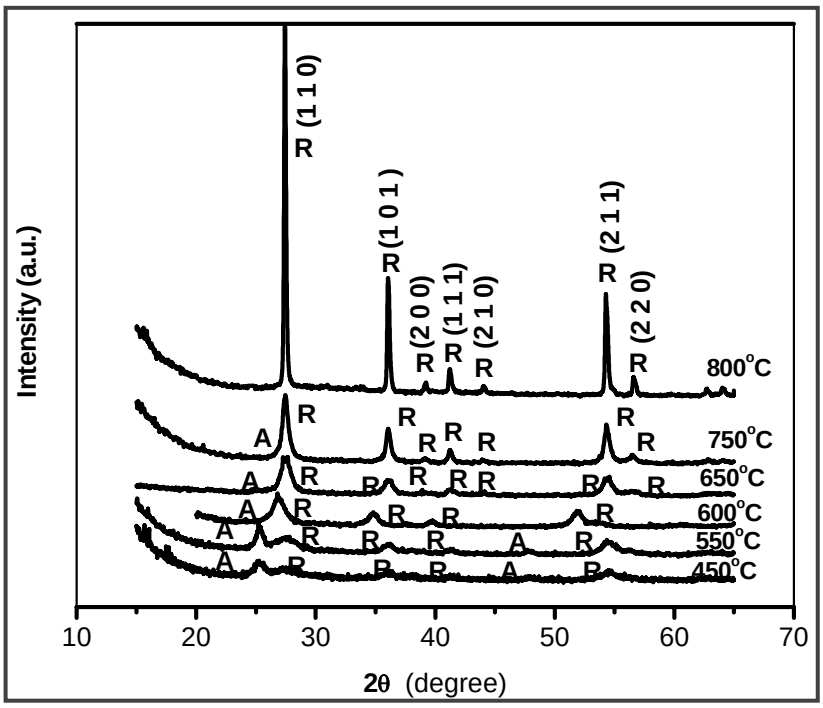

Figure 6.3: *X-ray diffractograms (using CuK_α radiation) of the $Cr_{2x}W_xTi_{1-3x}O_2$ (x = 0.05) precursors on calcination at various temperatures.*

The percentages of the rutile phase, determined from the relative intensities of the XRD peaks corresponding to the anatase and the rutile phases in the $Cr_{2x}W_xTi_{1-3x}O_2$ (x = 0.05, 0.1, and 0.15) compositions at various heat-treated temperatures are tabulated in Table 6.1 along with the tap densities (discussed in Chapter 5, Section 5.6.2) for x = 0.05 composition. On calcination of the precursors at 750 °C for 2 h, the percentage of the rutile phase in $Cr_{2x}W_xTi_{1-3x}O_2$ (x = 0.05) was found to be around 96%, and the pure rutile phase was obtained at the calcination temperatures of 800 ^oC for 2 h. The XRD peaks for the various solid solution compositions were indexed using the standard data available for the rutile phase (JCPDS card no. 781510) and the same have been shown in Figure 6.4. It was observed that the precursors of the oxide solid solution with $x \geq 0.2$, the formation of the rutile phase was accompanied by the phase of Cr_2O_3 when the heat-treatment of the compositions were carried out between 650 °C-900 °C. Prolonging the heat-treatment period (for 20-30 h) at higher temperatures (1300-1400 ^oC) eventually resulted in the pure rutile phase in these precursors (i.e. for $x \geq 0.2$) however. This was accomplished at the expense of loss of the nanocrystallinity in the sample.

Table 6.1: *Percentage of rutile Phase, relative XRD intensities of the anatase and rutile phases and tap densities of the various $Cr_{2x}W_xTi_{1-3x}O_2$ compositions at different calcination temperatures*

Calcination Temperature	**Rutile Phase (%) for Compositions**			**XRD Intensities of the A and R phases for Compositions***			**Tap densities (gm/cc)**
	x=0.05	**x=0.10**	**x=0.15**	**x=0.05**	**x=0.10**	**x=0.15**	**x=0.05**
550 ºC for 2h	41.0	72.4	75.2	A (s), R (w)	A (mw), R(s)	A (mw), R(s)	0.1325
650 ºC for 2h	85.8	90.2	92.8	A(mw), R(s)	A (w), R(s)	A (w), R(s)	0.1633
750 ºC for 2h	96.1	98.3	98.0	R(s), A (vw)	R(s), A (vw)	R (s), A (vw)	0.1758
800 ºC for 2h	100.0	100.0	100.0	R (s)	R (s)	R (s)	0.2345

* Relative XRD Intensities of the Anatase (A) and Rutile (R) Phases; s= strong, w = weak, mw = medium weak, vw= very week

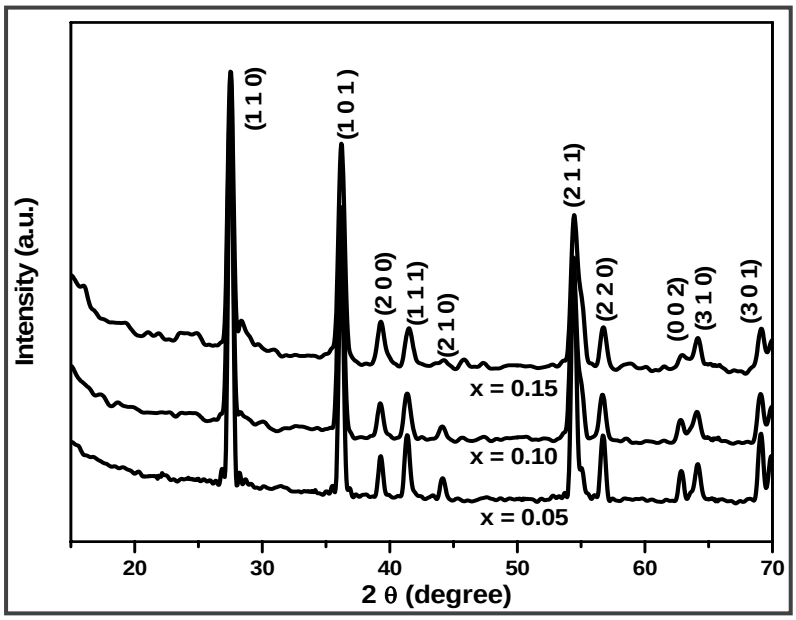

Figure 6.4: *X-ray diffractograms (using CuK_α radiation) of the various $Cr_{2x}W_xTi_{1-3x}O_2$ solid solution compositions after calcination at 800 ºC for 2 h.*

It can be thus inferred that the metastable anatase phase (typically preserves a large surface area) underwent transformation to the rutile phase on calcination between 550 °C-800 °C. At calcination temperatures above 550 °C, a more rapid phase transformation from anatase to rutile was observed for x = 0.10 and 0.15 compositions. The crystallite sizes and the surface areas for the calcined (800 °C for 2 h) $Cr_{2x}W_xTi_{1-3x}O_2$ (x = 0.05, 0.10, 0.15) compositions are shown in Table 6.2. Figure 6.5 shows the plot of ($\beta^o cos\theta/\lambda$) versus ($sin\theta/\lambda$) for the typical

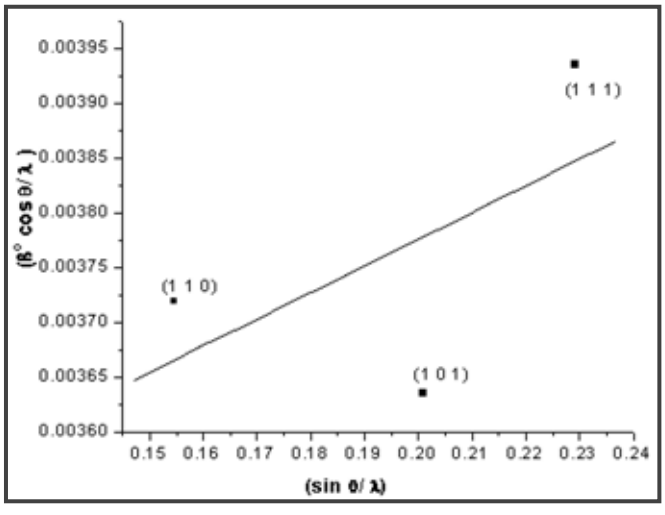

Figure 6.5: *Plot of ($\beta^o cos\theta/\lambda$) versus ($sin\theta/\lambda$) for $Cr_{2x}W_xTi_{1-3x}O_2$ (with x = 0.05) solid solution composition.*

solid solution composition with x = 0.05, the effective strain (η), obtained from the slope of the plot, was found to be 0.00243.

Table 6.2: *Variation in crystallite size, surface area and particle size for calcined (at 800 ºC for 2 h) $Cr_{2x}W_xTi_{1-3x}O_2$ solid solution with change in dopant concentration*

Composition of $Cr_{2x}W_xTi_{1-3x}O_2$	Crystallite size§ (nm) (± 2 nm)	BET surface area (m^2g^{-1})	TEM particle size* (nm) (± 5nm)
X= 0.05	30	60	40.0
X= 0.10	32	56	45.0
X= 0.15	35	58	38.0

§: Crystallite size calculated from FWHM of the X-ray diffraction peaks

***:** Average of the smallest visible isolated particle/crystallite agglomerate as observed from TEM studies for the respective compositions

The lattice parameters (i.e., *a* and *c*) for the calcined (800 ^oC for 2 h) rutile phase $Cr_{2x}W_xTi_{1-3x}O_2$ solid solutions, which were calculated following the reflection planes (*200*) and (*002*), have been tabulated in Table 6.3. These calculated values of *a* and *c* were found to be in close agreement with those reported for the standard rutile phased TiO_2 (JCPDS data card no.781510). As there was no evidence of any additional phase in the samples, which were calcined at 800 ºC, and also because the unit-cell parameters fairly matched with the standard values of the rutile phase, therefore the structure of $Cr_{2x}W_xTi_{1-3x}O_2$ solid solutions (calcined at 800 ^oC) was confirmed to be of purely rutile type. Increase in the lattice parameters *a* and *c*, with increasing fraction of Cr(III) [i.e., from x = 0.05 to x = 0.15] in the solid solution $Cr_{2x}W_xTi_{1-3x}O_2$, caused by substitution of the Ti^{4+} ions (r = 0.605 Å) by Cr^{3+} and W^{6+} ions followed the Vegard's law (West, 1984).

Table 6.3: *Variation in lattice parameters (a, c) and volume (at 800 ºC for 2 h) $Cr_{2x}W_xTi_{1-3x}O_2$ solid solution with change in dopant concentrations*

Composition of $Cr_{2x}W_xTi_{1-3x}O_2$	Lattice parameter (*a*) (Å)	Lattice parameter (*c*) (Å)	Volume (Å^3)	*c/a*
X= 0.05	4.583 ± 0.004	2.955 ± 0.003	62.05 ± 0.02	0.6447
X= 0.10	4.586 ± 0.002	2.956 ± 0.002	62.15 ± 0.01	0.6445
X= 0.15	4.589 ± 0.003	2.956 ± 0.005	62.26 ± 0.02	0.6441

6.6.3 Morphology and Microstructural Studies of the Nanocrystalline $Cr_{2x}W_xTi_{1-3x}O_2$ (x = 0.05, 0.1, 0.15) Powders

The finer morphological details of the calcined (800 ºC for 2 h) solid solution samples and their size-distributions were studied using Transmission Electron Microscopy (TEM). The smallest visible particles in the bright field electron micrograph can be identified as single crystallites and/or their aggregates. Figure 6.6 and 6.8 depict the TEM micrographs for the calcined (800 ºC for 2 h) $Cr_{2x}W_xTi_{1-3x}O_2$ (x = 0.05 and 0.10) solid solution compositions respectively. It was observed that the particles were almost spherical with average particle diameters ranging between of 30-60 nm. The distribution in particle sizes for the $Cr_{2x}W_xTi_{1-3x}O_2$ (x = 0.05 and 0.10) solid solution compositions, evaluated from TEM studies, are shown through bar charts in Figure 6.7 and 6.9 respectively. Selected-area electron diffraction (SAED) pattern of the calcined (800 ºC for 2 h) $Cr_{2x}W_xTi_{1-3x}O_2$ (x = 0.05) composition (Figure 6.10) showed distinct rings corresponding to the (*110*), (*101*), (*111*), (*211*) planes in a rutile lattice, thus inferring the powders to be small agglomerates of nanosized polycrystallites having the rutile structure. High resolution TEM (HRTEM) image for the same sample in Figure 6.11 depicted the finer details in their crystal structure. Lattice spacing of about 3.22 Å between the adjacent lattice planes, as examined from the

HRTEM image, corresponded to the distance between (*110*) crystal planes in the rutile structure, as the crystals were oriented along the (*110*) plane.

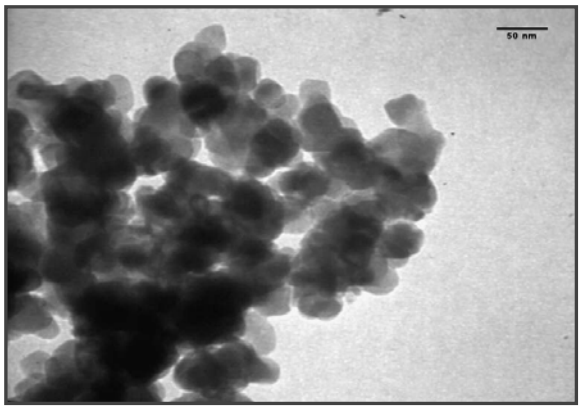

Figure 6.6: *Bright field TEM micrograph of the calcined (800 ºC for 2 h) $Cr_{2x}W_xTi_{1-3x}O_2$ (x = 0. 05) solid solution composition.*

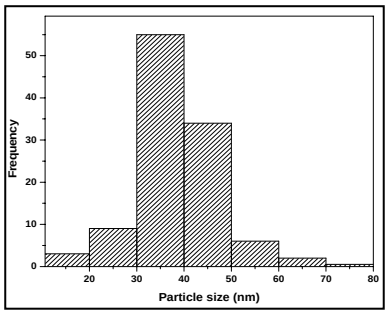

Figure 6.7: *Distribution of particle sizes, evaluated from TEM studies, for the calcined (800 ºC for 2 h) $Cr_{2x}W_xTi_{1-3x}O_2$ (x = 0. 05) solid solution composition.*

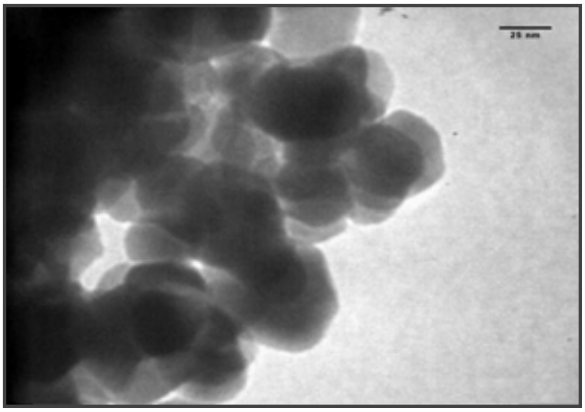

Figure 6.8*: Bright field TEM micrograph of the calcined (800 ºC for 2 h) $Cr_{2x}W_xTi_{1-3x}O_2$ (x = 0.10) solid solution composition.*

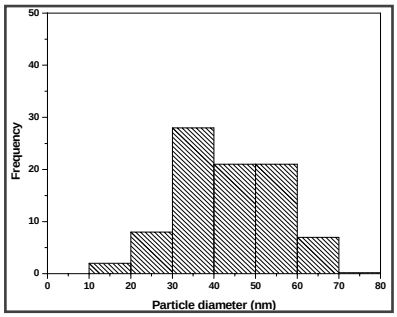

Figure 6.9: *Distribution of particle sizes, evaluated from TEM studies, for the calcined (800 ºC for 2 h) $Cr_{2x}W_xTi_{1-3x}O_2$ (x = 0. 10) solid solution composition.*

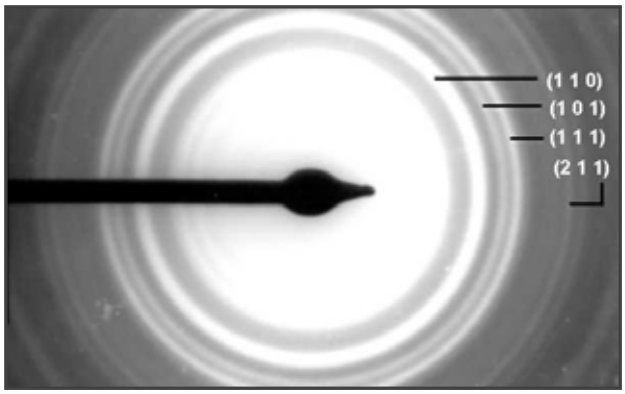

Figure 6.10: *SAED pattern of the calcined (800 ºC for 2 h) $Cr_{2x}W_xTi_{1-3x}O_2$ (x = 0.05) composition showing distinct rings corresponding to the (110), (101), (111), (211) planes in a rutile lattice.*

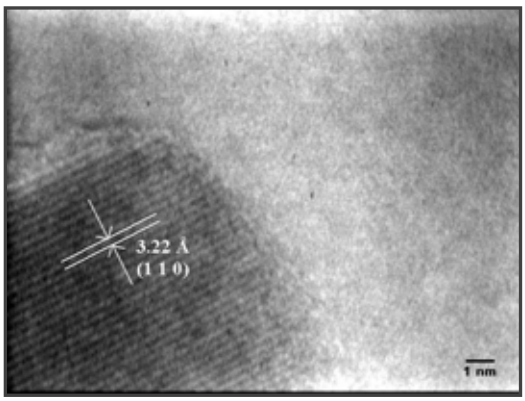

Figure 6.11: *HRTEM image of the calcined (800 ºC for 2 h) $Cr_{2x}W_xTi_{1-3x}O_2$ (x = 0.05) composition.*

The external morphology of the prepared solid solutions was visualized through Field-emission scanning electron microscopy studies. FESEM micrograph (Fig 6.12) for the calcined (800 º C for 2 h) $Cr_{2x}W_xTi_{1-3x}O_2$ (x = 0.05) solid solution composition shows the aggregates of small particles. The individual particles showed the size below 100 nm.

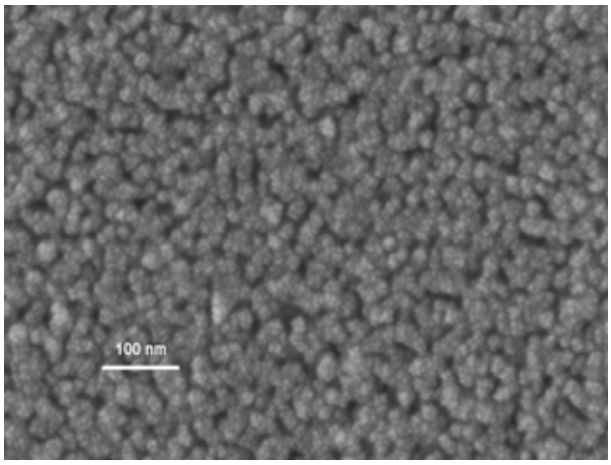

Figure 6.12: *FESEM micrograph of the calcined (800 ºC for 2 h) $Cr_{2x}W_xTi_{1-3x}O_2$ (x = 0.05) solid solution composition.*

6.6.4 UV-visible Spectroscopy Studies and Color Measurements of the Nanocrystalline $Cr_{2x}W_xTi_{1-3x}O_2$ (x = 0.05, 0.1, 0.15) Powders

The UV-visible absorption spectra for the calcined (at 800 ºC for 2 h) $Cr_{2x}W_xTi_{1-3x}O_2$ solid solutions, shown in Figure 6.12 revealed a wide absorption band ranging from 250 to 850 nm in all the samples, with three distinct humps positioned at 330-340 nm, 425-470 nm, and 590-640 nm, corresponding to the three respective spin allowed *d-d* transitions from the Cr^{3+} ions in octahedral environment. Ti^{4+} ion in titanium dioxide, being a $3d^0$ system, has no 3*d*-electrons for *d-d* electronic transition and hence appears as a white powder with no absorption in the visible range (Figure 6.12). According to crystal field theory (Marfunin, 1979), bulk Cr_2O_3 samples with Cr^{3+} ion ($3d^3$ electronic configuration) in an octahedral environment is predicted to have three absorption bands assigned to three electronic spin allowed transitions of [$^4A_{2g}$(F) $\rightarrow ^4T_{2g}$ (F)] at 600 nm; [$^4A_{2g}$(F) $\rightarrow ^4T_{1g}$ (F)] at 455 nm; and [$^4A_{2g}$(F) $\rightarrow ^4T_{1g}$ (P)] in the

UV region (Figure 6.13). The energies of the first two electronic spin allowed transitions exist in the visible light energy range (Lever, 1968) while the third transition lies is in the ultraviolet range and therefore does not affect the color of the samples. Observed shifts in the absorption bands of the Cr^{3+} ions in $Cr_{2x}W_xTi_{1-3x}O_2$ solid solutions to that of the bulk Cr_2O_3 samples may be due to deformation of the octahedral environment of the Cr^{3+} ions to lesser symmetry in the former. The Ti^{4+} ions in the oxygen octahedra in the rutile lattice is already slightly distorted and their substitution by slightly larger sized Cr^{3+} ions, for the formation of the solid solutions, may cause further deformation of the octahedra and may attribute to the shifts in the absorption bands of the Cr^{3+} ions in the solid solutions compared to those observed in the bulk Cr_2O_3 samples, where the Cr^{3+} ions exists in a symmetric octahedral environment. The broadness in the absorption spectra for the $Cr_{2x}W_xTi_{1-3x}O_2$ solid solutions may be due to existence of additional absorption bands corresponding to charge transfers between the constituent metal ions [Cr(III), Ti(IV), W(VI)], and between ligand and metal ions besides the spin allowed *d-d* transitions in Cr(III) ion in octahedral environment. Thus, the allowed *d-d* transitions of the Cr(III) get masked by the existence of absorption bands corresponding to metal-metal and metal-ligand charge transfers and their overlap in the UV-visible spectral range. Additionally, the substitution of the Cr^{3+} ions in the distorted rutile environment is also likely to contribute towards the broadness of the bands.

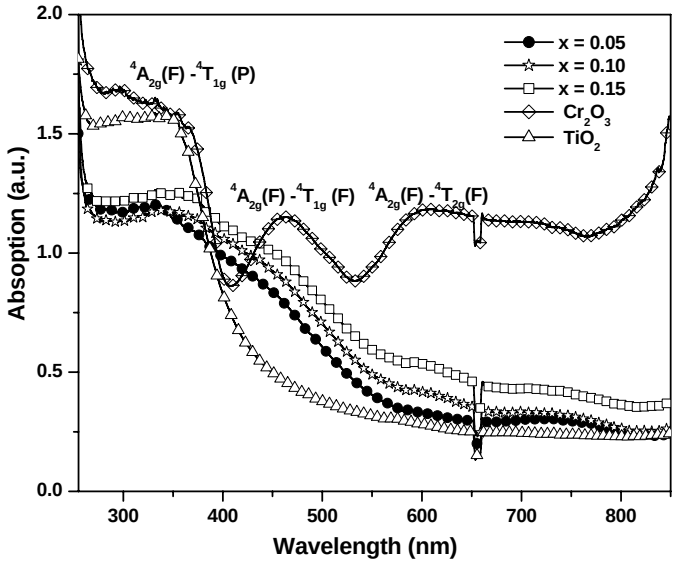

Figure 6.13: *UV-visible absorption spectra for calcined (at 800 ºC for 2 h) powders of the $Cr_{2x}W_xTi_{1-3x}O_2$ solid solution compositions.*

The particle sizes, in the three solid solution compositions, were almost in the same range (30-60 nm), thus the scattering due to the particle size can be assumed same for all the compositions. In this respect, the relation between reflectivity of the powder at λ = 700 nm and dopant concentrations x (in mole %) can be examined by plotting *K/S* (at λ = 700 nm) versus x, *K/S* for the solid powders, calculated applying the Kumelka-Munk equation (Johnston, 1973) that can be expressed as:

$$\frac{K}{S} = \frac{(1-R)^2}{2R}$$

where, *K* is the absorption coefficient and *S* is the scattering coefficient, *R* is the decimal fractional reflectance. Since the sample powders of all compositions had almost same particle sizes, thus *S* can also be assumed to be invariable for all the sample powders. The plot of *K/S* (at λ = 700 nm) versus x in Figure 6.14 shows the linearity confirming the intrusion of the dopants into the TiO_2 matrix to form the solid solutions (Huguenin *et al.*, 1998).

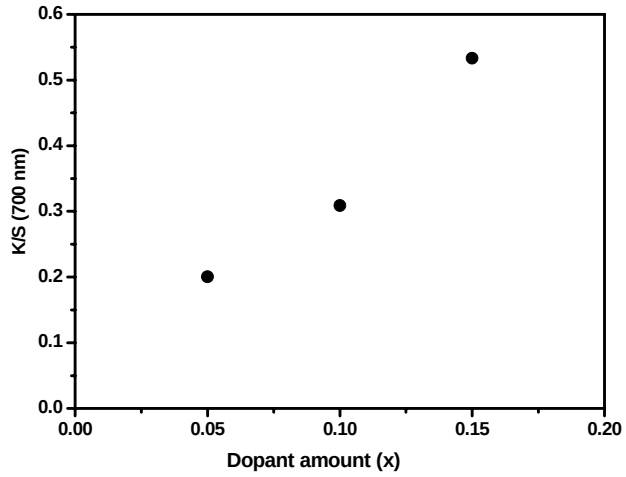

Figure 6.14: *Plot of K/S versus dopant amount (x) for the various $Cr_{2x}W_xTi_{1-3x}O_2$ solid solution compositions.*

The *CIE-L*a*b** measurements of $Cr_{2x}W_xTi_{1-3x}O_2$ (x = 0.05) solid solution heat treated at its calcination temperature has been done as a prototype. The *CIE-*

*L*a*b** measurements represent a reddish brown colour of the sample (i.e. high *b** (54.3) and low *a** (18.6) parameters) and a light colour (*L** by 67.8).

The BET surface areas for all compositions of $Cr_{2x}W_xTi_{1-3x}O_2$ solid solutions were found to lie between 56-68 m^2g^{-1}. The surface areas for the various compositions of the calcined (800 ºC for 2 h) $Cr_{2x}W_xTi_{1-3x}O_2$ solid solution are summarized in Table 6.2. The tap densities, which correspond the fluffiness of the powder, were observed to increase with increase in calcination temperatures for all the compositions of the solid solution (Table 6.1). This may be due to decrease in the volume of the samples brought about by the reduction of porosity on sintering of the particles at increased heat-treatment temperatures.

For studying the thermal stabilities of the solid solution compositions at high temperatures, the final powders were annealed at 1200 ºC for 1 h. XRD phase analysis (Figure 6.15) of the annealed powders showed no phase change thereby establishing that the thermal stabilities of the solid solution compositions were stable even when subjected to heat treatment at the temperatures of 1200 ºC for 1 h. Furthermore, XRD phase analysis of the powders after being subjected to treatment with dilute HCl, dilute HNO_3 and dilute NaOH were found to remain unchanged reflecting the retention of their chemical composition and colour even on post treatment thereby validating their chemical inertness under acidic and alkaline conditions.

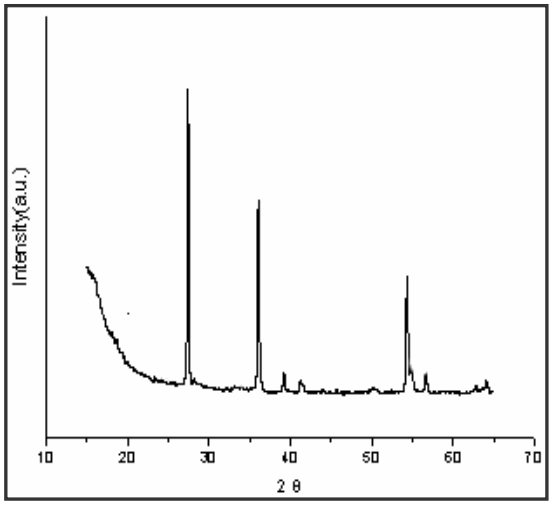

Figure 6.15: *XRD phase analysis of $Cr_{2x}W_xTi_{1-3x}O_2$ (x =0.05) solid solution composition after annealing at 1200 ºC for 1 h.*

5.7 Major Findings in the present Investigation

- Nanocrystalline rutile structured $Cr_{2x}W_xTi_{1-3x}O_2$ (x= 0.05, 0.10, 0.15) powders have been prepared through pyrolysis of metal ion-ligand complex based precursor solution.
- The preparation method established the use of dimethyl ammonium tungstate and titanium oxalate as respective stable water-soluble sources of tungsten and titanium.
- Pure rutile phase was formed through heat-treatment of the precursor powders at 800 ^oC.
- TEM study showed average diameters ranging between of 30 and 60 nm for all three compositions.
- The UV-visible-NIR spectra for all solid solutions exhibited three absorption bands due to *d*-*d* transitions of *d*-electrons of Cr^{3+} ions.

References

Alfred, S. and Adriana, U. (2003), Electronic Study of Doping TiO_2 Catalysts 2, Doping with Higher Valence Ions (WO_3) and Variable Valence Ions (Cr_2O_3), Progress in Catalysis, Vol. 12, No. 1, pp. 51-69.

Herrmann, J. M., Disdier, J. and Pichat, P. (1984), Effect of Chromium Doping on the Electrical and Catalytic Properties of Powder Titania under UV and Visible Illumination, Chemical Physics Letter, Vol. 6, pp. 618-622.

Huguenin, D. and Chopin, T. (1998), New Titanium Precursors for Manufacture of Colored Pigments, Dyes and Pigments, Vol. 37, No. 2, pp. 129-134.

Hund, F. (1962), United States Patent, 3,022,186.

Johnston, R. M. (1973), Color Theory, In Pigment Handbook, Patton, T.C. (Editor), Wiley-Interscience, United States of America, Vol. 3, pp. 229-288.

Lever, A. B. P. (1968), Inorganic Electron Spectroscopy, Elsevier, Amsterdam.

Malati, M. A., Wong, W. K. (1984), Doping Titanium Dioxide for Solar Energy Applications, Surface Technology, Vol. 22, No. 4, pp. 305-322.

Maloney, J. (2002), Titanate Pigments: Colored Rutile, Priderite, and Pseudobrookite Structured Pigments, In High Performance Pigments, Smith, H. M. (Editor), Wiley-VCH, Verlag-GmbH, Weinheim, Germany, pp.53-73.

Marfunin, A. S. (1979), in Physics of Minerals and Inorganic Materials, Springer-Verlag, Berlin Heidelberg New York, p. 340.

Matteucci, F., Cruciani, G., Dondi, M. and Raimondo, M. (2006), The Role of Counterions (Mo, Nb, Sb, W) in Cr-, Mn-, Ni- and V-Doped Rutile Ceramic Pigments. Part 1. Crystal Structure and Phase Transformation, Ceramics International, Vol. 32, No. 4, pp. 385-392.

Qadri, S. B., Skelton, E. F., Hsu, D., Dinsmore, A. D., Yang, J., Gray, H. F., Ratna, B. R. (1999), Size Induced Transition-Temperature Reduction in Nanoparticles of ZnS, Physics Review B, Vol. 60, No. 13, pp. 9191-9193.

Ramos, E., Veiga, M. L., Fernández, R., Sáez-Puche, R. and Pico, C. (1991), Synthesis, Structural Characterization, and Two-Dimensional Antiferromagnetic Ordering for the Oxides $Ti_{3\ (1-x)}\ Ni_x\ Sb_{2x}O_6$ ($1.0 \geq x \geq 0.6$), Journal of Solid State Chemistry, Vol. 91, pp. 113-120.

Richards, L. W. (1973), in Pigment Handbook, Patton, T. C. (Editor), Wiley-Interscience, United States of America, Vol. 3, pp 93.

Sorlí, S., Tena, M. A., Badenes, J. A., Calbo, J., Llusar, M. and Monrós, G. (2004a), Structure and Color of $Ni_xA_{1-3x}B_{2x}O_2$ (A = Ti, Sn; B = Sb, Nb) Solid Solutions, Journal of the European Ceramic Society, Vol. 24, pp. 2425-2432.

Sorlí, S., Tena, M. A., Badenes, J. A., Llusar, M. and Monrós, G. (2004b), Study of Nickel Precursors in $(Ni,M,Ti)O_2$ (M = Sb, Nb) Yellow Ceramic Pigments, British Ceramic Transactions, Vol. 103, No. 1, pp. 10-14.

Spurr, R. A. and Myers, H. (1957), Quantitative Analysis of Anatase-Rutile Mixtures with an X-Ray Diffractometer, Analytical Chemistry, Vol. 29, No. 5, pp. 760-762.

Swiler, D. R. and Livingston, J. (1993), Mixed Metal Oxide "Titanate" Pigments, Int. Conf. Prod. Appl. Spec. Inorganic Pigments, pp. 32-45.

Tavala, T. P., Brinzan, N. G. and Florea, V. (1977), Red-Brown Pigments in the Cr_2O_3-TiO_2-WO_3 System, Revue Roumaine de Chimie. Vol. 22, No. 5, pp. 787-792.

Tena, M. A., Morós, J., Carda, G., Cordoncillo, E., Escribano, P. and Alarcón, J. (1994), Synthesis of $Cr_xTi_{1-2x}Nb_xO_2$ $0 \leq x \leq 0.5$ Rutile Solid Solutions from Alkoxides, Journal Materials Science, Vol. 29, pp. 3817-3821.

West, A. R. (1984), Solid State Chemistry and its Applications, John Wiley and Sons. New York, p. 368.

List of Figures

		Page
Figure 1.1:	Schematic illustration for Bottom-up and Top-down approach.	6
Figure 1.2:	Schematic representation of metal ion-ligand complex based precursor solution method.	14
Figure 1.3:	A photograph of black carbonaceous fluffy mass.	14
Figure 1.4:	Probable metal-TEA complex.	15
Figure 2.1:	Schematic representation of the preparation of the aqueous solution of niobium tartrate.	45
Figure 2.2:	Schematic representation of the preparation of the nanocrystalline $CuNb_2O_6$.	47
Figure 2.3:	Simultaneously recorded TGA/DTA plots of the carbonaceous precursors of $CuNb_2O_6$.	49
Figure 2.4:	(a) X-Ray diffractogram (using CuK_α radiation) of the $CuNb_2O_6$ calcined at 700 ºC for 2 h. (b) Rietveld refinement of monoclinic $CuNb_2O_6$ calcined at 700 ºC for 2 h. Vertical bars show the positions of Bragg reflections.	50
Figure 2.5:	EDX analysis of the $CuNb_2O_6$ after calcination at 700 ºC for 2 h.	50
Figure 2.6:	(a) Bright field TEM micrograph of the calcined (at 700 ºC for 2h) $CuNb_2O_6$. (b) SAED pattern of the calcined (at 700ºC for 2h) $CuNb_2O_6$.	51
Figure 2.7:	FESEM image of nanocrystalline $CuNb_2O_6$ powders.	52
Figure 2.8:	FESEM image of pellet surface derived from nanosized $CuNb_2O_6$ powder.	52
Figure 2.9:	Schematic representation of (a) porous and (b) compact sensing layer with geometry and energy band. x_g grain size, L_D Debye length, eV_s band bending, z_o thickness of the depleted surface layer and z_g layer thickness.	53
Figure 2.10:	Photograph of setup equipment for resistance measurements and the cylindrical test-chamber with steel made sample holder (Inset).	54
Figure 2.11:	Setup equipment for in-situ resistance measurements	55

Figure 2.12:	Arrhenius plot for electrical conductivity of $CuNb_2O_6$ in air.	58
Figure 2.13:	Response characteristics of porous pellets of nanocrystalline $CuNb_2O_6$ towards 500 ppm each of H_2, LPG, and NH_3 in air as a function of temperature.	59
Figure 2.14:	Responses of porous pellets of nanocrystalline $CuNb_2O_6$ towards 500 ppm of H_2 in air at different temperatures.	59
Figure 2.15:	Responses of porous pellet of nanocrystalline $CuNb_2O_6$ towards 500 ppm of LPG in air at different temperatures.	59
Figure 2.16:	Responses of porous pellet of nanocrystalline $CuNb_2O_6$ towards 500 ppm of NH_3 in air at different temperatures.	59
Figure 2.17:	Electrical resistance of porous pellet of $CuNb_2O_6$ in alternating environments of air and (a) 500 ppm H_2 (b) 500 ppm LPG at 300 ºC and (c) 500 ppm NH_3 at 400 ºC.	60
Figure 2.18:	Variation of sensitivity of porous pellet of $CuNb_2O_6$ with concentration of H_2 and LPG at 300 ºC.	61
Figure 2.19:	Temperature variation of response time and recovery time for $CuNb_2O_6$ for 500 ppm H_2, LPG and NH_3.	61
Figure 3.1:	Schematic representation of the preparation of the nanocrystalline powders of $FeNbO_4$ composition.	73
Figure 3.2:	Simultaneously recorded TGA/DTA plots of the carbonaceous precursors of $FeNbO_4$.	74
Figure 3.3:	(a) X-ray diffractograms (using CuK_α radiation) of the $FeNbO_4$ precursor on calcination at various temperatures. (b) Rietveld refinement of orthorhombic $FeNbO_4$ calcined at 850 ºC for 3 h. Vertical bars show the positions of Bragg reflections.	75
Figure 3.4:	X-ray diffractogram (using CuK_α radiation) of the platinum incorporated $FeNbO_4$ after calcination at 850 ºC for 1 h.	77
Figure 3.5:	EDX pattern of (1 wt %) platinum impregnated $FeNbO_4$ after calcination at 850 ºC for1 h.	77
Figure 3.6:	Bright field TEM micrograph of the calcined (at 850 ºC for 3 h) $FeNbO_4$.	78
Figure 3.7:	Bright field TEM micrograph of Pt-$FeNbO_4$ after calcined (at 850 ºC for 1 h). (Inset) SAED pattern of Pt-$FeNbO_4$.	78

Figure 3.8:	FESEM micrograph of pellet derived from the calcined (at 850 ºC for 2 h) powders of the nanocrystalline $FeNbO_4$	79
Figure 3.9:	FESEM micrograph of pellet derived from the calcined (at 850 ºC for 1 h) powders of the nanocrystalline Pt-$FeNbO_4$.	79
Figure 3.10:	BET isotherms of nanocrystalline $FeNbO_4$ and platinum (1 wt %) incorporated $FeNbO_4$.	79
Figure 3.11:	Arrhenius plot for electrical conductivity of $FeNbO_4$ and platinum (1 wt %) incorporated $FeNbO_4$ in air.	81
Figure 3.12:	Response characteristics of nanocrystalline $FeNbO_4$ and Pt-$FeNbO_4$ in porous pellet forms towards 500 ppm each of H_2, LPG, and NH_3 in air as a function of temperature.	83
Figure 3.13:	Response characteristics of $FeNbO_4$ and platinum (1 wt %) incorporated $FeNbO_4$ for 500 ppm of LPG at 200 ºC.	83
Figure 3.14:	Electrical resistance of Pt-$FeNbO_4$ in alternating environments of air and LPG (500 ppm) at 200 ºC.	83
Figure 4.1:	Schematic representation of the preparation of the nanocrystalline $CuGa_2O_4$.	93
Figure 4.2:	(a) X-Ray diffractogram (using CoK_α radiation) of the $CuGa_2O_4$ calcined at 750 ºC for 2 h. (b) Rietveld refinement of monoclinic $CuGa_2O_4$ calcined at 750 ºC for 2 h. Vertical bars show the positions of Bragg reflections.	94
Figure 4.3:	EDX analysis of the $CuGa_2O_4$ after calcination at 750 ºC for 2 h.	95
Figure 4.4:	Bright field TEM micrograph of the calcined (at 750 ºC for 2 h) $CuGa_2O_4$.	96
Figure 4.5:	FESEM image of nanocrystalline $CuGa_2O_4$ powders.	97
Figure 4.6:	FESEM image of pellet surface derived from nanocrystalline $CuGa_2O_4$ powder.	98
Figure 4.7:	Arrhenius plot for electrical conductivity of $CuGa_2O_4$ in air and argon.	99
Figure 4.8:	Sensing characteristics of nanocrystalline $CuGa_2O_4$ in the form of porous pellet towards 500 ppm each of H_2, LPG, and NH_3 in air as a function of temperature.	100

Figure 4.9:	Responses of porous pellet of nanocrystalline $CuGa_2O_4$ towards 500 ppm of H_2 in air at different temperatures.	100
Figure 4.10:	Responses of porous pellet of nanocrystalline $CuGa_2O_4$ towards 500 ppm of LPG in air at different temperatures.	101
Figure 4.11:	Responses of porous pellet of nanocrystalline $CuGa_2O_4$ towards 500 ppm of NH_3 in air at different temperatures.	101
Figure 4.12:	Electrical resistance of porous pellet of $CuGa_2O_4$ in alternating environments of air and 500 ppm LPG at 350 ºC.	101
Figure 4.13:	Variation of response of porous pellet of nanocrystalline $CuNb_2O_6$ with concentration of H_2 and LPG at 350 ºC.	102
Figure 4.14:	Temperature variation of response time and recovery time for $CuGa_2O_4$ for 500 ppm H_2, LPG and NH_3.	102
Figure 5.1:	Schematic representation of the preparation of the aqueous solution of dimethylammonium tungstate.	112
Figure 5.2:	Schematic representation of the preparation of the aqueous solution of titanium oxalate.	113
Figure 5.3:	Schematic representation of the preparation of the nanocrystalline powders of $Ni_{0.1}W_{0.1}Ti_{0.8}O_2$	114
Figure 5.4:	Schematic representation of the synthesis of the nanocrystalline powders of $BaNiTi_7O_{16}$.	115
Figure 5.5:	Simultaneously recorded TGA and DTA plots of the carbonaceous precursors of solid solution composition: (a) $Ni_{0.1}W_{0.1}Ti_{0.8}O_2$, (b) $BaNiTi_7O_{16}$.	118
Figure 5.6:	X-ray diffractograms (using CuK_α radiation) of $Ni_{0.1}W_{0.1}Ti_{0.8}O_2$ precursor on calcination at various temperatures.	119
Figure 5.7:	X-ray diffractograms (using CuK_α radiation) of $BaNiTi_7O_{16}$ precursor on calcination at various temperatures.	122
Figure 5.8:	(a), (b), and (3): Bright field TEM micrograph of the calcined (800 ºC for 2 h) $Ni_{0.1}W_{0.1}Ti_{0.8}O_2$ solid solution. Figure-5.8(d): HRTEM image of the calcined (800 ºC for 2 h) $Ni_{0.1}W_{0.1}Ti_{0.8}O_2$ solid solution.	123
Figure 5.9:	SAED pattern of the calcined (800 ºC for 2 h) $Ni_{0.1}W_{0.1}Ti_{0.8}O_2$ showing distinct rings corresponding to the (1 0 1), (2 0 0), (2 2 0) planes in a rutile lattice.	124

Figure 5.10:	Bright field TEM micrograph of the calcined (850 ºC for 2 h) $BaNiTi_7O_{16}$ composition.	125
Figure 5.11:	SAED pattern of the calcined (850 ºC for 2 h) $BaNiTi_7O_{16}$ with a priderite structure.	125
Figure 5.12:	UV-visible-NIR absorption spectra for calcined (at 800 ºC for 2h) powder of the $Ni_{0.1}W_{0.1}Ti_{0.8}O_2$ solid solution.	126
Figure 5.13:	UV-visible-NIR absorption spectra for calcined (at 850 ºC for 2h) powder of the $BaNiTi_7O_{16}$ solid solution.	126
Figure 6.1:	Process for the preparation of the nanocrystalline solid solution compositions of $Cr_{2x}W_xTi_{1-3x}O_2$.	137
Figure 6.2:	Simultaneously recorded TGA/ DTG/ DTA plots of the carbonaceous precursors of $Cr_{2x}W_xTi_{1-3x}O_2$ (x = 0.05) solid solution composition.	139
Figure 6.3:	X-ray diffractograms (using CuK_α radiation) of the $Cr_{2x}W_xTi_{1-3x}O_2$ (x = 0.05) precursors on calcination at various temperatures.	140
Figure 6.4:	X-ray diffractograms (using CuK_α radiation) of the various $Cr_{2x}W_xTi_{1-3x}O_2$ solid solution compositions after calcination at 800 ºC for 2 h.	142
Figure 6.5:	Plot of ($\beta^o\cos\theta/\lambda$) versus ($\sin\theta/\lambda$) for $Cr_{2x}W_xTi_{1-3x}O_2$ (with x = 0.05) solid solution composition.	142
Figure 6.6:	Bright field TEM micrograph of the calcined (800 ºC for 2 h) $Cr_{2x}W_xTi_{1-3x}O_2$ (x = 0. 05) solid solution composition.	145
Figure 6.7:	Distribution of particle sizes, evaluated from TEM studies, for the calcined (800 ºC for 2 h) $Cr_{2x}W_xTi_{1-3x}O_2$ (x = 0. 05) solid solution composition.	145
Figure 6.8:	Bright field TEM micrograph of the calcined (800 ºC for 2 h) $Cr_{2x}W_xTi_{1-3x}O_2$ (x = 0.10) solid solution composition.	145
Figure 6.9:	Distribution of particle sizes, evaluated from TEM studies, for the calcined (800 ºC for 2 h) $Cr_{2x}W_xTi_{1-3x}O_2$ (x = 0. 10) solid solution composition.	146
Figure 6.10:	Selected-area Electron Diffraction (SAED) pattern of the calcined (800 ºC for 2h) $Cr_{2x}W_xTi_{1-3x}O_2$ (x = 0.05) composition showing distinct rings corresponding to the (110), (101), (111), (211) planes in a rutile lattice.	146

Figure 6.11: HRTEM image of the calcined (800 ºC for 2 h) $Cr_{2x}W_xTi_{1-3x}O_2$ (x = 0.05) composition. 146

Figure 6.12: FESEM micrograph of the calcined (800 ºC for 2 h) $Cr_{2x}W_xTi_{1-3x}O_2$ (x = 0.05) solid solution composition. 147

Figure 6.13: UV-visible absorption spectra for calcined (at 800 ºC for 2 h) powders of the $Cr_{2x}W_xTi_{1\ 3x}O_2$ solid solution compositions. 148

Figure 6.14: Plot of K/S versus dopant amount (x) for the various $Cr_{2x}W_xTi_{1-3x}O_2$ solid solution compositions. 149

Figure 6.15: Figure 6.15: XRD phase analysis of $Cr_{2x}W_xTi_{1-3x}O_2$ (x = 0.05) solid solution composition after annealing at 1200 ºC for 3 h. 150

List of Tables

		Page
Table 1.1:	Summary of changes observed in some of the physical properties for nanocrystalline materials.	2
Table 1.2:	Traditional properties associated with inorganic and organic properties.	26
Table 5.1:	Percentage of rutile phase, and tap densities of the $Ni_{0.1}W_{0.1}Ti_{0.8}O_2$ composition at different calcinations temperatures.	121
Table 5.2:	The colour parameters (CIE L*a*b*) for $Ni_{0.1}W_{0.1}Ti_{0.8}O_2$ and $BaNiTi_7O_{16}$ solid solution compositions at different temperatures.	127
Table 6.1:	Percentage of rutile Phase, relative XRD intensities of the anatase and rutile phases and tap densities of the various $Cr_{2x}W_xTi_{1-3x}O_2$ compositions at different calcination temperatures.	141
Table 6.2:	Variation in crystallite size, surface area and particle size for calcined (at 800ºC for 2h) $Cr_{2x}W_xTi_{1-3x}O_2$ solid solution with change in dopant concentration.	143
Table 6.3:	Variation in lattice parameters (a, c) and volume (at 800ºC for 2h) $Cr_{2x}W_xTi_{1-3x}O_2$ solid solution with change in dopant concentrations.	144

Annexure

List of Figures and Tables

Appendix A

The typical data collection parameters for $CuNb_2O_6$

Molecular formula	$CuNb_2O_6$
Goniometer	PW3050/60
Radiation	$K\alpha 1$= 1.54060 Å $K\alpha 2$ = 1.54443 Å
Formula mass	345.35525
Density (calculated) (g cm^{-3})	5.6334
Space group (No)	$P2_1/C$ (14)
Volume (Å) ^{3}	407.1416
Z	4

Appendix B

The typical data collection parameters for $FeNbO_4$

Molecular formula	$FeNbO_4$
Goniometer	PW3050/60
Radiation	*Kα1*= 1.54060 Å *Kα2* = 1.54443 Å
Formula mass	425.5020
Density (calculated) (g cm^{-3})	5.4290
Space group (No)	*Pbcn (60)*
Volume (Å) ^{3}	130.1271

Appendix C

The typical data collection parameters for $CuGa_2O_4$

Molecular formula	$CuGa_2O_4$
Goniometer	PW3050/60
Radiation	*Kα1*= 1.54060 Å *Kα2* = 1.54443 Å
Formula mass (g mol^{-1})	2135.918
Density (calculated) (g cm^{-3})	6.2202
Space group (No)	Fd-3m (227)
Volume (Å) ^{3}	570.1202

Chapter 7

Conclusions and Scope of Future Studies

The present research effort establishes a versatile and technically simple chemical synthesis methodology through successful preparation of nanocrystalline powders of a variety of mixed metal oxide compositions (as is summarized below). The synthesis method involves pyrolysis of aqueous-based precursor solutions that comprises of water-soluble, metal ion-ligand complexes of the desired metal ions and triethanolamine (TEA), in the requisite molar ratios. The chelating agents used for obtaining the water-soluble, metal ion-ligand complexes are: TEA, oxalic acid, EDTA and tartaric acid. The as-prepared powders as well as the powders calcined at their respective crystallization temperatures have been characterized with respect to their crystal structure and phase, particle morphology and composition along with investigation of their respective gas sensing and pigmentary properties. The work carried out in the present investigation can be summarized as follows:

Prepared Metal Oxide Compositions	**Properties Studied**
Nanocrystalline powders of: $CuNb_2O_6$; $CuGa_2O_4$; $FeNbO_4$ and Pt impregnated $FeNbO_4$	• Gas sensing property through Electrical conductivity measurements in dry air. • Gas sensing property towards 500 ppm of reducing gases such as, hydrogen, liquefied petroleum gas (LPG), and ammonia.
Nanocrystalline powders of $Ni_{0.1}W_{0.1}Ti_{0.8}O_2$; $NiBaTi_7O_{16}$; and $Cr_{2x}W_xTi_{1-3x}O_2$ (x = 0.05, 0.1, 0.15)	• UV-visible Absorption Spectroscopy • Color measurement

The major conclusion drawn from the present investigation can be summarized as follows:

❍ The synthesis method developed in this present study is versatile and can be extended to the preparation of nanocrystalline powders of a variety of metal oxide

compositions particularly, the niobium/ tantalum/ titanium based systems, which are difficult to process otherwise.

- The developed method result is polycrystalline and single phase final powders of the desired metal oxide compositions at processing temperatures (i.e., ≤ 850 ºC) that are comparatively lower than those reported in literature so far, with grain sizes in the nano-metric range (i.e., < 60 nm) and the specific surface from 40-120 m^2/g.

- The present investigation establishes the gas-sensing behavior of nanocrystalline $CuGa_2O_4$, $FeNbO_4$, and Pt-$FeNbO_4$ systems for the very first time in literature. The synthesized nanocrystalline powders of $CuNb_2O_6$, $CuGa_2O_4$, $FeNbO_4$, and Pt-$FeNbO_4$ exhibit *n*-type semiconducting behaviors and gas sensing characteristics towards H_2, LPG, and NH_3.

- The compressed pellets of the prepared nanocrystalline oxides in pellet show response towards H_2, LPG and NH_3 at operating temperatures ranging between 250 ºC and 400 ºC. Incorporation of platinum into $FeNbO_4$ (i.e., Pt-$FeNbO_4$ system) is found to improve the system's gas sensing properties through reduction in the sensor operating temperature, sensor response time and recovery time. The details of the oxide systems and their observed gas sensing behaviors towards reducing gases such as, hydrogen, LPG and ammonia are summarized as follows:

Nanocrystalline Mixed Metal Oxide Powders for Sensor Applications						
System	**Phase formation temperature**	**Structure**	**Particle size (TEM)**	**% of Response (working temperature)**		
				H_2 (500 ppm)	**NH_3 (500 ppm)**	**LPG (500 ppm)**
$FeNbO_4$	850 ºC	Orthorhombic	35-60 nm	93 (250 ºC)	52.0 (300 ºC)	92 (300 ºC)
Pt-$FeNbO_4$	850 ºC	Orthorhombic	35-60 nm	94 (175 ºC)	61.5 (250 ºC)	94 (200 ºC)
$CuNb_2O_6$	700 ºC	Monoclinic	20-38 nm	84 (300 ºC)	56 (400 ºC)	80 (300 ºC)
$CuGa_2O_4$	750 ºC	Spinel	30-60 nm	80 (350 ºC)	38 (350 ºC)	72 (350 ºC)

Non-toxic, chemically inert, thermally stable, nanocrystalline powders of titanates with compositions of $Ni_{0.1}W_{0.1}Ti_{0.8}O_2$, and $BaNiTi_7O_{16}$ along with and $Cr_{2x}W_xTi_{1-3x}O_2$ (x = 0.05, 0.1, 0.15) have been prepared, characterized and tested for their pigmentary properties. Ni^{2+}or Cr^{3+} doped nanocrystalline titanate powders show interesting color shades in different color range due to *d-d* transition of the *d*-electrons of Ni^{2+}or Cr^{3+} ions. The measurement of the color parameters (*CIE L* a* b**) reflect an intense yellow color with greenish shades for the $BaNiTi_7O_{16}$ composition, while the $Ni_{0.1}W_{0.1}Ti_{0.8}O_2$ solid solution exhibit yellow coloration with reddish shades. Doping of Cr^{3+} ion in the rutile lattice on the other hand, impart buff coloration to the $Cr_{2x}W_xTi_{1-3x}O_2$ (x = 0.05, 0.1, 0.15)] solid solution. The oxide systems and their structural, morphological and optical properties can be summarized as follows:

Nanocrystalline Mixed Metal Oxide Powders for Application in Pigments						
Pigment Compositions	**Phase formation temp.**	**Structure**	**Particle size (nm)**	**Absorption band for the d-d transitions (nm)**		
Yellow Color				**$^3A_{2g}(F)\rightarrow {}^3T_{1g}(P)$**	**$^3A_{2g}(F)\rightarrow {}^3T_{1g}(F)$**	**$^3A_{2g}(F)\rightarrow {}^3T_{2g}(F)$**
$Ni_{0.1}W_{0.1}Ti_{0.8}O_2$	800 ºC	Rutile	25-60	350–570	600–950	970-1100
$BaNiTi_7O_{16}$	850 ºC	Priderite	25-60	275–550	570–950	950-1100
Reddish Brown Color				**$^4A_{2g}(F)\rightarrow {}^4T_{1g}(P)$**	**$^4A_{2g}(F)\rightarrow {}^4T_{1g}(F)$**	**$^4A_{2g}(F)\rightarrow {}^4T_{2g}(F)$**
$Cr_{2x}W_xTi_{1-3x}O_2$ (x = 0.05, 0.10, 0.15)	800 ºC	Rutile	30-60	UV region	455	600

Scope of Future Work

- Further studies on the sensitivity of all the synthesized nanocrystalline mixed metal oxides can be carried out using their thick films.
- The effect of doping of the different noble metals and transition metals in the prepared oxides sensors can be studied for improving the sensitivity of these materials.
- The developed synthesis method can be applied for the preparation of different niobium and tantalum based nanocrystalline metal oxide sensor materials.
- The advantages of the prepared oxide pigments can be further investigated after paint formulations through dispersing the prepared nanopowders in suitable dispersing medium.

****

Chapter 7

Conclusions and Scope of Future Studies

Chapter 7

Conclusions and Scope of Future Studies

The present research effort establishes a versatile and technically simple chemical synthesis methodology through successful preparation of nanocrystalline powders of a variety of mixed metal oxide compositions (as is summarized below). The synthesis method involves pyrolysis of aqueous-based precursor solutions that comprises of water-soluble, metal ion-ligand complexes of the desired metal ions and triethanolamine (TEA), in the requisite molar ratios. The chelating agents used for obtaining the water-soluble, metal ion-ligand complexes are: TEA, oxalic acid, EDTA and tartaric acid. The as-prepared powders as well as the powders calcined at their respective crystallization temperatures have been characterized with respect to their crystal structure and phase, particle morphology and composition along with investigation of their respective gas sensing and pigmentary properties. The work carried out in the present investigation can be summarized as follows:

Prepared Metal Oxide Compositions	**Properties Studied**
Nanocrystalline powders of: $CuNb_2O_6$; $CuGa_2O_4$; $FeNbO_4$ and Pt impregnated $FeNbO_4$	• Gas sensing property through Electrical conductivity measurements in dry air. • Gas sensing property towards 500 ppm of reducing gases such as, hydrogen, liquefied petroleum gas (LPG), and ammonia.
Nanocrystalline powders of $Ni_{0.1}W_{0.1}Ti_{0.8}O_2$; $NiBaTi_7O_{16}$; and $Cr_{2x}W_xTi_{1-3x}O_2$ (x = 0.05, 0.1, 0.15)	• UV-visible Absorption Spectroscopy • Color measurement

The major conclusion drawn from the present investigation can be summarized as follows:

❍ The synthesis method developed in this present study is versatile and can be extended to the preparation of nanocrystalline powders of a variety of metal oxide

compositions particularly, the niobium/ tantalum/ titanium based systems, which are difficult to process otherwise.

- The developed method result is polycrystalline and single phase final powders of the desired metal oxide compositions at processing temperatures (i.e., ≤ 850 ºC) that are comparatively lower than those reported in literature so far, with grain sizes in the nano-metric range (i.e., < 60 nm) and the specific surface from 40-120 m^2/g.

- The present investigation establishes the gas-sensing behavior of nanocrystalline $CuGa_2O_4$, $FeNbO_4$, and Pt-$FeNbO_4$ systems for the very first time in literature. The synthesized nanocrystalline powders of $CuNb_2O_6$, $CuGa_2O_4$, $FeNbO_4$, and Pt-$FeNbO_4$ exhibit *n*-type semiconducting behaviors and gas sensing characteristics towards H_2, LPG, and NH_3.

- The compressed pellets of the prepared nanocrystalline oxides in pellet show response towards H_2, LPG and NH_3 at operating temperatures ranging between 250 ºC and 400 ºC. Incorporation of platinum into $FeNbO_4$ (i.e., Pt-$FeNbO_4$ system) is found to improve the system's gas sensing properties through reduction in the sensor operating temperature, sensor response time and recovery time. The details of the oxide systems and their observed gas sensing behaviors towards reducing gases such as, hydrogen, LPG and ammonia are summarized as follows:

Nanocrystalline Mixed Metal Oxide Powders for Sensor Applications						
System	**Phase formation temperature**	**Structure**	**Particle size (TEM)**	**% of Response (working temperature)**		
				H_2 (500 ppm)	**NH_3 (500 ppm)**	**LPG (500 ppm)**
$FeNbO_4$	850 ºC	Orthorhombic	35-60 nm	93 (250 ºC)	52.0 (300 ºC)	92 (300 ºC)
Pt-$FeNbO_4$	850 ºC	Orthorhombic	35-60 nm	94 (175 ºC)	61.5 (250 ºC)	94 (200 ºC)
$CuNb_2O_6$	700 ºC	Monoclinic	20-38 nm	84 (300 ºC)	56 (400 ºC)	80 (300 ºC)
$CuGa_2O_4$	750 ºC	Spinel	30-60 nm	80 (350 ºC)	38 (350 ºC)	72 (350 ºC)

Non-toxic, chemically inert, thermally stable, nanocrystalline powders of titanates with compositions of $Ni_{0.1}W_{0.1}Ti_{0.8}O_2$, and $BaNiTi_7O_{16}$ along with and $Cr_{2x}W_xTi_{1-3x}O_2$ (x = 0.05, 0.1, 0.15) have been prepared, characterized and tested for their pigmentary properties. Ni^{2+}or Cr^{3+} doped nanocrystalline titanate powders show interesting color shades in different color range due to *d-d* transition of the *d*-electrons of Ni^{2+}or Cr^{3+} ions. The measurement of the color parameters (*CIE L* a* b**) reflect an intense yellow color with greenish shades for the $BaNiTi_7O_{16}$ composition, while the $Ni_{0.1}W_{0.1}Ti_{0.8}O_2$ solid solution exhibit yellow coloration with reddish shades. Doping of Cr^{3+} ion in the rutile lattice on the other hand, impart buff coloration to the $Cr_{2x}W_xTi_{1-3x}O_2$ (x = 0.05, 0.1, 0.15)] solid solution. The oxide systems and their structural, morphological and optical properties can be summarized as follows:

Nanocrystalline Mixed Metal Oxide Powders for Application in Pigments						
Pigment Compositions	**Phase formation temp.**	**Structure**	**Particle size (nm)**	**Absorption band for the d-d transitions (nm)**		
Yellow Color				**$^3A_{2g}(F)\rightarrow {}^3T_{1g}(P)$**	**$^3A_{2g}(F)\rightarrow {}^3T_{1g}(F)$**	**$^3A_{2g}(F)\rightarrow {}^3T_{2g}(F)$**
$Ni_{0.1}W_{0.1}Ti_{0.8}O_2$	800 ºC	Rutile	25-60	350–570	600–950	970-1100
$BaNiTi_7O_{16}$	850 ºC	Priderite	25-60	275–550	570–950	950-1100
Reddish Brown Color				**$^4A_{2g}(F)\rightarrow {}^4T_{1g}(P)$**	**$^4A_{2g}(F)\rightarrow {}^4T_{1g}(F)$**	**$^4A_{2g}(F)\rightarrow {}^4T_{2g}(F)$**
$Cr_{2x}W_xTi_{1-3x}O_2$ (x = 0.05, 0.10, 0.15)	800 ºC	Rutile	30-60	UV region	455	600

Scope of Future Work

- Further studies on the sensitivity of all the synthesized nanocrystalline mixed metal oxides can be carried out using their thick films.
- The effect of doping of the different noble metals and transition metals in the prepared oxides sensors can be studied for improving the sensitivity of these materials.
- The developed synthesis method can be applied for the preparation of different niobium and tantalum based nanocrystalline metal oxide sensor materials.
- The advantages of the prepared oxide pigments can be further investigated after paint formulations through dispersing the prepared nanopowders in suitable dispersing medium.

****

Appendix A

The typical data collection parameters for $CuNb_2O_6$

Molecular formula	$CuNb_2O_6$
Goniometer	PW3050/60
Radiation	$K\alpha 1$= 1.54060 Å $K\alpha 2$ = 1.54443 Å
Formula mass	345.35525
Density (calculated) (g cm^{-3})	5.6334
Space group (No)	$P2_1/C$ (14)
Volume (Å) ^{3}	407.1416
Z	4

Appendix B

The typical data collection parameters for $FeNbO_4$

Molecular formula	$FeNbO_4$
Goniometer	PW3050/60
Radiation	*Kα1*= 1.54060 Å *Kα2* = 1.54443 Å
Formula mass	425.5020
Density (calculated) (g cm^{-3})	5.4290
Space group (No)	*Pbcn (60)*
Volume (Å) ^{3}	130.1271

Appendix C

The typical data collection parameters for $CuGa_2O_4$

Molecular formula	$CuGa_2O_4$
Goniometer	PW3050/60
Radiation	*Kα1*= 1.54060 Å *Kα2* = 1.54443 Å
Formula mass (g mol^{-1})	2135.918
Density (calculated) (g cm^{-3})	6.2202
Space group (No)	Fd-3m (227)
Volume (Å) ^{3}	570.1202

Annexure

List of Figures and Tables

List of Figures

		Page
Figure 1.1:	Schematic illustration for Bottom-up and Top-down approach.	6
Figure 1.2:	Schematic representation of metal ion-ligand complex based precursor solution method.	14
Figure 1.3:	A photograph of black carbonaceous fluffy mass.	14
Figure 1.4:	Probable metal-TEA complex.	15
Figure 2.1:	Schematic representation of the preparation of the aqueous solution of niobium tartrate.	45
Figure 2.2:	Schematic representation of the preparation of the nanocrystalline $CuNb_2O_6$.	47
Figure 2.3:	Simultaneously recorded TGA/DTA plots of the carbonaceous precursors of $CuNb_2O_6$.	49
Figure 2.4:	(a) X-Ray diffractogram (using CuK_α radiation) of the $CuNb_2O_6$ calcined at 700 ºC for 2 h. (b) Rietveld refinement of monoclinic $CuNb_2O_6$ calcined at 700 ºC for 2 h. Vertical bars show the positions of Bragg reflections.	50
Figure 2.5:	EDX analysis of the $CuNb_2O_6$ after calcination at 700 ºC for 2 h.	50
Figure 2.6:	(a) Bright field TEM micrograph of the calcined (at 700 ºC for 2h) $CuNb_2O_6$. (b) SAED pattern of the calcined (at 700ºC for 2h) $CuNb_2O_6$.	51
Figure 2.7:	FESEM image of nanocrystalline $CuNb_2O_6$ powders.	52
Figure 2.8:	FESEM image of pellet surface derived from nanosized $CuNb_2O_6$ powder.	52
Figure 2.9:	Schematic representation of (a) porous and (b) compact sensing layer with geometry and energy band. x_g grain size, L_D Debye length, eV_s band bending, z_o thickness of the depleted surface layer and z_g layer thickness.	53
Figure 2.10:	Photograph of setup equipment for resistance measurements and the cylindrical test-chamber with steel made sample holder (Inset).	54
Figure 2.11:	Setup equipment for in-situ resistance measurements	55

Figure 2.12:	Arrhenius plot for electrical conductivity of $CuNb_2O_6$ in air.	58
Figure 2.13:	Response characteristics of porous pellets of nanocrystalline $CuNb_2O_6$ towards 500 ppm each of H_2, LPG, and NH_3 in air as a function of temperature.	59
Figure 2.14:	Responses of porous pellets of nanocrystalline $CuNb_2O_6$ towards 500 ppm of H_2 in air at different temperatures.	59
Figure 2.15:	Responses of porous pellet of nanocrystalline $CuNb_2O_6$ towards 500 ppm of LPG in air at different temperatures.	59
Figure 2.16:	Responses of porous pellet of nanocrystalline $CuNb_2O_6$ towards 500 ppm of NH_3 in air at different temperatures.	59
Figure 2.17:	Electrical resistance of porous pellet of $CuNb_2O_6$ in alternating environments of air and (a) 500 ppm H_2 (b) 500 ppm LPG at 300 ºC and (c) 500 ppm NH_3 at 400 ºC.	60
Figure 2.18:	Variation of sensitivity of porous pellet of $CuNb_2O_6$ with concentration of H_2 and LPG at 300 ºC.	61
Figure 2.19:	Temperature variation of response time and recovery time for $CuNb_2O_6$ for 500 ppm H_2, LPG and NH_3.	61
Figure 3.1:	Schematic representation of the preparation of the nanocrystalline powders of $FeNbO_4$ composition.	73
Figure 3.2:	Simultaneously recorded TGA/DTA plots of the carbonaceous precursors of $FeNbO_4$.	74
Figure 3.3:	(a) X-ray diffractograms (using CuK_α radiation) of the $FeNbO_4$ precursor on calcination at various temperatures. (b) Rietveld refinement of orthorhombic $FeNbO_4$ calcined at 850 ºC for 3 h. Vertical bars show the positions of Bragg reflections.	75
Figure 3.4:	X-ray diffractogram (using CuK_α radiation) of the platinum incorporated $FeNbO_4$ after calcination at 850 ºC for 1 h.	77
Figure 3.5:	EDX pattern of (1 wt %) platinum impregnated $FeNbO_4$ after calcination at 850 ºC for1 h.	77
Figure 3.6:	Bright field TEM micrograph of the calcined (at 850 ºC for 3 h) $FeNbO_4$.	78
Figure 3.7:	Bright field TEM micrograph of Pt-$FeNbO_4$ after calcined (at 850 ºC for 1 h). (Inset) SAED pattern of Pt-$FeNbO_4$.	78

Figure 3.8:	FESEM micrograph of pellet derived from the calcined (at 850 ºC for 2 h) powders of the nanocrystalline $FeNbO_4$	79
Figure 3.9:	FESEM micrograph of pellet derived from the calcined (at 850 ºC for 1 h) powders of the nanocrystalline Pt-$FeNbO_4$.	79
Figure 3.10:	BET isotherms of nanocrystalline $FeNbO_4$ and platinum (1 wt %) incorporated $FeNbO_4$.	79
Figure 3.11:	Arrhenius plot for electrical conductivity of $FeNbO_4$ and platinum (1 wt %) incorporated $FeNbO_4$ in air.	81
Figure 3.12:	Response characteristics of nanocrystalline $FeNbO_4$ and Pt-$FeNbO_4$ in porous pellet forms towards 500 ppm each of H_2, LPG, and NH_3 in air as a function of temperature.	83
Figure 3.13:	Response characteristics of $FeNbO_4$ and platinum (1 wt %) incorporated $FeNbO_4$ for 500 ppm of LPG at 200 ºC.	83
Figure 3.14:	Electrical resistance of Pt-$FeNbO_4$ in alternating environments of air and LPG (500 ppm) at 200 ºC.	83
Figure 4.1:	Schematic representation of the preparation of the nanocrystalline $CuGa_2O_4$.	93
Figure 4.2:	(a) X-Ray diffractogram (using CoK_α radiation) of the $CuGa_2O_4$ calcined at 750 ºC for 2 h. (b) Rietveld refinement of monoclinic $CuGa_2O_4$ calcined at 750 ºC for 2 h. Vertical bars show the positions of Bragg reflections.	94
Figure 4.3:	EDX analysis of the $CuGa_2O_4$ after calcination at 750 ºC for 2 h.	95
Figure 4.4:	Bright field TEM micrograph of the calcined (at 750 ºC for 2 h) $CuGa_2O_4$.	96
Figure 4.5:	FESEM image of nanocrystalline $CuGa_2O_4$ powders.	97
Figure 4.6:	FESEM image of pellet surface derived from nanocrystalline $CuGa_2O_4$ powder.	98
Figure 4.7:	Arrhenius plot for electrical conductivity of $CuGa_2O_4$ in air and argon.	99
Figure 4.8:	Sensing characteristics of nanocrystalline $CuGa_2O_4$ in the form of porous pellet towards 500 ppm each of H_2, LPG, and NH_3 in air as a function of temperature.	100

Figure 4.9:	Responses of porous pellet of nanocrystalline $CuGa_2O_4$ towards 500 ppm of H_2 in air at different temperatures.	100
Figure 4.10:	Responses of porous pellet of nanocrystalline $CuGa_2O_4$ towards 500 ppm of LPG in air at different temperatures.	101
Figure 4.11:	Responses of porous pellet of nanocrystalline $CuGa_2O_4$ towards 500 ppm of NH_3 in air at different temperatures.	101
Figure 4.12:	Electrical resistance of porous pellet of $CuGa_2O_4$ in alternating environments of air and 500 ppm LPG at 350 ºC.	101
Figure 4.13:	Variation of response of porous pellet of nanocrystalline $CuNb_2O_6$ with concentration of H_2 and LPG at 350 ºC.	102
Figure 4.14:	Temperature variation of response time and recovery time for $CuGa_2O_4$ for 500 ppm H_2, LPG and NH_3.	102
Figure 5.1:	Schematic representation of the preparation of the aqueous solution of dimethylammonium tungstate.	112
Figure 5.2:	Schematic representation of the preparation of the aqueous solution of titanium oxalate.	113
Figure 5.3:	Schematic representation of the preparation of the nanocrystalline powders of $Ni_{0.1}W_{0.1}Ti_{0.8}O_2$	114
Figure 5.4:	Schematic representation of the synthesis of the nanocrystalline powders of $BaNiTi_7O_{16}$.	115
Figure 5.5:	Simultaneously recorded TGA and DTA plots of the carbonaceous precursors of solid solution composition: (a) $Ni_{0.1}W_{0.1}Ti_{0.8}O_2$, (b) $BaNiTi_7O_{16}$.	118
Figure 5.6:	X-ray diffractograms (using CuK_α radiation) of $Ni_{0.1}W_{0.1}Ti_{0.8}O_2$ precursor on calcination at various temperatures.	119
Figure 5.7:	X-ray diffractograms (using CuK_α radiation) of $BaNiTi_7O_{16}$ precursor on calcination at various temperatures.	122
Figure 5.8:	(a), (b), and (3): Bright field TEM micrograph of the calcined (800 ºC for 2 h) $Ni_{0.1}W_{0.1}Ti_{0.8}O_2$ solid solution. Figure-5.8(d): HRTEM image of the calcined (800 ºC for 2 h) $Ni_{0.1}W_{0.1}Ti_{0.8}O_2$ solid solution.	123
Figure 5.9:	SAED pattern of the calcined (800 ºC for 2 h) $Ni_{0.1}W_{0.1}Ti_{0.8}O_2$ showing distinct rings corresponding to the (1 0 1), (2 0 0), (2 2 0) planes in a rutile lattice.	124

Figure 5.10:	Bright field TEM micrograph of the calcined (850 ºC for 2 h) $BaNiTi_7O_{16}$ composition.	125
Figure 5.11:	SAED pattern of the calcined (850 ºC for 2 h) $BaNiTi_7O_{16}$ with a priderite structure.	125
Figure 5.12:	UV-visible-NIR absorption spectra for calcined (at 800 ºC for 2h) powder of the $Ni_{0.1}W_{0.1}Ti_{0.8}O_2$ solid solution.	126
Figure 5.13:	UV-visible-NIR absorption spectra for calcined (at 850 ºC for 2h) powder of the $BaNiTi_7O_{16}$ solid solution.	126
Figure 6.1:	Process for the preparation of the nanocrystalline solid solution compositions of $Cr_{2x}W_xTi_{1-3x}O_2$.	137
Figure 6.2:	Simultaneously recorded TGA/ DTG/ DTA plots of the carbonaceous precursors of $Cr_{2x}W_xTi_{1-3x}O_2$ (x = 0.05) solid solution composition.	139
Figure 6.3:	X-ray diffractograms (using CuK_α radiation) of the $Cr_{2x}W_xTi_{1-3x}O_2$ (x = 0.05) precursors on calcination at various temperatures.	140
Figure 6.4:	X-ray diffractograms (using CuK_α radiation) of the various $Cr_{2x}W_xTi_{1-3x}O_2$ solid solution compositions after calcination at 800 ºC for 2 h.	142
Figure 6.5:	Plot of ($\beta^o\cos\theta/\lambda$) versus ($\sin\theta/\lambda$) for $Cr_{2x}W_xTi_{1-3x}O_2$ (with x = 0.05) solid solution composition.	142
Figure 6.6:	Bright field TEM micrograph of the calcined (800 ºC for 2 h) $Cr_{2x}W_xTi_{1-3x}O_2$ (x = 0. 05) solid solution composition.	145
Figure 6.7:	Distribution of particle sizes, evaluated from TEM studies, for the calcined (800 ºC for 2 h) $Cr_{2x}W_xTi_{1-3x}O_2$ (x = 0. 05) solid solution composition.	145
Figure 6.8:	Bright field TEM micrograph of the calcined (800 ºC for 2 h) $Cr_{2x}W_xTi_{1-3x}O_2$ (x = 0.10) solid solution composition.	145
Figure 6.9:	Distribution of particle sizes, evaluated from TEM studies, for the calcined (800 ºC for 2 h) $Cr_{2x}W_xTi_{1-3x}O_2$ (x = 0. 10) solid solution composition.	146
Figure 6.10:	Selected-area Electron Diffraction (SAED) pattern of the calcined (800 ºC for 2h) $Cr_{2x}W_xTi_{1-3x}O_2$ (x = 0.05) composition showing distinct rings corresponding to the (110), (101), (111), (211) planes in a rutile lattice.	146

Figure 6.11: HRTEM image of the calcined (800 ºC for 2 h) $Cr_{2x}W_xTi_{1-3x}O_2$ (x = 0.05) composition. 146

Figure 6.12: FESEM micrograph of the calcined (800 ºC for 2 h) $Cr_{2x}W_xTi_{1-3x}O_2$ (x = 0.05) solid solution composition. 147

Figure 6.13: UV-visible absorption spectra for calcined (at 800 ºC for 2 h) powders of the $Cr_{2x}W_xTi_{1\ 3x}O_2$ solid solution compositions. 148

Figure 6.14: Plot of K/S versus dopant amount (x) for the various $Cr_{2x}W_xTi_{1-3x}O_2$ solid solution compositions. 149

Figure 6.15: Figure 6.15: XRD phase analysis of $Cr_{2x}W_xTi_{1-3x}O_2$ (x = 0.05) solid solution composition after annealing at 1200 ºC for 3 h. 150

List of Tables

		Page
Table 1.1:	Summary of changes observed in some of the physical properties for nanocrystalline materials.	2
Table 1.2:	Traditional properties associated with inorganic and organic properties.	26
Table 5.1:	Percentage of rutile phase, and tap densities of the $Ni_{0.1}W_{0.1}Ti_{0.8}O_2$ composition at different calcinations temperatures.	121
Table 5.2:	The colour parameters (CIE L*a*b*) for $Ni_{0.1}W_{0.1}Ti_{0.8}O_2$ and $BaNiTi_7O_{16}$ solid solution compositions at different temperatures.	127
Table 6.1:	Percentage of rutile Phase, relative XRD intensities of the anatase and rutile phases and tap densities of the various $Cr_{2x}W_xTi_{1-3x}O_2$ compositions at different calcination temperatures.	141
Table 6.2:	Variation in crystallite size, surface area and particle size for calcined (at 800ºC for 2h) $Cr_{2x}W_xTi_{1-3x}O_2$ solid solution with change in dopant concentration.	143
Table 6.3:	Variation in lattice parameters (a, c) and volume (at 800ºC for 2h) $Cr_{2x}W_xTi_{1-3x}O_2$ solid solution with change in dopant concentrations.	144

Curriculum Vita

Mr. Soumya Kanti Biswas studied undergraduate in Berhampore K. N. College and received his B.Sc. Degree with Honours in Chemistry in 2000 from the Calcutta University, West Bengal, India. After being awarded M. Sc. Degree in Chemistry in 2002 from the Banaras Hindu University, Varanasi, India, he joined to the Department of Chemistry, Indian Institute of Technology Kharagpur in the same year for his doctoral program and enrolled as a research scholar in February 2003. During his doctoral studies he has published several scientific papers in many international journals, which include Material Research Bulletin, Journal of the American Ceramic Society, Ceramics International, Journal of the European Ceramic Society, Sensors and Actuators B, Journal of Electrochemical Society etc. His research work has been presented in many national and international conferences. His current research interest includes studies on gas sensing behaviour of different nanosized inorganic oxides and development of high performance nanosized inorganic pigments.

List of publication

Thesis related

- "Studies on the gas sensing behaviour of nanosized $CuNb_2O_6$ towards ammonia, hydrogen and liquefied petroleum gas", S. K. Biswas, P. Pramanik, Sensors and Actuators B (In press, 2008).
- "Sensing Properties of Chemically Synthesized Pristine and Pt Impregnated Nanosized $FeNbO_4$ in Hydrogen, Ammonia, and LPG" S. K. Biswas, T. Gnanasekaran, T. K. Ghorai, P. Pramanik. Journal of The Electrochemical Society, (2008), 155(1) J26-J31.
- "Chemical synthesis of environment-friendly nanosized yellow titanate pigments" S. K. Biswas, D. Dhak, A. Pathak, P. Pramanik. Material Research Bulletin (2008), 43, 665–675
- "Codoped Cr and W rutile nanosized powders obtained by pyrolysis of triethanolamine complexes" S. K. Biswas, A. Pathak, N. K. Pramanik, D. Dhak, P. Pramanik. Ceramic International (in press, 2007).
- "Studies on the gas sensing behaviour of nanosized $CuGaO_4$ towards ammonia, hydrogen and liquefied petroleum gas", S. K. Biswas, A. Pathak, P. Pramanik, (Communicated).

Other publication

- "Synthesis of Nanocrystalline $KTiOPO_4$ Powder by Chemical Method" S. K. Biswas, A. Pathak, P. Pramanik The Journal of the American Ceramic Society (2007), 90(4) 1071-1076.
- "A process for the preparation of nanosized $MTiO_3$" S. K. Biswas, P. Pramanik Patent Application 824/KOL/2005 published 2007-05-25, filed 2005-09-08. (PATENT)
- "Photocatalytic oxidation of organic dyes by nano-sized metal molybdate incorporated titanium dioxide ($M_xMo_xTi_{1-x}O_6$) (M = Ni, Cu, Zn) photocatalysts" T.K. Ghorai, D. Dhak, S. K. Biswas, S. Dalai, P. Pramanik. Journal of Molecular Catalysis A: Chemical (2007), 273, 224-229.
- "Synthesis and characterization of nanocrystalline $SrBi_2Nb_2O_9$ ferroelectric ceramics using TEA as the polymeric matrix" D. Dhak, S. K. Biswas, P. Pramanik Journal of the European Ceramic Society (2006), 26, 3717-3723.

- "Preparation of nanosized mixed-oxide powders" Pathak, A., Mohapatra, Sunita, Mohapatra Sasmita, Biswas, S. K., Dhak, D., Pramanik, N.K., Tarafdar, A., Pramanik. P. American Ceramic Society Bulletin. (2004), 83(8), 9301-9306.
- "Synthesis and characterization of hydroxyapatite/poly(vinyl alcohol phosphate) nanocomposite biomaterials", N. K. Pramanik, S. K. Biswas, P. Pramanik, International Journal of Applied Ceramic Technology (2008), 5(1), 20-28.
- "Preparation of nano-sized $ABi_2Nb_2O_9$ (A = Ca^{2+}, Sr^{2+}, Ba^{2+}) ferroelectric ceramics by soluble Nb(V) tartarate precursor and their dielectric characteristics after sintering", D. Dhak, P. Dhak,T. K. Ghorai, S. K. Biswas, P. Pramanik, Journal of Materials Science: Materials in Electronics (2008), 19(5), 448-456.
- Photooxidation of different organic dyes (RB, MO, TB, BG) using Fe(III)-doped TiO_2 nano-photocatalyst prepared by novel chemical method, T. K. Ghorai, S. K. Biswas, P. Pramanik Applied Surface Science, In Press, 2008.
- "Preparation of white pigments from nanosized alkaline earth metal titanates and potassium titanium oxophosphate", S. K. Biswas, P. Pramanik (communicated).